Technical Letter Report
[TLR-RES/DE/REB-2026-01]

Properties of Molten Chloride Salts and Modeling/Simulation Methods for Corrosion

Date:
January 2026

Prepared in response to Task 5 of User Need Request NRR-2022-002 by:

Laurent Capolungo
Xueyang Wu
Hannah K. Patenaude
Tanguy de Miscault
Marisa J. Monreal

Los Alamos National Laboratory

NRC Project Manager:

Wendy A. Reed
Reactor Engineering Branch

Division of Engineering
Office of Nuclear Regulatory Research
U.S. Nuclear Regulatory Commission
Washington, DC 20555–0001

Properties of Molten Chloride Salts and Modeling/Simulation Methods for Corrosion

Report submitted to **Nuclear Regulatory Commission (NRC)**

Date: September 29, 2025

Authors:

Laurent Capolungo, Xueyang Wu, Hannah K Patenaude, Tanguy de Miscault, Marisa J Monreal

Los Alamos National Laboratory (LANL)

Los Alamos National Laboratory Los Alamos, New Mexico, USA

Executive Summary

To meet the rapidly rising energy demand at the national scale, the nuclear energy industry is devoting significant resources to the development of Molten Salt Reactors (MSRs). The nuclear industry is developing these technologies due to factors of cost, thermal efficiency and safety. As such, several U.S. companies have engaged with the Nuclear Regulatory Commission (NRC) to seek approval for the construction of demonstration and commercial reactors. Both the efficiency and lifetime of the reactor depend on key properties of the salt and on their compatibility with the structural metal composing the vessel as well as on the operating conditions (e.g., temperature). Indeed, depending on their composition, molten salts can be particularly corrosive to structural metals, and potentially lead to a rapid propagation of the corrosion front, change in the chemical composition of the metal, formation of bicontinuous structures, and formation of cracks. The nuclear industry salt choice is anticipated to be guided by performance and cost considerations. As such, both fluoride and chloride-based salts are being proposed, along with various structural metals. While the knowledge base is quite extensive for the use of fluoride salts because of the U.S. Molten Salt Reactor Experiment (MSRE), significantly less work has been conducted on chloride salt behavior in the context of MSRs.

Modeling of material interactions in an MSR is particularly complex as key intrinsic properties of the salts will dynamically evolve during service due to the generation of fission products (e.g. noble gases, lanthanides). Further, impurities in the salt (e.g., water, oxygen, metallic impurities, oxides, etc.) can also considerably impact the salt properties. The salt state will also impact the neutron economy, reproduction factors, heat capacity, and viscosity, as well as its compatibility with the structural metal.

Motivated by the above, there is a need to (i) assess the state-of-knowledge of chloride salt properties, (ii) perform a state-of-the-art review dedicated to modeling techniques used to study molten salt properties, (iii) investigate the state of maturity of modeling techniques to predict corrosion of metals exposed to salts as a function of the salt state. These three objectives define the three focal aspects of this technical letter report.

The portion of the report on chloride salt properties presents the state-of-knowledge on the linkages between the salt composition and ionic radii effects, short and long-range correlations, thermochemical and thermophysical properties, homogeneous redox reactions, and a range of metal/salt interfacial properties such as heterogeneous redox reactions at the metal/salt interface, morphology, specific adsorption, composition, and electrostatic potential profiles. A focus is placed on actinide-bearing fuel salts. The report underscores how modern experimental efforts, such as thermal property measurements and electrochemical studies, are beginning to expand the knowledge gained from older fluoride-focused research, such as from MSRE. There is a particular value in the effort to combine experimental results with computational tools (such as thermodynamic calculations and databases) to inform predictions about corrosion and thermodynamic stability across various alloy and salt compositions. This report further highlights areas where knowledge may be expanded. Despite increased interest in chloride-based MSRs, there is not a large quantity of high-quality, *in situ* experimental data—especially for salts containing uranium and plutonium chlorides which are central to realistic reactor conditions. Further, the effects of impurities and fission products have not been thoroughly investigated. The impact of fission products on viscosity and heat capacity in chloride salts is largely unexplored. Only limited studies have examined this for simple $LnCl_3$ additions. Current models (molecular dynamics (MD), CALPHAD) often exclude fission products (FPs) contributions due to lack of data. Further, we note that there is little experimental data on how irradiation influences FP solubility, speciation, or volatility in molten chloride systems. Many corrosion studies rely on static exposure tests and lack real-time electroanalytical measurements that could provide kinetic insights into redox behavior and species transport. This limited understanding prevents having accurate predictive models and hinders the development of effective corrosion mitigation strategies. The report notes that standardized methodologies, broader compositional studies, and closer integration of modeling and experiments may play a role in the deployment readiness of chloride-based MSRs.

The presentation of modeling and simulation methods to predict properties of molten salts, which largely focus on the assessment of today's Molten Salt Thermal Properties Database–thermochemical and thermophysical (MSTDB-TC/TP) databases, reveals several important points. Overall, it is found that Gibbs free energy minimizers leveraging thermochemical databases are sufficiently mature to accurately quantify the driving forces for corrosion. In parallel, the quantitative effects of the electric double layer (EDL), a key factor in governing corrosion kinetics at the salt/metal interface, remains poorly understood in molten salts. Molecular dynamics and density functional theory simulations have revealed insights and data about ion crowding and overscreening phenomena, yet current models are limited by simplified system assumptions and a lack of data on impurities and radiation effects. More realistic and complex EDL modeling, using machine learning and REAXFF potentials, is a promising direction of modeling advances. Thermophysical properties such as viscosity, density, diffusion coefficients, and heat capacity have been extensively modeled using ab initio and molecular dynamics simulations. These models, though computationally intensive, often agree well with experimental data and have a crucial role in populating property databases. Increasing the use of interatomic potentials derived from machine learning is enabling exploration of multi-component salts and the effects of fission products and impurities. Nonetheless, the existing literature is sparse, and more coordinated studies are needed to ensure comprehensive coverage. In summary, while the current modeling framework provides robust tools for evaluating molten salt behavior, significant challenges remain—particularly in incorporating impurities, fission products, and interfacial reaction rates. Ongoing developments in databases, atomic scale simulations, and machine learning are expected to bridge these gaps, enabling more predictive and transferable corrosion models for use in advanced reactor designs.

Finally, this technical letter report also describes state-of-the-art modeling approaches for molten salt corrosion. Ideally such models should be able to capture the salt compositions which could arise during service, accounting for the evolution of the salt composition during service. Over the past decade, significant progress has been made in developing computational models to predict aspects of molten salt corrosion, such as mass loss, salt penetration depth, and corrosion front morphology. However, no universal model currently exists that can predict all features, and research needs remain; particularly in modeling Kirkendall void formation, reaction rates at salt-metal interfaces, and the effects of salt impurities and fission products. Models currently require calibration due to limited understanding of how metal and salt compositions affect the EDL and reaction kinetics. Though electrochemical tests, such as voltammetry, can help estimate rates, comprehensive thermodynamic databases, especially those accounting for impurities, are needed. Current modeling approaches include empirical and one-dimensional (1D) sharp-interface models, which assume an immediate phase boundary between the solid and the fluid. The sharp-interface models are computationally efficient and effective in simple scenarios such as planar fronts and diffusion-limited cases. However, the currently published sharp-interface models are limited in their ability to capture the morphology of the corrosion front and the competition between all diffusive processes. With greater but still accessible computational expense through high performance computing resources, diffusive interface models, particularly phase-field models (PFM), can handle complex morphologies, grain boundary effects, and thermodynamic coupling. One of the key challenges is that existing models cannot generalize across different metal-salt systems without recalibration. The roles of effective diffusivity and grain boundary contributions also are not fully accounted for in models today. While high-resolution simulations are necessary for accurately predicting corrosion front evolution, their computational demands restrict their applicability. Future directions could include the development of hybrid models that combine 1D sharp-interface approaches with corrections informed by PFM and surrogate models. In conclusion, efforts that integrate thermodynamic data, experimental validation, and computationally efficient surrogate models may enable constructing predictive models of molten salt corrosion over extended periods of time.

Table of Contents

Abbreviations

AMR	Adaptive Mesh Refinement
AIMD	Ab Initio Molecular Dynamics
ANLWR	Advanced Non-Light Water Reactor
ARE	Aircraft Reactor Experiment
BCC	Body-Centered Cubic
BV	Butler-Volmer
CALPHAD	CALculation of PHAse Diagrams
CCC	Conserved current condition
CE	Counter electrode
CSP	Concentrated solar power
CV	Cyclic voltammetry
DFT	Density functional theory
DOE	Department of Energy
DSC	Differential scanning calorimetry
EDL	Electric double layer
EDS	Energy dispersive X-ray spectroscopy
EKM	electrochemical kinetic models
EXAFS	Extended X-ray Absorption Fine Structure
FNN	First Nearest Neighbors
FP	Fission products
GCS	Gouy-Chapman-Stern
GP	Grand potential
GPR	Gibbs Phase Rule
IHP	Inner Helmholtz plane
INL	Idaho National Laboratory
KKS	Kim-Kim-Suzuki
KMC	Kinetic Monte Carlo
KP-FHR	fluoride salt-cooled high-temperature reactor
LANL	Los Alamos National Laboratory
LFA	Laser flash analysis
MC	Monte Carlo
MCFR	Molten Chloride Fast Reactor
MD	Molecular dynamics
MHC	Marcus-Hush-Chidsey
MMC	Metropolis Monte Carlo
MQM	Modified Quasichemical Model
MQMQA	Modified Quasichemical Model in the Quadruplet Approximation

MSR	Molten salt reactor
MSRE	Molten Salt Reactor Experiment
MSTDB	Molten Salt Thermal Properties Database
OHP	Outer Helmholtz plane
ORNL	Oak Ridge National Laboratory
PB	Poisson-Boltzmann
PFM	Phase-field models
PZC	Potential of zero charge
RE	Reference electrode
REAXFF	Reactive force-field
RMSE	Root Mean Square Error
SBM	Smoothed Boundary Method
SEM	Scanning electron microscopy
SER	Standard Element Reference
SNN	Second Nearest Neighbor
SRO	Short-Range Order
STM	Scanning tunneling electron microscopy
TES	Thermal energy storage
WBM	Wheeler-Boettinger-McFadden
WE	Working electrode
XRF	X-ray Fluorescence

1. Introduction

Over the past decade, Advanced Non-Light Water Reactor (ANLWR) designs have been proposed for safe and efficient nuclear reactors [1]. Within the large spectrum of reactors concepts being proposed, Molten Salt Reactors (MSRs) are one class of industrially considered technologies.

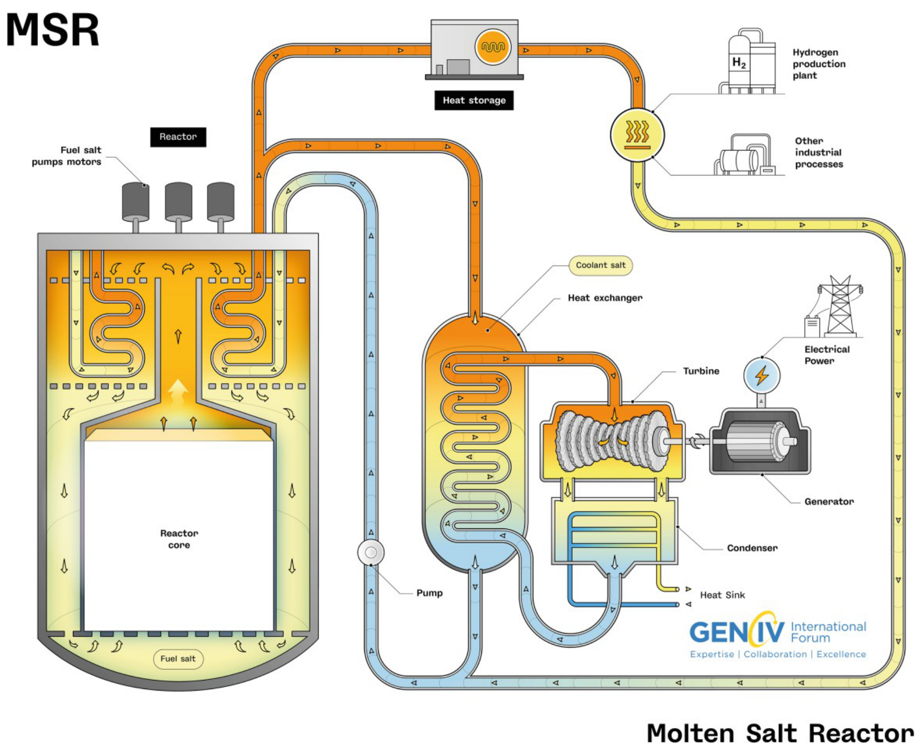

Figure 1: Schematic of a generic Molten Salt Reactor concept with fuel and coolant salts, power production, hydrogen production, and other industrial processes integrated into the plant. Figure adapted from source. [2]

The variety of designs that fall under the category of MSRs includes reactors that will use either chloride or fluoride liquid salt for fuels, coolants, or both. In the cases of salt fuels, the reactors proposed for near and mid-term technologies are thermal neutron or fast neutron reactors, will have fuels composed of fissile or fertile material, and may or may not incorporate online reprocessing of the fuel salt. A generic schematic of an MSR is shown in Figure 1 [2]. Currently, some of the most prominent designs nearing deployment include the Molten Chloride Fast Reactor (MCFR) from TerraPower, [3] the Kairos Power fluoride salt-cooled high-temperature reactor (KP-FHR) [4], and the Abilene Christian University salt-fueled and salt-cooled Molten Salt Research Reactor (Natura MSR-1, planned to be constructed in association with Natura Resources) [5]. The efforts led by the private sector are accompanied by several publicly sponsored initiatives which, for the most part, aim at understanding the fundamental properties of salts and the mechanisms by which the properties of metals degrade over time due to exposure to molten salts.

Molten salt reactors, particularly the fluid-fueled types, have unique considerations with regards to materials compatibility, fuel performance, and radionuclide management. Compatibility of materials with molten salts is one of the more unique aspects of MSR design. Chloride salts are being proposed for use in fast spectrum MSRs [6], and deployment of these reactors will involve addressing any safety considerations, including any that may arise from the complex chemistry and behavior of molten chloride salts. While the knowledge base is quite extensive for the use of fluoride salts because of the U.S. Molten Salt Reactor Experiment (MSRE) [7], significantly less work has been conducted on chloride salt behavior in the context of MSRs, although research activity in this area is increasing. The NRC has issued reports on material compatibility in molten salts [8]. Information referring to interactions between structural alloys and static, isothermal molten salts, specifically, can be found in [9], followed by reports summarizing models considered for the prediction of long-term corrosion in molten salts [10]. Further, an overview of what was known about the impact of fission products on the degradation of structural materials in MSRs was presented in [10] and [11]. Most recently, the NRC has supported assessment of electrochemical monitoring for MSRs [12].

Given the above, this report first focuses on the current status of experimental and computational efforts to understand chloride salt materials compatibility and properties for MSRs. The aim here is to complement and extend previous reports by highlighting key developments in molten salt chemistry, particularly chloride salt chemistry, to provide experimental and computational information for NRC's technical basis.

Second, focus is placed on assessing the state of modeling efforts to predict critically important properties of molten salts as a function of their composition (including lanthanides, alkali metals and other fission products). Focus is placed on (i) the predictions of redox potentials, (ii) our ability to understand the complex salt composition and charge distribution near the salt-metal interface (i.e., the so-called double layer), and on (iii) modeling approaches and applications to predict other important salt properties as a function of compositions. These properties included the salts' viscosity and heat capacity. Importantly, in this report we further perform an independent assessment of the accuracy of thermodynamics databases in predicting redox potentials associated with the Cr/Cr^{2+} couple in FLiNaK. In its simplest form, the redox potential is a measure of how easily a substance gains or loses electrons in a chemical reaction: a high redox potential means the substance easily gains electrons (acts as an oxidizing agent); a low redox potential means the substance easily loses electrons (acts as a reducing agent). The predictions are found to be in excellent agreement with experimental data; thereby demonstrating the prospects of augmenting the data from thermodynamic databases to predict salt properties for outside-the-database compositions, such as when impurities and fission products are present. Focus is placed on presenting the different modeling techniques available to predict molten salt properties (e.g. redox potential) as a function of salt composition and fission products.

The report details the strengths, weaknesses, and potential paths for improvements in empirical models, one-dimensional diffusion/reaction-based models, and phase-field modeling. These tools may be used for predicting macroscale corrosion (e.g., mass loss, penetration depth) and evolution of the morphology of the metal (e.g., planar corrosion front, bicontinuous structure, Kirkendall voids, cracks). Finally, this report concludes with a discussion of the different potential avenues enabling the development of practical models for molten salt corrosion over extended periods of time as the function of salt chemistry/composition.

2. Experimental Assessments of Molten Chloride Salt Properties

Many proposed ANLWRs designs are fundamentally different from the uranium oxide-fueled light-water reactors currently commercially deployed in the U.S. A prominent set of advanced reactor concepts are molten salt reactors, which comprise reactors that are designed to be fueled and/or cooled with liquid molten salts, typically chloride or fluoride salts. The molten salts of relevance to these reactor designs are corrosive, high-temperature, complex chemical systems—especially for fuel salts. In fuel salts, fission will occur during reactor operation and will be accompanied by changing concentrations of actinides (An), lanthanides (Ln), fission products (FPs), and corrosion products. Experimental data is being collected on these systems, and the experimental data is also being used to inform contemporary development of improved modeling and simulation capabilities.

MSRs are not an entirely novel concept: in the 1950s ORNL built a salt-fueled MSR to explore the possibility of a nuclear-powered airplane during the Aircraft Reactor Experiment (ARE). The ARE was the first example of an MSR and used a circulating molten salt fuel composed of $NaF{-}ZrF_4{-}UF_4$ (53.09-40.73-6.18 mol%) [17]. The ARE was succeeded by the MSRE which was a $LiF{-}BeF_2{-}ZrF_4{-}UF_4$ (65-29.1-5-0.9 mol%) fueled and $LiF{-}BeF_2$ cooled (46.9-53.1 mol%), reactor that operated at ORNL in the late 1960s. The design, construction, operation, experimentation, and decommissioning of the MSRE was well-documented and provided a wealth of knowledge that is still used today. These experiments provided the only available data from operating MSRs and the data from MSRE contributes to the knowledge used by those modern designs that plan to incorporate $LiF{-}BeF_2$ salts (commonly referred to as '*FLiBe*' salts). The other MSR designs that use molten salts, particularly chloride salts, do not benefit significantly from the MSRE accumulated knowledge, and the molten salt community rapidly works to produce reliable data to support chloride salt systems.

Multiple thorough reviews of material corrosion in molten salts exist and were used as the foundation for the present work [18–23]. Many reviews have focused on salt compositions that are primarily relevant to concentrated solar power (CSP) plants like alkali and/or alkaline earth chloride and fluoride salt compositions (e.g., $NaCl{-}MgCl_2$) [19, 20]. The primary salt in a molten salt is also termed the 'solvent salt', and that terminology is used in this report. Alkali and alkaline earth halides are generally the solvent salts in liquid-fueled MSR and pyroprocessing applications, and serve as carrier salts in which other species, like nuclear fuels (e.g., UCl_3 or UO_2), are dissolved [18, 22, 23]. Fewer reviews include information about corrosion measurements performed in complex, actinide-bearing molten chloride systems indicative of a modern MSR fuel system, given the difficulty of such measurements and the previous focus on fluorides within the legacy of the MSRE. The primary goal of this section is to provide a current repository of available data and results that can be used to inform licensing and regulation of MSRs, with a focus on material compatibility. The salts within the scope of this report include those applicable to MSRs: alkali and alkaline earth halide salts with and without additional components of reactor fuels (e.g., An, Ln, FP, and corrosion products). Table 1 summarizes the salts and common corrosion products that will be discussed in what follows.

Table 1: Chloride salts of interest for material compatibility in MSRs.

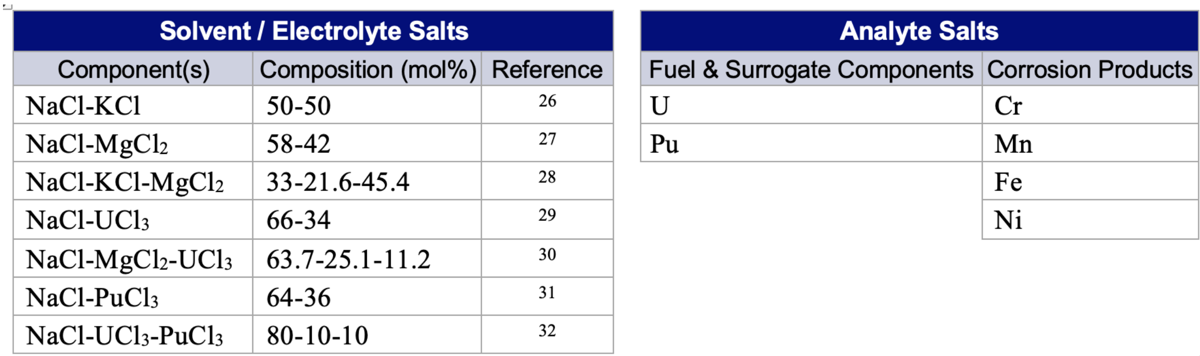

Solvent / Electrolyte Salts		
Component(s)	Composition (mol%)	Reference
$NaCl\text{-}KCl$	50-50	26
$NaCl\text{-}MgCl_2$	58-42	27
$NaCl\text{-}KCl\text{-}MgCl_2$	33-21.6-45.4	28
$NaCl\text{-}UCl_3$	66-34	29
$NaCl\text{-}MgCl_2\text{-}UCl_3$	63.7-25.1-11.2	30
$NaCl\text{-}PuCl_3$	64-36	31
$NaCl\text{-}UCl_3\text{-}PuCl_3$	80-10-10	32

Analyte Salts	
Fuel & Surrogate Components	Corrosion Products
U	Cr
Pu	Mn
	Fe
	Ni

Additionally, while many materials are included in the design and operation of any given MSR (see Figure 2), this work, like prior literature reviews [22–31], is concerned with those related to the physical infrastructure and containment that is in direct contact with molten salts. This report encompasses the interactions of molten salts with alloys, including but not limited to Hastelloy N, stainless steel, and Inconel. This report does not cover interactions of molten salts with carbon, ceramic, or vitreous materials. This work also covers fundamental salt properties, thermodynamic considerations, contemporary hypotheses about salt behavior at material interfaces, and commentary on the benefits of the experimental-computational cycle for modeling to support the licensing, regulation, and deployment of MSRs. An indepth investigation of updates to material compatibility following the previous reviews [8–12] is provided in this report, including an examination of the experimental approaches to molten salt corrosion measurements and an analysis of chloride versus fluoride salt corrosion intensity and mechanisms.

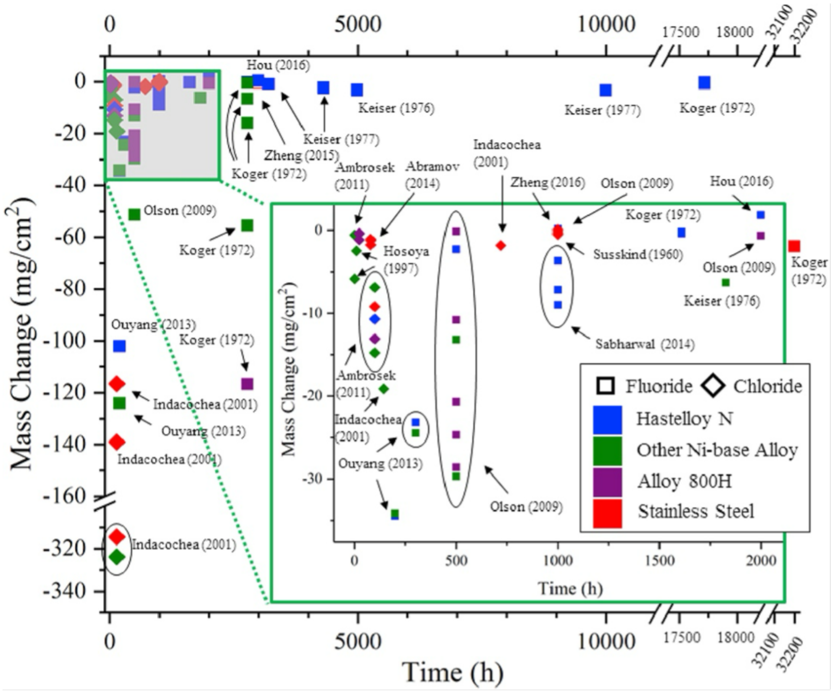

Figure 2: Mass change data as a function of time for corrosion experiments conducted in fluoride and chloride salts. Colors indicate sample materials. Figure adapted from source.[22]

2.1. Salt Properties

There are many intrinsic factors that contribute to or influence the interactions between ions in a molten salt and the surrounding materials, including but not limited to: atomic and microstructure; complexation, coordination, and bonding; and thermodynamic properties. These characteristics ultimately govern how the ions interact with surrounding materials, particularly in the context of corrosion. The following section outlines some of the experimental results that can be used to inform simulations involving MSR fuels. The section begins with a description of atomic scale interactions, followed by the fundamentals of how bulk thermodynamic properties are measured, and contemporary knowledge about the chemistry of the salt-metal interface.

Four primary factors at the salt-metal interface that have been identified as having the greatest implications on corrosion thermodynamics: salt moisture content, the presence of any oxide films, salt impurities, and the redox potential of the salt as assessed by uranium (IV) concentration [32]. However, it is important to reinforce the early-stage knowledge about these four factors. For chloride salts, like for fluoride salts, there is an understanding and evidence that oxides are unstable in molten salts (unlike non-salt typical high temperature operations, where passivation is used as an intentional method for stabilizing alloys) [30, 32]. For an MSR, it is expected that if oxide films form that they will not be stable and will be dissolved by the chlorination process like in the following example reactions [32]:

$$2NiO + ZrCl_4 \leftrightarrow 2NiCl_2 + ZrO_2 \tag{1}$$

$$2NiO + UCl_4 \leftrightarrow 2NiCl_2 + UO_2 \tag{2}$$

$$2FeO + UCl_4 \leftrightarrow 2FeCl_2 + UO_2 \tag{3}$$

$$2Fe_2O_3 + 3CrCl_4 \leftrightarrow 3CrO_2 + 4FeCl_3 \tag{4}$$

Water content in the salt will drive the formation of insoluble metal oxide species in the salt, which may subsequently deposit on alloy surfaces and initiate or accelerate corrosion. Undesired oxide formation can be chemically countered with chloride salt (i.e., $ZrCl_4$, $CrCl_4$, or UCl_4) or metallic (e.g., *Na*) additives to act as reducing agents [32, 189], which convert the oxides into soluble chloride species. Chromium is especially susceptible to corrosion by impurities like *HCl* that can form from the presence of moisture or other corrosion product chlorides that can favorably react with *Cr* metal to form $CrCl_2$. Lastly, excess U^{4+} may be present from UCl_4 additives and can have adverse impacts that facilitate corrosion, by serving as an oxidizing agent, promoting the dissolution of alloy constituents from the metal into the salt. The four primary factors and their associated phenomena are discussed throughout the following sections as they pertain to the metal-salt interface and material compatibility.

2.1.1. Salt State

Atomic scale chemical interactions within a given ionic liquid are determined by atomic-level properties such as ionic radii, polarization strength (hardness), and short- and long-range ion correlations. In the case of salt-fueled MSRs, there is typically a fuel salt (e.g., UCl_3) dissolved within a solvent salt containing one or more constituents (e.g., *NaCl*, $NaCl{-}MgCl_2$, *FLiBe*, etc.). The ionic radii, short- and long-range correlations, ordering, clustering, and aggregation of ions in molten salts are fundamental features that directly impact the bulk and macroscale properties, and ultimately the thermodynamics of corrosion. However, the high-temperature, corrosive nature of molten salts presents challenges for characterizing these properties and efforts are currently being made to explore these features. Hundreds of experimental teams are actively overcoming these challenges, and some of the recent work will be discussed throughout this section.

Atomic radial distribution functions describe the relative probability of finding an atom at a certain distance from another. Atomic radial distribution functions can be collected experimentally by measurements at X-ray and neutron spectroscopy beamlines. Such spectroscopic beam time is a limited resource, and the use of heated radioactive samples at beamlines is not facile. Therefore, computational efforts have been pursued to extract knowledge with fewer experiments; like in the case of UCl_3 and *NaCl* endmembers of the $UCl_3{-}NaCl$ eutectic [33]. Figure 3 illustrates the predicted radial distribution functions for *U−U*, *U−Cl*, and *Cl−Cl* in pure UCl_3 and *Na−Na*,

$Na-Cl$, and $Cl-Cl$ in pure $NaCl$ at 977 °C using large and small supercells. This data provides a wealth of information: one of the major findings is the difference in $Cl-Cl$ distributions because of cation size when comparing Na^+ to U^{3+}.

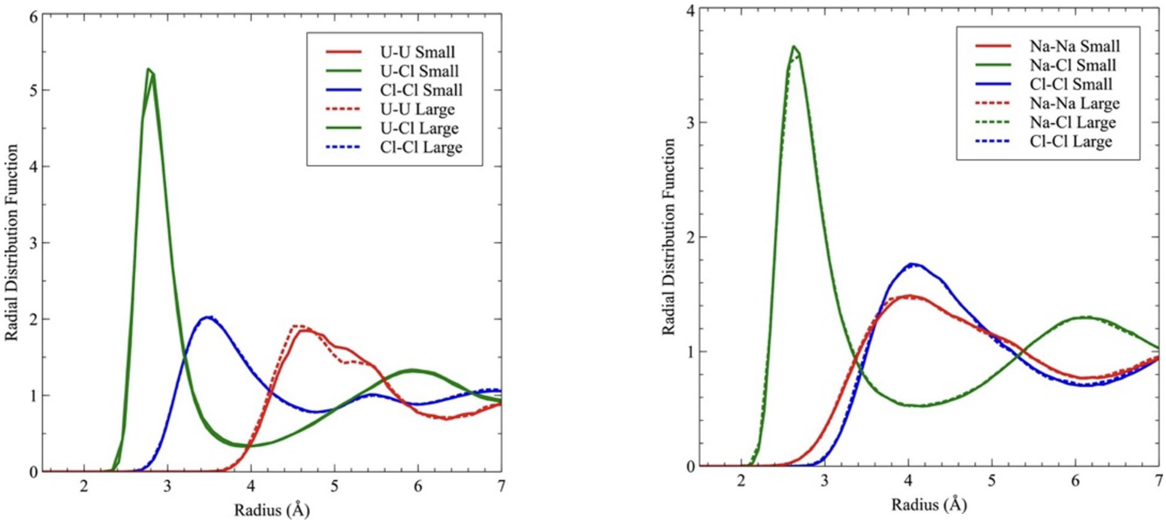

(a) UCl_3

(b) NaCl

Figure 3: The predicted radial distribution function in (a) UCl_3 and (b) $NaCl$ obtained by supercells containing 64 (small) and 216 (large) atoms at 977 ◦C. [33]

Solvent salt cations play a critical role in determining the structure and chemical behavior of the full molten salt, particularly through their influence on ion coordination and the stability of oxidation states. Several studies have been performed to better understand the impact that cations have on coordination [34] and on the oxidation state stability of different species in molten chloride salts [35, 36]. In some cases, it has been suggested that alkaline earth metal solvent salts can exhibit nearly covalent bonding behaviors [35, 37] which would significantly affect how molten salts can be predicted and modeled, especially in the context of corrosion, where the stabilization or destabilization of reactive species is crucial.

In one key study, electrochemical measurements were performed for *Ln* series elements in pure, pseudo-unary molten chloride salts [36]. The primary result was an evident effect on the stability of either higher or lower oxidation states of *Eu*, for example, based on the coordination and ionic radii of the cation comprising the solvent salt. An overview of the findings is described in the cartoon in Figure 4, where the electron density moves either toward or away from the *Eu* ion based on the outer sphere coordination of the solvent salt cation. In the case of KCl, the higher oxidation state of Eu^{3+} was more stable compared to the same measurement performed in $CaCl_2$ where the lower oxidation state of Eu^{2+} was favored. Controlling the oxidation state of fuel salt species such as those containing uranium can have direct consequences on corrosion rates and will be discussed in detail in the following sections. Experimental results are expected to inform strategies for predicting and mitigating corrosion in an operating MSR through adjustments to the salt composition.

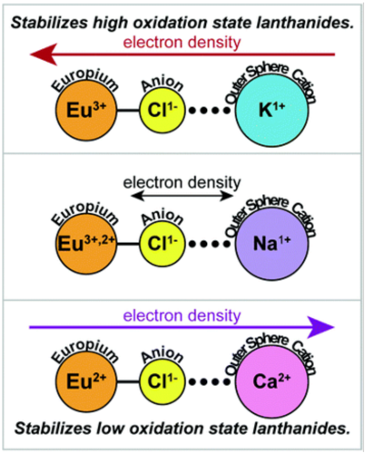

Figure 4: A cartoon illustrating inductive outer-sphere impacts from molten salt cations (K^+, Na^+, and Ca^{2+}) on lanthanide ions using the Eu^{3+}/Eu^{2+} redox couple as a representative example for other lanthanide cations [36].

2.1.2. Thermal Properties

Thermal properties of molten salts are essential for predicting the physical and chemical forms of the salt during reactor operation. Virtually all thermophysical and thermochemical properties are tied into the thermodynamics of the system, specifically focused on the Gibbs free energy of formation which is also intertwined with corrosion behaviors [32, 38]. For example, the Gibbs free energy can be used to calculate and predict the phase (i.e., solid, liquid, gas) in which a given species would exist under specified conditions, and there is a 'general rule' established where, for high temperature applications, the difference between the Gibbs energy of formation between an alloy and salt should be >80 $kJ\ mol^{-1}$ in order to minimize corrosion [32, 39–42]. Similarly, corrosion products like $CrCl_2$ have been thermodynamically evaluated to predict corrosion favorability [43, 44]. The fundamentals of thermodynamic calculations and predictions of molten salts will be discussed more thoroughly in Section 3.

Informative experimental techniques like differential scanning calorimetry (DSC), dilatometry, and viscometry can be challenging to apply to volatile molten salts, especially those bearing *An* series species [45–48]. Methodology has not yet been fully standardized for each thermal property needed to fully understand and predict MSR fuel behavior, but in cases like DSC there are multiple reports in the literature where features like melting point and heat capacity have been successfully determined and corroborated. However, variability in material purity, large experimental uncertainties, and insufficient error analysis in some studies further complicate the interpretation and comparison of results. DSC is an especially important technique given its high sensitivity to heat flow which can inform phase transitions, specifically melting points, and heat capacities of solid and liquid phases. Figure 5 provides examples of pseudobinary phase diagrams of (a) *FLiBe,* which was measured with great care for the MSRE more than 50 years ago, accompanied by (b) a more recent study of the UCl_3–$NaCl$ phase diagram, where the latter used modern instrumentation and techniques to determine the salt composition. The diagram offers details about the system like the lowest melting point at the eutectic (conversion from two phases, like two solid salts, to one phase, like a homogenized liquid) and where combined existences of solid+liquid phases will occur. Additionally, higher-order systems like pseudoternary salts can be described using liquidus projection plots, like those shown in (c) and (d) in Figure 5 for *LiF*–*NaF*–*KF* (or '*FLiNaK*') and UCl_3–$NaCl$–$MgCl_2$ where the temperatures indicated across the triangular diagram describe the melting point for a given ratio of the three salts. Many datapoints are required to fully build even the pseudobinary phase diagrams. In these cases, experimental data can heavily inform these plots and arguably provide the most reliable information, but computational support can more quickly fill in data points (when able). Thus, phase diagrams can be achieved most rapidly when the experimental-computational cycle is active. This relationship will be discussed in more detail in Section 2.1.4.

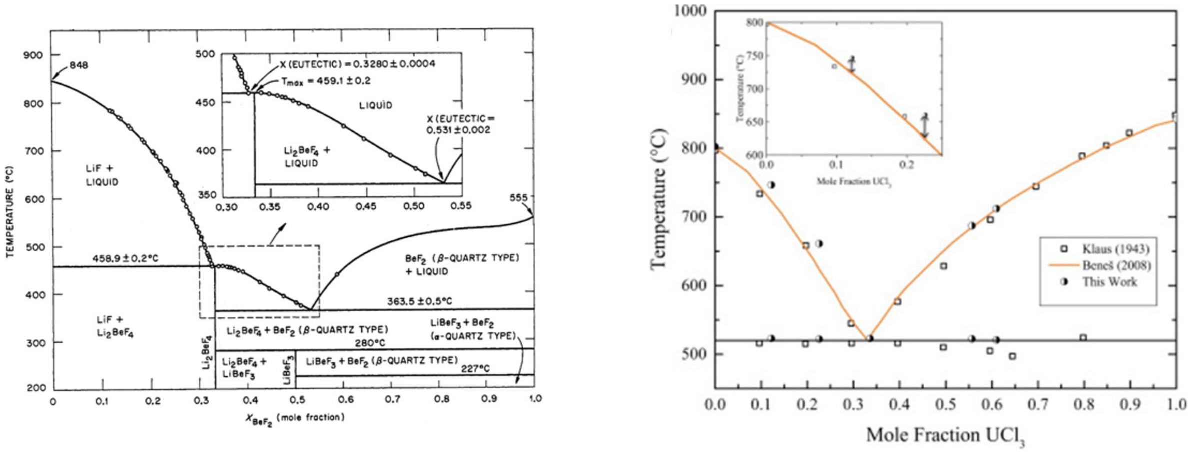

(a) $LiF-BeF_2$ (b) UCl_3-NaCl

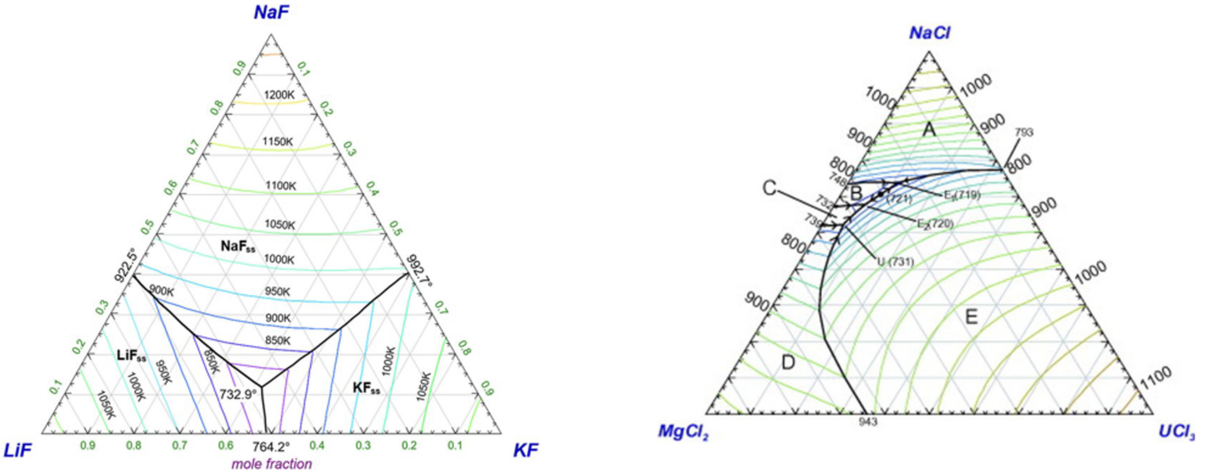

(c) $LiF-NaF-KF$ (d) $UCl_3-NaCl-MgCl_2$

Figure 5: Experimentally determined pseudo-binary phase diagrams for (a) $LiF-BeF_2$ [49] and (b) UCl_3-NaCl. [27] Computationally determined liquidus projection plots for (c) $LiF-NaF-KF$ [50] and (d) $UCl_3-NaCl-MgCl_2$. [28]

Measurements of fundamental thermal properties for *An*-bearing MSR fuel salts, specifically focusing on the UCl_3-NaCl eutectic or near-eutectic composition, have recently been made. For example, preliminary data for the melting point, liquidus heat capacity, and thermal diffusivity of 34.2-65.8 mol% UCl_3-NaCl has been documented in [47]. The DSC measured thermograms for the phase transition and DSC measured heat capacities are shown in Figure 6 (a) and (b), respectively. The thermal diffusivity values across 596-798°C from laser flash analysis (LFA) are plotted in (c). The average values for each of these three measurements are listed in Table 2.

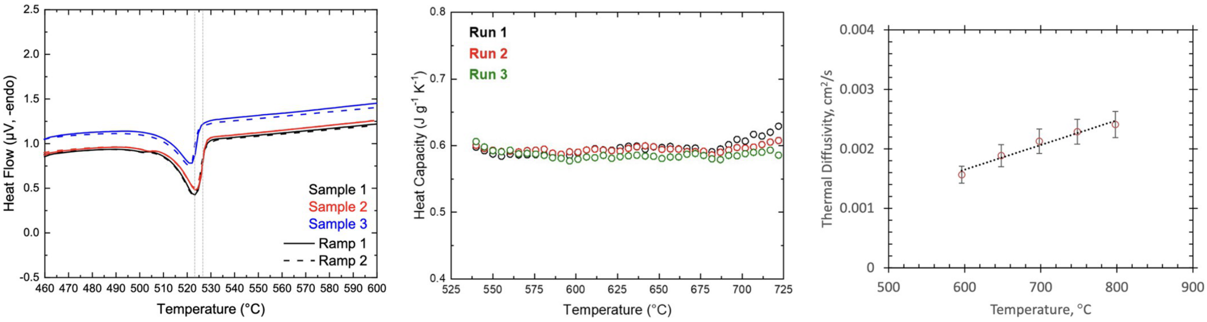

(a) (b) (c)

Figure 6: (a) DSC responses of three samples of $NaCl–UCl_3$ salt, (b) heat capacity values for molten $NaCl–UCl_3$, and (c) thermal diffusivity values of $NaCl–UCl_3$. [47]

Table 2: Average melting point, heat capacities, and thermal diffusivities for $NaCl–UCl_3$ [47]

Melting Point	
Ave. Onset T (°C)	**Ave. Endpoint T (°C)**
510.7	526.6
Heat Capacity	
T (°C)	**Ave. C_p (J/g*K)**
550	0.591
600	0.586
650	0.591
700	0.597
Thermal Diffusivity	
T (°C)	**Ave. Thermal Diffusivity (cm^2*s^{-1})**
596	0.0016
648	0.0019
698	0.0021
748	0.0023
798	0.0024

Another important case study, conducted by INL, was recently made publicly available for the $UCl_3–PuCl_3–NaCl$ system [51]. That study is of exceptionally high quality, based on high-purity materials, and used robust methodology and analysis, making the study a valuable contribution to the field. Building on that study, the Department of Energy (DOE) MSR Campaign is now supporting complementary efforts at other national laboratories, including LANL, to expand the thermal property dataset for An-bearing salts. Inter-laboratory validation is a key objective of these efforts, which leverage the unique capabilities and infrastructure of the national laboratory system. The INL report describes that thermal properties were affected by compositional changes, specifically when adding Pu to 67-33 mol% $UCl_3–NaCl$ to create a 30-9-61 mol% $UCl_3–PuCl_3–NaCl$ mixture. The melting point, or liquidus transition, had been hypothesized by the authors to decrease upon addition of the Pu, but instead increased from ~520 °C to ~550 °C. This liquidus temperature did remain below the 576 °C liquidus transition associated with the alternative composition of 61NaCl–39UCl_3 (mol%), The density was also observed to change, following the expected trend that the addition of actinide species increases the overall density. This work also included preliminary results from their microloop, through which $PuCl_3–NaCl$ (36-64 mol%) flowed for over

1,000 hours. In this case, they measured thermal property changes to the salt after $NaCl–MgCl_2$ was introduced, to create an overall mixture of 10-64-26 mol% $MgCl_2–NaCl–PuCl_3$. Compared to the *Pu*-bearing pseudobinary salt, the thermogram from DSC to determine the melting point showed a decreased onset temperature from 449 °C to 398 °C. Similarly, the density decreased after the addition of the flush salt from a linear trend described by $\rho(T) = 3.86$ g cm^{-3} - 9.50×10^{-4} (g cm^{-3} °C^{-1})×T to a linear trend described by $\rho(T) = 3.50$ g cm^{-3} - 9.23×10^{-4} (g cm^{-3} °C^{-1})×T, where T is the temperature in °C. These changes are important findings when considering the overall performance of chloride fuel salts and have direct impacts on the corrosion thermodynamics and kinetics of a given system, but more work is needed to fully understand *An*-bearing molten chloride salts for MSR fuels.

2.1.3. Salt-Metal Interface Properties

Understanding material compatibility with molten chloride salts begins at the interface between the alloys comprising the containment of fuel or coolant. However, the interactions between solid metal and liquid salt are not yet well understood due to the challenges of corrosion experiments and complexity of modeling such environments. Factors like salt composition and purity, flow and circulation within a loop system, and the composition and morphology of the solid surface can all influence the salt-metal interface and subsequent corrosion. Mechanisms that determine which interactions occur at the interface include heterogeneous redox reactions (solid/liquid reactions or soluble/insoluble phase reactions), species adsorption to the surface, and diffusion or double layer structure.

The Gibbs free energy of species in molten salts heavily dictates the favorability of corrosion of a metal. Gibbs free energy tabulations and calculations thus allow for predictions of which alloy components (elements) are most likely to be prone to attack, and these are, *W*, *Mo*, *Ni*, *Co*, *Fe*, *Nb*, *Cr*, *Mn*, *Ti*, *Zr*, and *Al* [18, 23]. Thermodynamics can be exploited to better understand the implications of the oxygen activity, or the 'oxoacidity', on corrosion mechanisms at the salt-metal interface. Like traditional Pourbaix diagrams used to predict the oxidation state of a species based on the redox potential (E°) across a *pH* range [52], oxo-acidity is guided by the influence of oxygen activity or pO_2 on the thermodynamic stability of different species in molten salts. This approach has a longer history of use in studies on aqueous contamination of chloride salts, with this approach expanded in recent years to incorporate anticipated oxidation states of complex salts that can inform the speciation of cations likely to be involved in corrosion [30, 53]. Oxoacidity can help to identify "immunity domains", which are regions of the composition diagram where corrosion is not expected to occur, providing a guide for navigating the formation of oxides from metals or conversion of alloying elements to ionic species in the salt (e.g., to metal-chloride salts), based on specific combinations of E° and pO_2 in the system, at a given temperature and composition [26, 30]. For example, a recent study used a combination of computational and experimental approaches to develop thermodynamic diagrams for the oxoacidity of common corrosion products in $NaCl–UCl_3–PuCl_3$.

Figure 7(a) and (b) illustrates the region of stability of Pu^{3+} and U^{3+}, respectively, in *NaCl* (vs. the Cl_2/Cl^- reference potential) across a range of activity for the oxide form of the solvent salt cation, $p(Na_2O)$. Figure 7(c) illustrates the overlapping region where Pu^{3+} and U^{3+} would be stable in the combined form of $NaCl–UCl_3–PuCl_3$ (80-10-10 mol%). Finally, similar calculations were performed for *Cr*, *Fe*, and *Ni* oxoacidity and overlain with the stable region for the pseudoternary system to determine which forms of each corrosion product would be expected to coexist; Figures 7(d), (e) and (f). For all three corrosion products, the diagrams indicate that both their ionic forms (chlorides) and reduced forms (metallic) would be stable, and the diagrams provide guidance for combinations of E° and $p(Na_2O)$ that would help to ensure the energetics of these corrosion prone elements favor their metallic states to minimize corrosion. Salt composition has been found to be the dominant factor in the likelihood of corrosion of materials in contact with a molten chloride salt, both through contaminants that will drive oxidation of metals and buffers that can be added to mitigate those reactions. Multi-oxidation state species like chromium which can oxidize to either the 2+ or 3+ state can be involved with redox reactions at the salt-metal interface that ultimately result in corrosion. F-block species (particularly U^{4+}) could potentially have a significant effect on corrosion given their prevalence as fuel and transmutation products in MSRs [18, 21, 23]. Additionally, impurities like moisture and metallic halides have been shown to drive or influence corrosion rates by orders of magnitude in some cases (see Figure 1 in Raiman & Lee, 2018) [22].

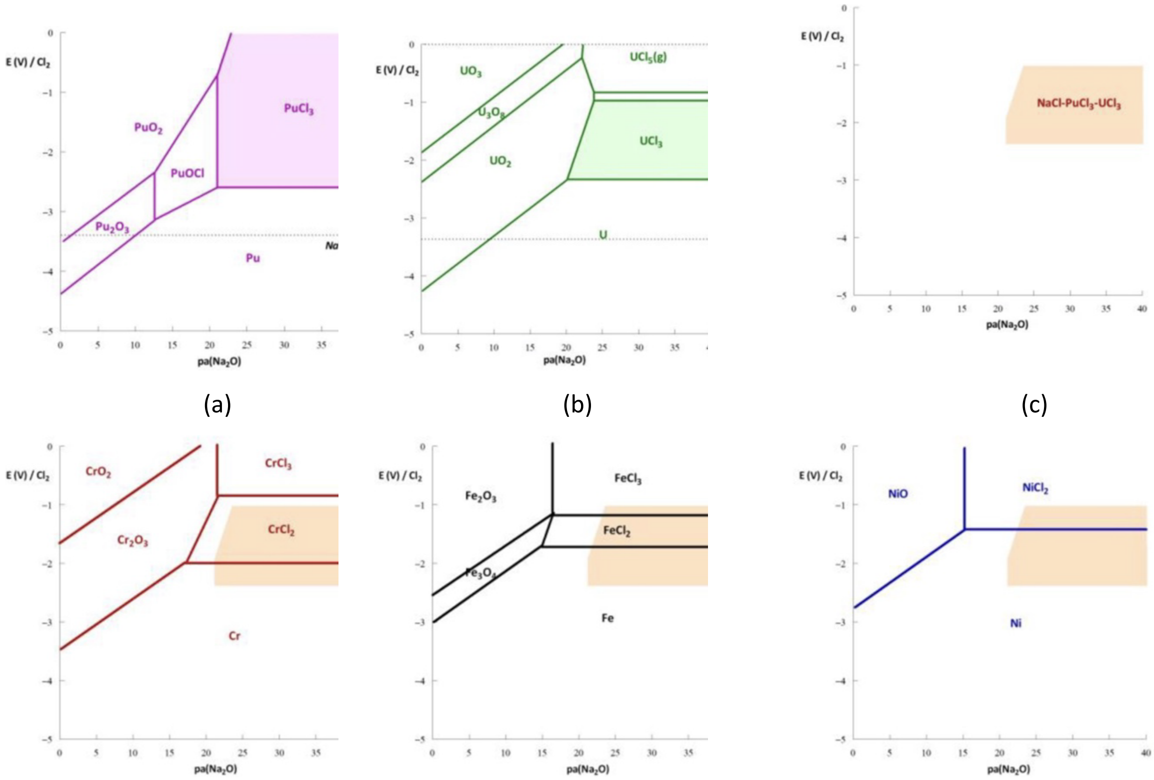

(a) (b) (c)

(d) (e) (f)

Figure 7: (a)–(c) Thermodynamic diagrams of plutonium (a), uranium (b), and the salt $NaCl–UCl_3–PuCl_3$ (80–10–10 mol%) (c) at 600 °C in *NaCl*-based chloride media. Mole fractions were taken as 10 mol% for these examples [30]. (d)–(f) Thermodynamic diagrams of *Cr* (d), *Fe* (e), and *Ni* (f) in *NaCl*-based molten salt at 600 °C. The orange domain corresponds to the stability domain of the $NaCl–UCl_3–PuCl_3$ (80–10–10 mol%) mixture. $a(MCl_2) = 10^{-6}$ (M = *Cr*, *Fe*, and *Ni*) [30].

Another essential component to describe the salt-metal interface is the electrochemical double layer (EDL), which can be considered to include the region of the salt where redox reactions with the solid surface will occur. EDLs are well understood in traditional aqueous electrochemistry measurements but have not been thoroughly investigated for molten salt electrolytes [31, 54–59]**.** The experimental efforts to understand the double layer in molten salts are largely limited to the 1990s and earlier [54–57], and the more modern discussions are virtually exclusively based on modeling and simulations [31, 58, 59].

Frischknecht et al. clearly described the discrepancies between the well-understood structure of the EDL in aqueous systems and the unknown environment of molten salts [31]. They explained that corrosion mechanisms at the salt-metal interface are entirely dependent on the structure and behavior of the species within the double layer near the material surface. The standard theory for aqueous systems follows a mean-field theory outlined by Gouy-Chapman which assumes the coulomb interactions dominate ion behavior by describing the ions simply as point charges and thus approximates the electrostatic potential as a smoothly varying field that does not depend on the local configurations of the atoms/molecules in the fluid. With this approximation, a diffuse layer at the surface has the greatest charge density which decreases with distance until the bulk solution is reached. The total charge in the inner layer (Inner Helmholtz Plane, IHP) of the diffusion layer has a measurable capacitance that exists as a function of the overall surface potential. However, in molten salts, the finite size and strong correlations of the ions in the system invalidate the Gouy-Chapman theory because the density profiles of said ions become oscillatory near the charged surface (metal) and fundamentally changes the structure of the double layer [31]. Note however that more refined mean field models can capture the oscillatory charge distributions near the sale metal interface but not quantitatively. Better understanding of EDLs adjacent to conductive materials in molten salts will facilitate more accurate descriptions of corrosion and thus facilitate corrosion prediction and control.

2.1.4. Experimental-Computational Cycle of MSR Fuel Chemistry

The continuous cycle of experimental data collection used to feed calculations and simulations that can, in turn, inform future experimental needs is not an approach unique to MSR technology, but it is especially challenging given the complexity of high-temperature ionic liquids that are difficult to measure and to computationally model. DOE funded work has developed a database of thermophysical and thermochemical properties of halide compounds important to MSR modeling and predictions through the Molten Salt Thermal Properties Database (MSTDB). MSTDB has data files for thermophysical (TP) and thermochemical (TC) properties of An, Ln, FPs, and corrosion products in their chloride and fluoride forms as pseudounary, pseudobinary, pseudoternary, and even pseudoquaternary species using data available in the literature [60, 61]. These databases are being used in various modeling and simulation programs to predict corrosion kinetics. Figure 8 presents an illustration of the many different facets of molten salt corrosion that could leverage these databases [62]. Briefly, the thermophysical properties of the MSTDB could inform the bulk mass, momentum, and energy transport information for thermal hydraulics considerations while the thermochemical properties provide a foundation for the thermochemical state of the fuel salt through Gibbs energy minimization. Each of these properties can then be used to inform species transport, reactor physics, surface behavior, and component interface either directly or indirectly.

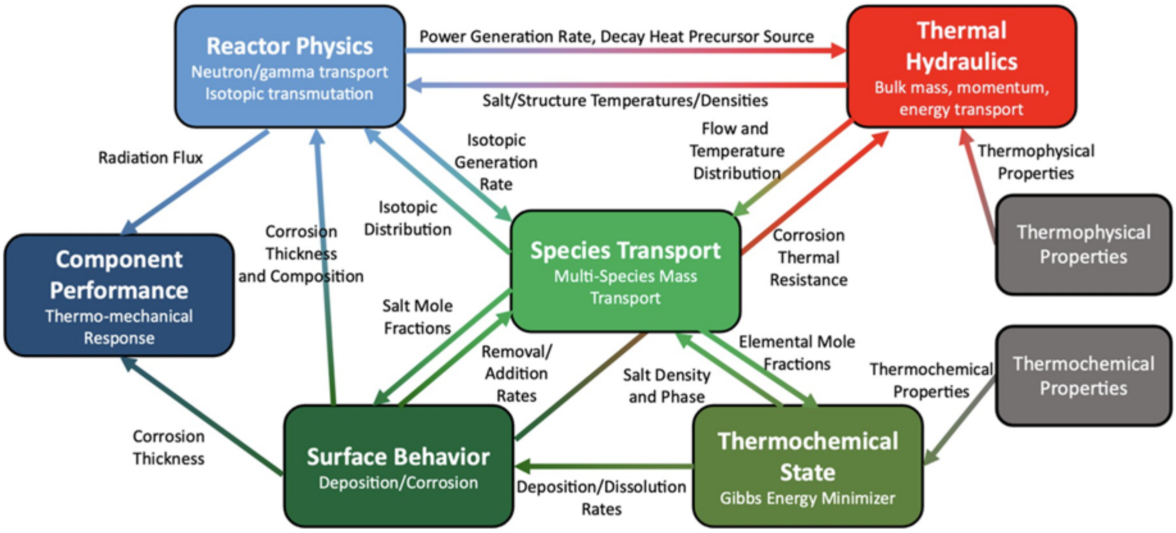

Figure 8: Physical phenomena in MSR systems addressed by modeling and simulation codes, along with the interrelationships among them [62]

MSTDB-TP uses experimental data for density (ρ), viscosity (μ), thermal conductivity (k), and heat capacity (C_p) to generate data files that can be used for predictive models and simulations of MSR fuel and coolant systems. Of the 799 unique entries available in MSTDB-TP (v3.0), those relevant to the present work are listed in Table 3 [60]. The thermophysical properties in the MSTDB are useful for understanding the intrinsic properties of MSR fuel salts, like those described in Section 2.1.1, ultimately influencing corrosion kinetics.

The MSTDB-TC uses thermodynamic calculations rooted in the Computer Coupling of Phase Diagrams and Thermochemistry (CALPHAD), which is a robust, well-developed methodology for predicting phase diagrams and thermodynamics, which in turn enables certain calculations for chemical kinetics and other features of multi-component systems [63]. CALPHAD is also the framework within which the MSTDB-TC data files can be used to predict the stable phases and forms of MSR-relevant species that will exist under specified operating conditions. The data files from the MSTDB-TC can be used with commercial software like Fact Sage and open-source equilibrium codes like Thermochimica and PyCalphad. The systems relevant to this report which are available in MSTDB-TC (v4.0) are listed in Table 3 and blue portions represent gaps in the database. The database continues to be updated to improve outputs, as new results are published, but is somewhat limited by the availability of reliable experimental data.

Table 3: Available data for pure components, pseudobinary compositions, and pseudoternary compositions of chloride salts relevant to material compatibility in MSRs and available in the current version of the MSTDB-TP. Systems are described via the number of available reports for density (ρ), viscosity (μ), thermal conductivity (k), and heat capacity (Cp) [60]. Blue cells mean that data is not available

Salt(s)	Density (ρ)	Viscosity (μ)	Thermal Conductivity (k)	Heat Capacity (C_p)
Pure Components				
LiCl	1	1	1	1
NaCl	1	1	1	1
KCl	1	1	1	1
$MgCl_2$	1	1	1	1
UCl_3	1	🟦	🟦	1
UCl_4	1	🟦	🟦	🟦
$PuCl_3$	🟦	🟦	🟦	1
Pseudobinary Compositions				
LiCl-NaCl	6	🟦	🟦	🟦
LiCl-KCl	5	6	🟦	🟦
LiCl-UCl_3	10	🟦	🟦	🟦
LiCl-UCl_4	14	🟦	🟦	🟦
NaCl-KCl	6	6	🟦	🟦
NaCl-$MgCl_2$	10	8	🟦	🟦
NaCl-$ThCl_4$	13	🟦	🟦	🟦
NaCl-UCl_3	8	🟦	🟦	🟦
NaCl-UCl_4	8	🟦	🟦	🟦
NaCl-$PuCl_3$	2	🟦	🟦	🟦
KCl-$MgCl_2$	13	8	1	1
KCl-UCl_3	16	1	🟦	🟦
KCl-UCl_4	12	🟦	🟦	🟦
UCl_3-UCl_4	11	🟦	🟦	🟦
Pseudoternary Compositions				
LiCl-NaCl-KCl	4	🟦	🟦	🟦
LiCl-NaCl-UCl_3	18	🟦	🟦	🟦
LiCl-NaCl-UCl_4	18	🟦	🟦	🟦
LiCl-KCl-UCl_3	18	🟦	🟦	🟦
LiCl-KCl-UCl_4	18	🟦	🟦	🟦
LiCl-UCl_3-UCl_4	21	🟦	🟦	🟦
NaCl-KCl-UCl_3	18	🟦	🟦	🟦
NaCl-UCl_3-UCl_4	26	🟦	🟦	🟦
KCl-UCl_3-UCl_4	32	🟦	🟦	🟦
Totals		314	33	5

For this type of continuous improvement process, Bayesian parameter estimation methods [221] are currently not used in MSTDB-TC, but a similar approach has been successfully applied to gas phase thermodynamics databases [222-225]. It is possible that Bayesian parameter estimation methods will be incorporated into MSTDB-TC in the future, and the concept has been discussed in technical workshops.

Table 4: Available data for pseudobinary, pseudoternary, and pseudoquaternary chloride salts relevant to material compatibility for MSRs available in version 4 of the MSTDB-TC [61, 64]

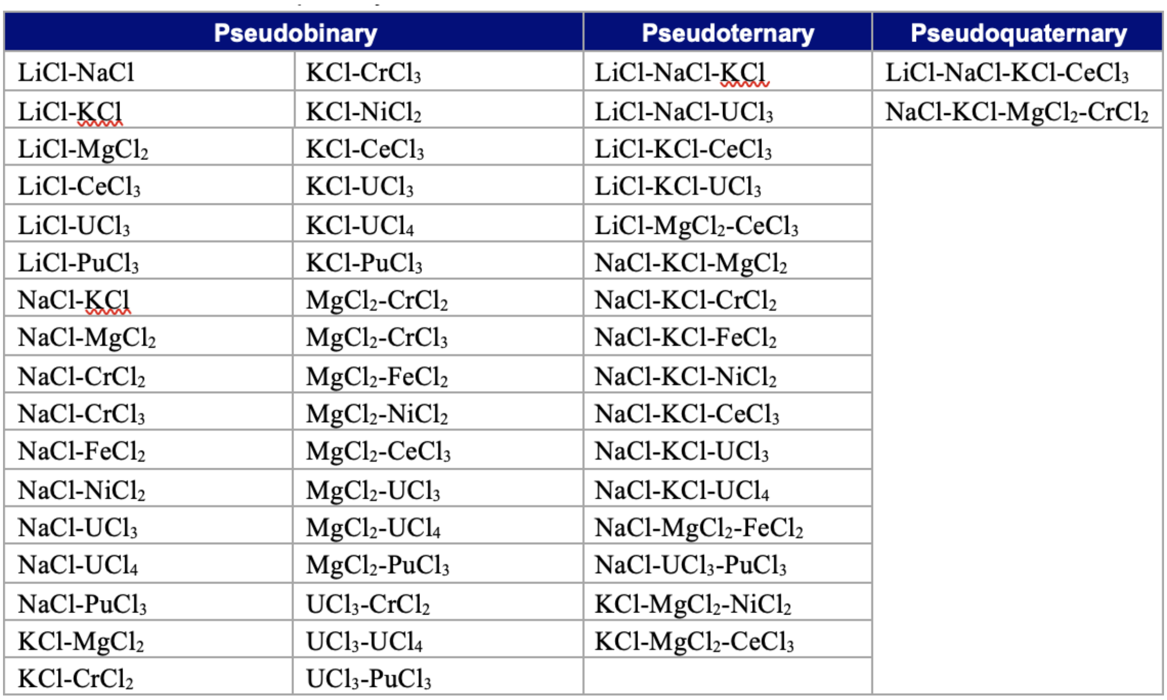

Pseudobinary		Pseudoternary	Pseudoquaternary
LiCl-NaCl	$KCl-CrCl_3$	LiCl-NaCl-KCl	$LiCl-NaCl-KCl-CeCl_3$
LiCl-KCl	$KCl-NiCl_2$	$LiCl-NaCl-UCl_3$	$NaCl-KCl-MgCl_2-CrCl_2$
$LiCl-MgCl_2$	$KCl-CeCl_3$	$LiCl-KCl-CeCl_3$	
$LiCl-CeCl_3$	$KCl-UCl_3$	$LiCl-KCl-UCl_3$	
$LiCl-UCl_3$	$KCl-UCl_4$	$LiCl-MgCl_2-CeCl_3$	
$LiCl-PuCl_3$	$KCl-PuCl_3$	$NaCl-KCl-MgCl_2$	
NaCl-KCl	$MgCl_2-CrCl_2$	$NaCl-KCl-CrCl_2$	
$NaCl-MgCl_2$	$MgCl_2-CrCl_3$	$NaCl-KCl-FeCl_2$	
$NaCl-CrCl_2$	$MgCl_2-FeCl_2$	$NaCl-KCl-NiCl_2$	
$NaCl-CrCl_3$	$MgCl_2-NiCl_2$	$NaCl-KCl-CeCl_3$	
$NaCl-FeCl_2$	$MgCl_2-CeCl_3$	$NaCl-KCl-UCl_3$	
$NaCl-NiCl_2$	$MgCl_2-UCl_3$	$NaCl-KCl-UCl_4$	
$NaCl-UCl_3$	$MgCl_2-UCl_4$	$NaCl-MgCl_2-FeCl_2$	
$NaCl-UCl_4$	$MgCl_2-PuCl_3$	$NaCl-UCl_3-PuCl_3$	
$NaCl-PuCl_3$	UCl_3-CrCl_2	$KCl-MgCl_2-NiCl_2$	
$KCl-MgCl_2$	UCl_3-UCl_4	$KCl-MgCl_2-CeCl_3$	
$KCl-CrCl_2$	UCl_3-PuCl_3		

There are several *An* halides with a relative lack of experimental results for populating both MSTDB-TP and -TC. This report also serves to identify recent reports of *U* and *Pu* chloride salt measurements that are not yet reflected in MSTDB, and which could also be used to improve computational investigations of molten salt fuel chemistry.

2.2. Material Compatibility

Material compatibility is dictated by the fundamental corrosion chemistry and redox mechanisms at the salt-metal interface and by transport kinetics in the salt and in the metal (particularly at grain boundaries), which is ultimately dictated by the environmental conditions. There are multiple, modern comprehensive reviews that have been published covering corrosion of MSR-relevant alloys in alkali or alkaline earth halides [18–23], including reports issued by the NRC [8–12]. However, studies with more complex systems like those containing *An* fuel components have not been readily available until recently. Corrosion studies of *U*- and *Pu*-bearing chloride salts have since been published and are discussed in the following section in addition to a collection of recent studies on the corrosion products of interest. Following that discussion, the MSR community's understanding of corrosion in molten chlorides is compared to that of molten fluorides, with the aim of identifying key differences and evaluating how insights from each system can inform the other.

2.2.1. Corrosion Chemistry

2.2.1.1. Solid Diffusion and Migration Kinetics

The chemical kinetics of corrosion and any associated chemical diffusion are essential to our understanding of corrosion and involves both the metallic constituents within the alloy and ionic species within the salt. Within the solid, kinetics and diffusivity are intertwined concepts as they describe the movement of metallics within the alloy. This process is greatly impacted by factors like temperature and overall alloy composition. This temperature dependency for diffusion of metal atoms in the alloy can be described by an Arrhenius-type equation:

$$D = D_o e^{-\frac{Q}{RT}} \tag{5}$$

$$\log(D) = -\frac{Q}{2.3RT} + \log(D_o) \tag{6}$$

where D_o is the temperature-dependent pre-exponential or frequency factor and related to the activation energy (Q), gas constant (R), and temperature (T). 'Self-diffusion' coefficients have been measured for Cr migrating throughout Ni-alloys. These were determined to be on the order of 10^{-20} to 10^{-16} $m^2 \cdot s^{-1}$ at 600 °C and 900 °C, respectively [32, 66]. Additionally, it was determined that, at least for *Cr* diffusion, the operating temperature range for MSRs (approximately 600 –750 °C), grain boundaries served as the primary pathways for movement through the alloy [32,65]. While *Cr* has been well-studied as a species known to migrate through a solid due to corrosion at the metal-salt interface, other corrosion products have not been equally discussed in the literature, and the associated corrosion chemistry is not as well understood.

2.2.1.2. Ionic Diffusion and Electron Transfer Kinetics

Ionic species also diffuse at the salt-metal interface due to concentration and potential gradients within the double layer, and the kinetics of the electron transfer can be calculated using electroanalytical techniques. Voltammetry, or the measurement of current as a function of sweeping potential, can be used to observe oxidation and reduction processes *in situ*. In cyclic voltammetry (CV) the electric potential is cycled repeatedly across a given window, so both oxidation and reduction reactions are observed. CV is typically performed using a three-electrode cell where the electric potential is applied and electric current is measured at the working electrode (WE), the circuit is completed at the counter electrode (CE), and the reference electrode (RE) provides a standard redox reaction to serve as the half-cell complementing the reaction being measured at the WE. In some cases, a quasi-reference electrode is used rather than a thermodynamic reference electrode [12]. There are multiple approaches to calculating the electron transfer rate constants that have been reported in the literature.

The Nicholson method for determining the heterogeneous electron transfer rate constant (*k*) is a common method used for aqueous, room temperature systems but has been used for molten salts as well. This methodology uses a simple estimation based on the distance between the oxidation and reduction peaks determined using voltametric techniques but assumes symmetry and true reversibility in the system using Equation 7 [67, 68].

$$\psi = \frac{k\left(\frac{D_O}{D_R}\right)^{\frac{\alpha}{2}}}{\sqrt{\frac{\pi D_O \nu n F}{RT}}} \tag{7}$$

This relationship takes the diffusion coefficients of the oxidized and reduced species ($D_{O/R}$) to the half-power of the charge transfer coefficient (α) in combination with the scan rate (ν), number of electrons involved in the redox reaction (n), Faraday's constant (F), the ideal gas constant (R), and temperature (T) to create a function of the peak separation constant kinetic parameter (ψ) and k. However, the estimation (see Table 1 in R[67]) has been reported to be only usable up to peak separations of 212 mV per electron transferred, and the peak separations found in molten salts often exceeds this value due to factors like temperature and the different sources of resistivity in the cell. Therefore, adaptations have been proposed by Kuznetsov et al. and tested by others where values in a typical range for electron transfer (on the order of 10^{-3}–10^{-2} *cm/s*) are produced using a standardization of the peak separation (ΔE_p) shown in Equation 8 and Equation 9 [68–72].

$$\Delta E_{p,298} = \frac{\Delta E_{p,T} \cdot 298}{T} \tag{8}$$

$$\psi_T = \psi_{298}\sqrt{\frac{T}{298}} \tag{9}$$

Additionally, the true reversibility of the reaction must be determined to accurately incorporate the charge transfer coefficient. In ideal scenarios, like some common aqueous analytes, α can be assumed as 0.5, but molten salt redox chemistry, especially for corrosion, is rarely ideal. Manually calculating α can be performed using Equation 10 by relating it to the difference between a given peak potential and the 'half-peak potential' which describes the potential where the current is half of the total peak current value $E_{p,\frac{a}{c}} - E_{\frac{p,\frac{a}{c}}{2}}$.

$$\alpha n_\alpha = \frac{1{,}857RT}{\left|E_p - E_{\frac{p}{2}}\right| F} \tag{10}$$

However, this approach should be limited to soluble-soluble redox reactions where both oxidation states are ionic species in the liquid phase (e.g., $U^{4+/3+}$), while the corrosion process involves soluble - insoluble reactions since the reduced oxidation state exists in the solid phase within the alloy (e.g., $Cr^{2+/0}$). An alternative calculation can be made using the process instead outlined by Klingler-Kochi (Equation 11), where $E_{p,c/a}$ refers to the peak potentials for the anodic, or oxidation, and cathodic, or reduction, reactions which is not reliant on the uniformity of oxidation and reduction in a single voltammogram and has proven effective for less-than-reversible redox reactions, including for use in molten salts [72–76].

$$k = 2.18\sqrt{\frac{D_O(\alpha n_\alpha)\nu F}{RT}}\,e^{\frac{\alpha^2 nF}{RT}(E_{p,c}-E_{p,a})}$$

(11)

Therefore, in molten salts, where a set of materials from the alloys of construction act as an electrode, the induced redox of corrosion products and oxidizing agents can give insights into the electron transfer mechanisms during corrosion processes.

Similarly, the traditional electroanalytical determination of diffusion coefficients, like that of Randles-Sevcik (Equation 12 where *A* represents the electrode surface area and *C* is the concentration in mol/mL) [77],

$$i_{p,\frac{a}{c}} = 2.69 \times 10^5 \cdot AC\sqrt{n^3 D_{\frac{R}{O}}\nu}$$

(12)

describes the movement of oxidized and reduced species away from the surface of an electrode (or surface in the case of corrosion) but are limiting when applied to complex molten salt systems. Again, the quasi-reversibility of the reaction is better described by a modified equation: the Berzins-Delahay equation in Equation 13 has been useful for non-trivial systems like f-block redox couples, in molten salt systems, or both [71, 72, 74, 75, 76, 78, 79].

$$i_{p,\frac{a}{c}} = 0.496nFAC\sqrt{\frac{D_{\frac{R}{O}}(\alpha n_\alpha)F\nu}{RT}}$$

(13)

This technique can also be useful in describing how a corrosion product may diffuse away from an alloy during dissolution into the salt following a corrosion event.

Corrosion rates for salt systems relevant to MSR fuels, specifically for salts containing *An* elements like *U* and *Pu*, are described in the publications described in the next section. The experimental approaches available in the literature vary between static or flowing salt exposure, with a few select examples of relevant *in situ* measurements. Ultimately, there is a need to further explore the aforementioned electroanalytical methods for these salt systems to better understand the diffusion and kinetics of their interactions with structural materials.

2.2.1.3. $AnCl_x$-Chloride Corrosion Studies

The information provided about the corrosion in the presence of salts containing *An* elements is primarily from analysis of pre- and post-characterization techniques of materials that have experienced prolonged exposure to molten salts ("exposure tests" with alloy coupons), as opposed to *in situ* electrochemical techniques. The pseudobinary $AnCl_x$–$NaCl$ system is of significant interest given the proposed use of UCl_3–$NaCl$ [32]. It is beneficial to explore other relevant systems for an operating MSR like UCl_4–$NaCl$ and $PuCl_3$–$NaCl$; some work has been recently published on these salts. The importance of minimizing the concentration of U^{4+} has been acknowledged in this system, specifically [32, 80]. Limited studies in the literature propose perform *in situ* measurements of corrosion using the electroanalytical techniques described previously for An-bearing chloride salts [85]. Additional experimental data would be beneficial to better understand the potential for chloride salt corrosion in MSRs.

However, one of the only available discussions about corrosion expectations in the UCl_3–$NaCl$ system is rooted in computational efforts like lower length scale modeling of properties like density, coordination number, and radial distribution functions [81]. Their comprehensive investigation describes predicted behavior of $CrCl_2$ and $CrCl_3$ as expected corrosion products in a chloride salt-fueled MSR. In a 31.25 mol% UCl_3 composition, they simulated corrosion mechanisms of the pseudobinary salt in the presence of Cr chlorides to include changes in thermal properties and coordination. When $CrCl_2$ was introduced, they found an increase in density (for up to 13.5 mol% $CrCl_2$) from $3.86 - \frac{0.78}{1000}T$ to $4.03 - \frac{0.97}{1000}T$. They also found that *Cr* complexes become connected to the *U* network of ions within the liquid salt, but does not significantly alter the coordination environment of *U*. While this indicates that *U*–*Cr* complexes are prominent in the network structure of mixtures, more experimental efforts are needed to fully understand this system at the atomistic scale. Their efforts to simulate the addition of $CrCl_3$ to UCl_3–$NaCl$ were more challenging and were more computationally expensive. The results showed a very different coordination environment from the $CrCl_2$ additions, and it was difficult to produce a purely $CrCl_3$-containing system because of the favorability to reduce to $CrCl_2$. The calculations indicate that equilibrium was not reached, and the reaction, $UCl_3 + CrCl_3 = UCl_4 + CrCl_2$, should be considered.

By introducing $CrCl_3$ into the system, which may be expected following what is known of *Cr* migration through alloys along grain boundaries and subsequent leaching into salts, it can interact with the UCl_3 present in the fuel salt to reduce the *Cr* and oxidize the *U* to produce a more stable $CrCl_2$ and more corrosive UCl_4. If this spontaneous reaction and change in density (and likely other thermal properties) really occurs, it is an important finding for corrosion prediction and would benefit from further experimental confirmation.

The microloop of $PuCl_3$–$NaCl$ (36-64 mol%) at INL has also produced valuable preliminary data about the corrosion of the containment material (Inconel alloy 625: $Ni/Cr_{20-23}/Mo_{8-10}/Fe_5/(NbTa)_{3.15-4.15}/Co_1$ wt% among other minor components) after over 1,000 hours of operation [82]. They described the impacts of planar and radial samples along the hot leg (700 °C) and cold leg (557 °C) of the loop. On the hot leg they observed *Cr* depletion, pitting to approximately 2 μm into the wall (shown in the micrographs in Figure 9), and the presence of corrosion products (*Cr*, *Fe*, *Ni*, *Mo*, and *Nb*) observed using scanning electron microscopy (SEM) energy dispersive X-ray spectroscopy (EDS). Additionally, a thin metallic layer of U (present as an impurity) and *Pu* metals co-deposited on the planar portion of the hot leg sample, but the radial samples did not experience metallic *An* deposition, only 2-3 μm pitting.

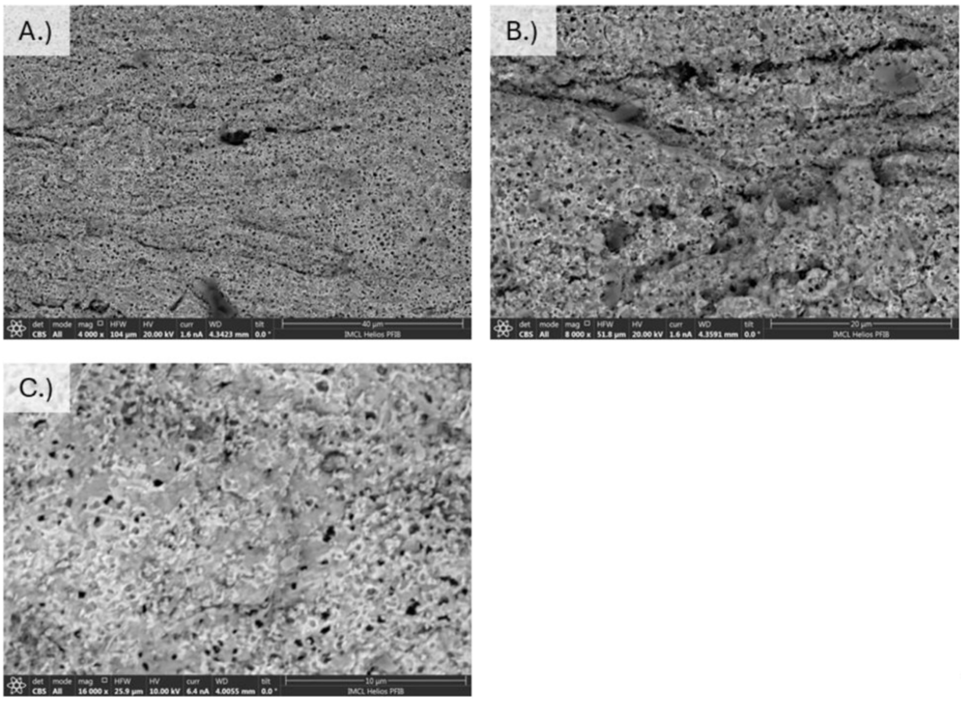

Figure 9: Different magnifications at an area of interest on a hot leg planar sample indicating the presence of pits or cavities in the microloop Alloy 625. [82]

The cold leg portion of the loop showed a 13 μm deep film or deposit on the planar sample that was neither uniform or consistent but was seemingly rich with *Cr* and *Fe* corrosion products in addition to *Pu* (but no U metal). No *U* or *Pu* was observed on the radial samples, and little-to-no corrosion was observed on either geometry of the cold leg samples. Ultimately the corrosion was minimally observed following the 1,000 hours operation of the microloop and was exclusive to the hot leg portion.

There are also several publications available in the literature describing multi-component An-bearing molten chloride salts, specifically studying the effects of material exposure to $NaCl{-}KCl{-}UCl_3$. In one study, multiple alloys were exposed to the $NaCl{-}KCl$ eutectic (50-50 mol%) doped with 6 wt% UCl_3 at 750 °C for 30 hours and analyzed the rates of corrosion using both gravimetric and X-ray fluorescence spectroscopic techniques [83]. Each of the alloys of varied compositions experienced corrosion rates in a range of 0.28-0.41 $g/(m^2 \cdot h)$. Another study of the $NaCl{-}KCl$ eutectic showed that varying the concentration of *U* added to the system had a direct impact on the rate of corrosion [80]. Similarly, they exposed austenitic stainless steels to either pure $NaCl{-}KCl$, the eutectic with 1 wt% *U*, or the eutectic with 6 % *U* at 750 °C for 30, 100, and even 500 hours in the case of the pure $NaCl{-}KCl$ salt. They determined corrosion rates based on gravimetric comparisons and imaging with SEM and scanning tunneling electron microscopy (STM). The micrographs of the two alloys in each of the three salt compositions after 30 hours are shown in Figure 10. The increased presence of *U* ions intensified the corrosion process, and the corrosion rates reported in Table 5 corroborate this finding as both alloys tested increased by orders of magnitude as a function of *U* ion presence. It was also found that corrosion products preferentially leached following a clear trend: *Cr > Fe > Ni > Mo*, which all increased at greater concentrations of *U* as well. It is important to note that the unit for corrosion rates used in this study (*mm/yr*) differ from what was used in the other *NaCl–KCl* exposure study discussed previously (*g/(m^2·h)*), making it challenging to make direct comparisons between data. Standardized approaches for quantifying and comparing corrosion measurement results could play a role in the development of materials for use in molten salt reactors.

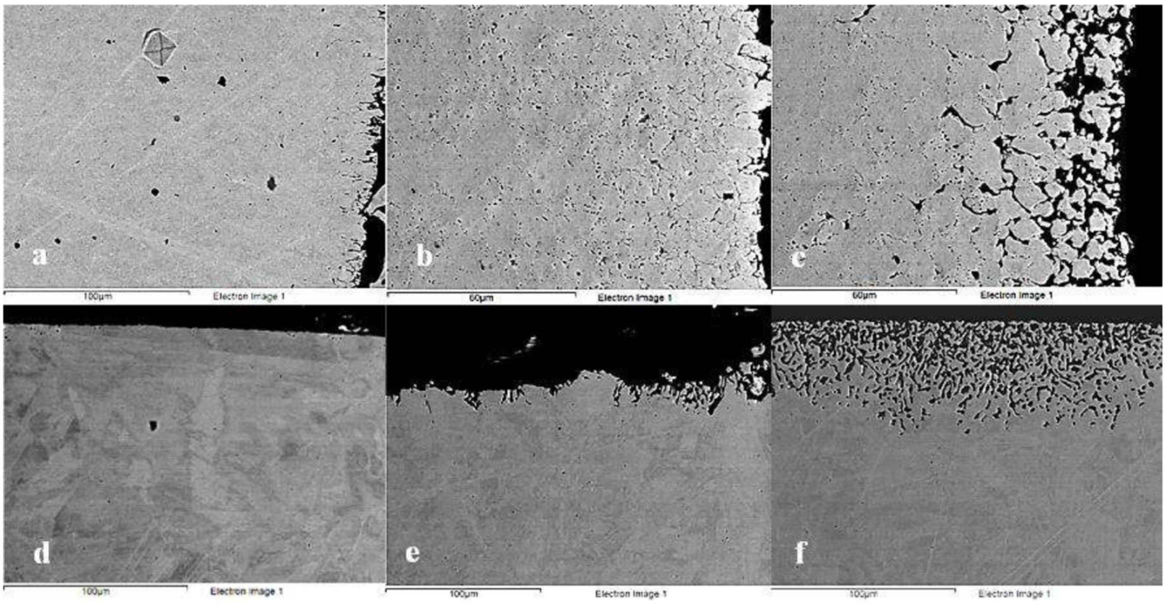

Figure 10: Microstructure of AISI 321 (a–c) and AISI 316L (d–f) surface after 30 h exposure in *NaCl-KCl* (a, d), *NaCl-KCl–UCl$_3$*, 1 wt.% U (b, e), and *NaCl-KCl–UCl$_3$*, 6 wt.% *U* (c, f) melts at 750 °C. [80]

Table 5: Corrosion rate of steels in molten salts after 30–500 h at 750 °C [80].

Time (h)	**Sample**	**NaCl-KCl (mm/yr)**	**NaCl-KCl-UCl$_3$, 1 wt% U (mm/yr)**	**NaCl-KCl-UCl$_3$, 6 wt% U (mm/yr)**
30	AISI 321	0.17 ±0.01	0.38 ±0.04	2.62 ±0.08
	AISI 316L	0.064 ±0.005	0.30 ±0.03	1.8 ±0.07
100	AISI 321	0.039 ±0.006	0.068 ±0.002	0.47 ±0.03
	AISI 316L	0.016 ±0.003	0.038 ±0.003	0.23 ±0.03
500	AISI 321	0.019 ±0.001	—	—
	AISI 316L	0.013 ±0.001	—	—

Another study in the *NaCl–KCl* eutectic investigated the presence and role of *UO$_2$* during the corrosion of SS316 at 750 °C for 100 h [84]. It was found the *UO$_2$* can form in two ways: either at the salt- metal interface or within the salt solution where oxide contaminants react with *UCl$_3$* or *UCl$_4$* species. The authors also note the importance of experimental infrastructure like the crucibles and containment of the salts where oxide ceramics like Al_2O_3 and MgO may be affecting corrosion results as a source of oxygen contamination. An interesting result they discovered was that the presence of *UO$_2$* on the surface of the alloy may play a helpful role by helping to minimize the depletion of *Cr* by limiting its migration as a passivating layer but also noted that this could lead to complications as the uranium continues to fission regardless of chemical composition. It is speculated that any UO_2 that may form would be in small amounts and likely have minimal impacts on overall reactor performance and neutronics.

While the *NaCl–KCl* system is a common molten chloride eutectic that has been well-studied in the literature, it is not currently a leading composition of molten chloride salt being considered for MSR applications. While it provides another set of data incorporating the presence of An-bearing salts, it does not provide quantifiable data that is directly applicable to fuel salts and materials of containment for MSRs. It would be beneficial for predictions to have strategically prioritized research on salt systems that closely reflect the compositions and conditions expected in real-world MSR designs.

A summary of the available data for material compatibility of alloys in *An*-bearing molten chloride salts is provided in Table 6. One of the most prominent limitations of this work is the lack of diversity in base or solvent salts in which U or Pu has been dissolved. Additionally, the singular temperatures and lack of dynamic salt flow hinder the applicability of these corrosion rates for simulations of an operating MSR. However, even from this limited data, it seems that increased concentrations of U, even as U^{3+} rather than the corrosive U^{4+}, may accelerate the corrosion process. Given the anticipated use of UCl_3-based fuel salts, refining the correlation between U and corrosion in relevant salts and materials of containment would enable better predictions for the materials compatibility and corrosion in those expected MSRs.

Table 6: Summary of experimental data available for material compatibility in U and Pu chloride molten salts.

Actinide	Base Salt	Sample	Temperature (°C)	Flow	Time (h)	Corrosion Rate	Reference
1 wt% UCl_3	NaCl-KCl	AISI 321	750	Static	100	0.47 ±0.03 (mm/yr)	80
6 wt% UCl_3	NaCl-KCl	AISI 316L	750			0.23 ±0.03 (mm/yr)	
6 wt% UCl_3	NaCl-KCl	KhN65MVU	750	Static	30	0.39 (g/m²·h)	83
		Hastelloy G-35				0.28 (g/m²·h)	
		Hastelloy C-2000				0.35 (g/m²·h)	
		Hastelloy N				0.38 (g/m²·h)	
		Hastelloy B-3				2.53 (g/m²·h)	
0.1 wt% UCl_x	NaCl-KCl	SS316	750	Static	100	1.79 (mg/cm²)	84
0.2 wt% UCl_x						2.36 (mg/cm²)	
36 mol% $PuCl_3$	NaCl	Inconel 625	557–700	Loop	1000	N/A	82

One of the few studies that used *in situ* electroanalysis to explore corrosion with An-bearing chloride salts involved the investigation of *U* and *Zr* redox buffers in *NaCl–CaCl₂* (50-50 mol%) containing 5 wt% *UCl₃* at 600 °C

[85]. Using a measurement of the open circuit (no potential or current applied), the potential of the system was monitored as the buffers were added to determine how the system adapted over time. Both *U* and *Zr* were found to be effective at buffering the overall redox potential of the salt, but the kinetics and favorability of each requires further investigation. However, these findings highlight the need for expanded experimental validation to confirm their behavior across a broader range of salt compositions and operational conditions.

2.2.1.4. Corrosion Mitigation Strategies

Corrosion mitigation is needed across all MSR designs regardless of salt, but each composition has its own challenges and possible solutions. Some examples of contemporary suggestions for corrosion mitigation are presented here. Unfortunately, the literature rarely includes mitigation in the presence of An-bearing salts. In some cases, species control can be a useful tool to control redox and corrosion in a fuel salt. Delpech et al. have categorized corrosion mitigation into three primary approaches: 1) addition of a soluble-soluble redox system, 2) potentiostatic methods, and 3) use of amphoteric species [30]. Suggestions for soluble-soluble redox systems that could help to buffer the salt solution to mitigate corrosion included $TiCl_2$ and UCl_3, but the kinetics and thermodynamics of these redox buffers require further experimental investigation to refine appropriate methodologies. The specific potentiostat method suggested is the application of a cathodic (reducing) potential. Delpech et. al. performed *in situ* corrosion measurements where Hastelloy C276 (*Ni*57*/Mo*17*/Cr*16*/Fe*5*/W*4*/Mn* in wt%) and AISI 304L (*Fe/Cr*18*/Ni*10) were positioned as WE in *LiCl−KCl* at 500 °C. The study compared the corrosion of these alloys after static exposure or after exposure with an applied potential. It was found that applying a potential significantly decreased the rate of corrosion, potentially mitigating the corrosion almost entirely. Finally, they identified species that could be considered as amphoteric buffers. Amphoteric species (e.g., UCl_3, $TiCl_2$) can act as both oxidants and reductants such that they constrain the potential of the salt solution within the range of its stability domain. However, the behavior of these species requires further investigation as their preliminary results are based on calculations that have not yet been verified.

Other approaches for corrosion mitigation that have been proposed recently in the literature include redox potential control through gas sparging [86] or applying coatings to the structural material like aluminide slurries or spray graphitization [87]. Multiple research teams have considered adding excess metallic species that correspond to the solvent salt, specifically adding *Mg* to $MgCl_2$-based systems [87– 89]. One study found that for a 30.2-69.8 mol% $MgCl_2-KCl$ salt, the corrosion of SS316H steel at 700°C for 100 hours was found to corrode significantly less with an appropriate amount of *Mg* added. They found the concentration of *Cr* on the surface was a function of excess *Mg* added, but at least 0.5 wt% (1.6 mol%) was required to prevent selective dissolution. This relationship is illustrated in Figure 11a. A *Ni*- 200 alloy sample set was also tested, and it was determined that there is a limit for which excess *Mg* can be added before it will begin to form intermetallic species with the *Ni* from the alloy (Figure 11b), which is not ideal for corrosion mitigation. Therefore, these strategies are clearly dependent on the specific combination of fuel salt and structural material compositions. Consistent with other findings presented in this report, additional experimental work would improve understanding of these phenomena and support the development of effective corrosion mitigation strategies. It is also important to note that this study represents another example where the approach to quantifying corrosion did not involve direct corrosion rate measurements—highlighting that comparison of corrosion rates data in the literature is not as simple as tabulating study data directly.

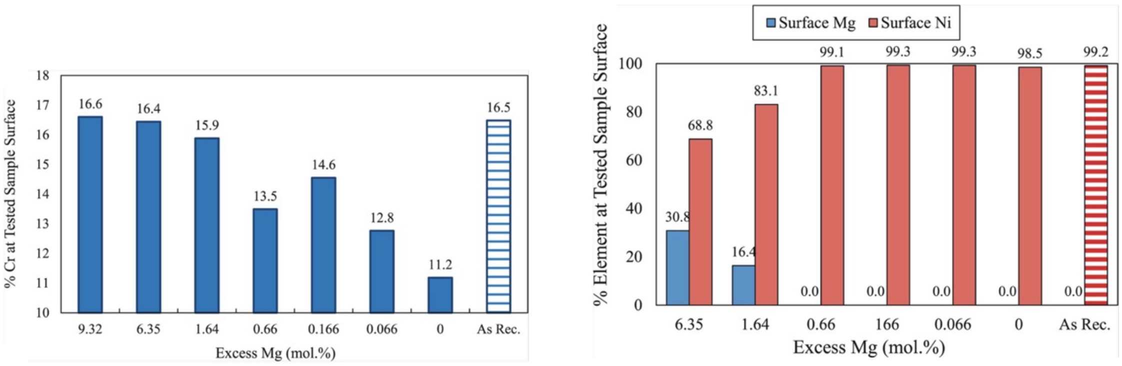

(a)

(b)

Figure 11: (a) Surface *Cr* content measured by XRF for the 316H and (b) *Ni*-200 samples tested in (69.8 mol% *KCl* + 30.2 mol% $MgCl_2$) molten salts with different mol% of excess *Mg* at 700 °C for 100h [88]

2.2.2. Chloride vs. Fluoride Molten Salts

There is a significantly larger body of literature on material corrosion and compatibility in fluoride molten salts, due in large part to the MSRE. However, growing interest in concentrated solar power (CSP), thermal energy storage (TES), and the renewed focus on MSRs has led to an increase in available data on chloride salt–material interactions, allowing for some general conclusions to be drawn regarding their similarities and differences. This report aims to identify key differences between fluoride and chloride molten salt systems, examine the underlying factors contributing to those differences, and explore whether one system can serve as a bounding case for the other (e.g., whether materials compatible with fluoride salts can be expected to perform at least as well in chlorides, or vice versa). These questions were previously examined by Hartmann and Paviet (2022), and their analysis is revisited here alongside relevant literature data on actinide-bearing chloride salts presented in the preceding sections [32].

While there have been some instances where it could be argued that fluorides could help to inform chloride corrosion given the four primary factors that affect corrosion discussed previously (moisture, oxide layers, impurities, and U^{4+}) [32, 42, 90], it is now known that chloride molten salt corrosion is generally more complex than fluoride salt corrosion, and it cannot be definitively stated that fluoride or chloride salts are more corrosive than the other. To illustrate this point, the diffusivity of *Cr* in alloys is well-known, and is the primary corrosion product of interest during fluoride salt exposure in MSRE reports [32, 90–93,190]. However, relative to fluoride salts, larger quantities of other corrosion products (*Mo*, *Fe*, and *Ni*) have been observed following material exposure to chloride molten salts, indicating a difference in fundamental thermodynamics and/or corrosion chemistry. Those species favor their ionic form within the salt, which, although complicating the corrosion process, can be more useful in detecting corrosion early enough to intervene before an impending material failure occurs [32]. Similarly, the comprehensive review of molten salt corrosion studies from 1960 to 2016 compared variables in different systems to determine trends which are summarized in Figure 12 [22]. With respect to halide influence, they observed that chlorides have an overall lower correlation score—a relative value calculated by the authors based on the likelihood of a variable to minimize (positive) or encourage (negative) corrosion—than fluorides, meaning the corrosion rates observed were higher. Lower correlation scores were also determined for impure salts and stagnant solutions compared to purified salts and flowing salt loops, respectively. With respect to An-bearing molten chloride salts, there is much less information available to compare with fluoride fuel salt corrosion.

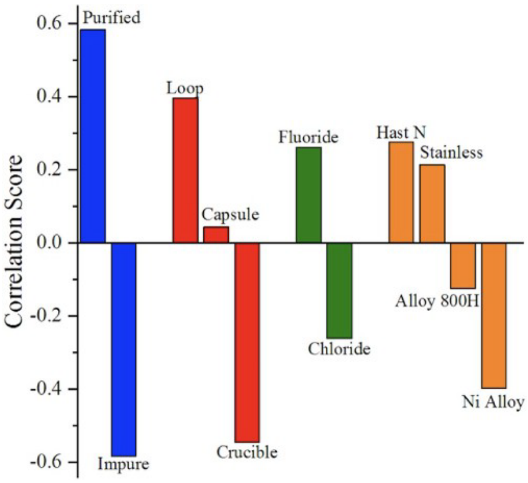

Figure 12: Correlation analysis result for experimental settings. More positive are correlated with lower corrosion rates, while more negative scores are correlated with higher corrosion rates. The variables depicted are, from left to right: salt purity, experiment type, salt type, and sample material

2.3. Summary

There is a great deal of experimental data regarding the corrosion of various alloys in several different molten chloride salt compositions that has been aggregated as new publications in the literature. However, there is a paucity of information specifically observing material compatibility with An-bearing molten chloride salts. Experimental and computational studies that can work in tandem to create an efficient cycle would be beneficial to provide information to a more comprehensive model, and may enable simulating MSR fuels behaviors, to predict, monitor, and mitigate corrosion during operation. Of the limited studies available on UCl_3 and $PuCl_3$ salt exposure, only a small number employ *in situ* electroanalytical techniques to measure corrosion rates within minutes to hours, rather than relying on long-term salt exposure over days, weeks, or months.

Fundamental properties and the behaviors of molten salts dictate the corrosion mechanisms and kinetics that can be expected for corrosion reactions, for diffusion at the salt-metal interface, and for diffusion within the solid alloys of reactor materials. However, there is still an incomplete understanding of salt features, like the electrical double layer that exists at the surface of a material where redox chemistry occurs, and of species like corrosion products and corrosive fuel components (e.g., U^{4+}) that can diffuse toward and away from the surface. Some preliminary modeling has been attempted to describe the EDL region of the salt, but it is still not well understood. Furthermore, the majority of molten salt corrosion studies that have been made public are for specific salt systems with very few components which is not necessarily representative of an MSR that would contain An, Ln, FP, corrosion products, and a range of other contaminants that would certainly influence corrosion. Surrogate burnup systems could be more thoroughly studied through both experimental efforts and advanced modeling and simulation in order to determine how these complex compositional changes affect the thermophysical and thermochemical properties of the salts, and consequently, corrosion behavior.

3. Modeling Approaches for Molten Salt Properties

This section presents state-of-the-art modeling approaches that can be used to predict some key properties of molten salts as a function of their compositions. Namely, in the context of MSR, focus is placed on (i) thermodynamic predictions of the electrochemical driving forces promoting corrosion (i.e. redox potential), (ii) predictions of the salt/metal interface, (iii) predictions of the viscosity and heat capacity of molten salts. We note here that the effects of irradiation on mixing and segregation in the structural material are not discussed here. In practice though, ballistic mixing and thermodynamic ordering are likely to affect the corrosion rate. The literature has not yet quantified these aspects.

With regards to (i) we first recall the principles behind predictions of electro-chemical driving forces for corrosion and further detail the thermodynamic model underpinning predictions of the chemical potentials of all species in the salt (i.e., the modified quasi-chemical model). These chemical potentials fully describe corrosivity of the salts. Second, we perform an independent assessment of the MSTDB-TC database to predict the redox potential for different Cr exposed to a Na-Cl-K-Cl salt. In doing so, we critically detail how to utilize these databases. Overall, we find that the predictions leveraging the MSTDB-TC database are in excellent agreement with experimental data; thereby clearly demonstrating that use of the MSTDB-TC and TP databases provides a promising path to quantitively study the salt states as a function of conditions and their compatibility with metals. Critically, it is worth noting that while the MSTDB-TC is extensive, it does not yet include the effects of impurities in the salt or of fission products (Xe, Kr, lanthanides). Recall here that impurities and fission products in the salt can significantly alter the corrosion kinetics. For example, in [191], it was shown that the fission product europium leads to rapid dissolution of Ni, Fe and Cr in chloride and fluoride salts. Extensions to the databases would thus be necessary to capture and predict the effects of fission products and impurities on molten salt corrosion. Such extensions would then enable being able to predict and anticipate how the dynamic changes in composition of the salt during an MSR reactor operation will impact how corrosive the salt is.

In (ii), emphasis is placed on detailing our state of understanding local salt composition and charged species distributions near the salt-metal interface. Borrowing terminology from the aqueous corrosion community, this is typically referred to as the electric double layer. An understanding of the structure/charge of this double layer is critical. Indeed, the electric double layer governs the electrochemical conditions at the metal–electrolyte interface, directly influencing corrosion kinetics through its control over potential distribution, ion transport, interfacial reactions, and passive film dynamics. The bulk of the work published in the literature focuses on aqueous corrosion which is not representative of the corrosion in molten salts. Indeed, in molten salts, the EDL may have oscillatory charge density due to strong Coulombic interactions and ion correlations which cannot be tracked with current ‘semi-analytical models’. We note that density functional theory and molecular dynamics-based simulations have been used to address this epistemic gap [192]. In [192] for example, the double layer interface between molten 2LiF–BeF2 (FLiBe) and 23LiF–6NaF–21KF (FLiNaK) fluoride mixtures and idealized solid electrode were studied. Overall, the body of work dedicated to studying the structure of the electric double layer remains limited to simplified systems and does not consider the effects of corrosion products, impurities, etc.

Finally, for (iii), we place emphasis on simulation methods to predict the viscosity and heat capacity of molten salts as a function of composition.

3.1. Review of Thermodynamic Predictions of Molten Salt and Structural Metal Interactions

3.1.1. Equilibrium Predictions

In this section we recall, in its simplest form the principle behind the quantification of the driving forces for corrosion. The primary structural materials in current molten salt reactor (MSR) design are metallic, e.g., Hastelloy N and various stainless steels. The corrosion of these alloys has been a technical consideration for the deployment of MSRs. Non-metallic materials, such as graphite components for neutron moderation within the reactor core, are also subject to corrosion by the molten salt, albeit through different chemical mechanisms than metals. Graphite can experience intercalation, for example, where salt ions penetrate its layered structure, leading to mechanical degradation.) [220]. Corrosion of metallic structural materials in molten salts generally involves the anodic dissolution of atoms (e.g., *Ni*, *Fe*, *Cr*, *Co*) and the cathodic reduction of the impurities in the salt (e.g., actinides, fission products, and water contaminants). The oxidation of metal atoms can be expressed as [41]:

$$M \rightarrow M^{n+} + ne^{-} \tag{14}$$

where *M* represents the metal atom and n is the number of transferred electrons. The reduction of the impurities can be written as

$$Ox + ne^{-} \rightarrow Red \tag{15}$$

where Ox and Red represent the oxidized and reduced state of the impurities, respectively. The combination of the two half-cell reactions (14) and (15) yields the overall electrochemical corrosion reaction

$$M + Ox \rightarrow M^{n+} + Red \tag{16}$$

For the corrosion reaction (16) to proceed spontaneously, the Gibbs free energy change (ΔG) must be negative. For an electrochemical process, this change is related to the overall equilibrium potential difference (ΔE) by the equation

$$\Delta G = -nF\Delta E \tag{17}$$

where F is Faraday constant and

$$\Delta E = E_c - E_a \quad . \tag{18}$$

The terms E_a and E_c are the equilibrium potentials of the anodic (14) and cathodic (15) half-reactions, respectively. Corrosion is thermodynamically favorable (spontaneous) when $E_c > E_a$, which corresponds to $\Delta G < 0$. However, as the heterogeneous reaction progresses, the activities of the reacting species (reactants and products) change near the solid-liquid interface. Consequently, the local equilibrium potentials, E_a and E_c, which depend on these activities, also evolve over time. Their relationship to the instantaneous activities of the involved species is described by the Nernst equation:

$$E_a = E_a^0 + \frac{RT}{nF}\ln\frac{a_{M^{n+}}}{a_M} = E_a^{0'} + \frac{RT}{nF}\ln\frac{\frac{[M^{n+}]_\circ}{[M^{n+}]}}{\frac{[M]_\circ}{[M]}} \tag{19}$$

$$E_c = E_c^0 + \frac{RT}{nF}\ln\frac{a_{Ox}}{a_{Red}} = E_c^{0'} + \frac{RT}{nF}\ln\frac{\frac{[Ox]_\circ}{[Ox]}}{\frac{[Red]_\circ}{[Red]}}, \tag{20}$$

where a_i is the activity of species i, $[i]$ is the molar concentration of species i in all equilibrated chemical forms, the terms with ° represent the standard states of the species which the concentrations are referenced to, E_a^0 and E_c^0 are the standard potential for the corresponding half-reactions, $E_a^{0'}$ and $E_c^{0'}$ are formal potential terms that incorporate the activity coefficients, γ_i, with $E_a^{0'} = E_a^0 + \frac{RT}{nF}\ln\frac{\gamma_{M^{n+}}}{\gamma_M}$ and $E_c^{0'} = E_c^0 + \frac{RT}{nF}\ln\frac{\gamma_{Ox}}{\gamma_{Red}}$ [41,77].

To assist material design, it is useful to compare the electrochemical reactivity of potential materials. This is often done by evaluating the potential of the material's half-reaction against a standard reference potential relevant to the environment. In the context of molten salt corrosion, this reference is typically based on the standard reduction potential of the dominant halide couple: F_2/F^- for fluoride salts or Cl_2/Cl^- for chloride salts. Representing the full-cell reaction as $M + \frac{n}{2}X_2 \leftrightarrow MX_n$ where X is Cl or F, according to Equation (17), the standard cell potential $\Delta E^0 = E_c^0 - E_a^0 = -\frac{\Delta G_f^0(MX_n)}{nF}$ where E_c^0 and E_a^0 correspond to $\frac{X_2}{X^-}$ and $\frac{M^{n+}}{M}$ reactions pairs, respectively. Choosing E_c^0 as the reference potential gives the standard half-cell potential and setting our scale to have the standard half-cell potential to be 0 V allows us to set the standard potentials of other species as relative to the standard half-cell potential:

$$E^0_{\frac{\mathrm{M^{n+}}}{M}}\left(\text{vs. }\frac{X_2}{X^-}\right) = \frac{\Delta G_f^0(MX_n)}{nF} \tag{21}$$

where $\Delta G_f^0(MX_n)$ is the standard formation energy of MX_n. The values of $\Delta G_f^0(MX_n)$ as a function of temperature can be found in thermodynamic tables. When the corrosion product MX_n is dissolved in the molten salt, it behaves thermodynamically like a liquid solute - it no longer exists as a solid compound. While liquid solutes have an entropy of mixing, the calculations here do not include an explicit term for entropy of mixing. If the reactor's operating temperature is below the melting point of pure MX_n, the relevant Gibbs free energy of formation for this dissolved (liquid-like) state can be approximated by using that of the supercooled liquid. This value is calculated by summing the standard Gibbs free energy of formation of solid MX_n ($\Delta G_f^0(MX_n)$) and the Gibbs free energy of fusion (melting), both evaluated at the operating temperature. The fusion energy can be calculated by the values of enthalpy, entropy, and heat capacity of the liquid and solid states [94]. Once $E^0_{\frac{M^{n+}}{M}}\left(\text{vs. }\frac{X_2}{X^-}\right)$ is known for a given temperature (it is a constant at a given temperature), the value of $E_{\frac{M^{n+}}{M}}\left(\text{vs. }\frac{X_2}{X^-}\right)$ can be computed at different temperature and activities according to Equation (19) [41]. Figure 13 displays the half-cell reduction potential $E_{\frac{M^{n+}}{M}}\left(\text{vs. }\frac{Cl_2}{Cl^-}\right)$ in Figure 13a and $E_{\frac{M^{n+}}{M}}\left(\text{vs. }\frac{F_2}{F^-}\right)$ in Figure 13b at various temperatures. The solid lines represent the reduction potential of the structural metal M calculated when M equilibrates for M^{n+} with $a_{M^{n+}} = 10^{-6}$; the dotted lines represent the reduction potential of salt constituents. The highest dotted lines in Figures 13a and 13b represent the reduction potential of UCl_4 to UCl_3 and UF_4 to UF_3, respectively. A more negative reduction potential for the M^{n+}/M couple indicates that the metal M is more easily corroded, e.g., Cr metal is less stable ('less noble') than Ni in both chloride and fluoride salts. At the redox potentials below the solid line, the metal is expected to be thermodynamically stable. If an oxidant has a reduction potential higher than the one of an M species, i.e., $E_{\frac{Ox}{Red}} > E_{\frac{M^{n+}}{M}}$, then $\Delta E = E_{\frac{Ox}{Red}} - E_{\frac{M^{n+}}{M}} = -\frac{\Delta G}{nF}$ will be greater than 0, and M can spontaneously corrode until the concentration of dissolved M^{n+} elevates until equilibrium is reached, at which time $E_{\frac{Ox}{Red}} = E_{\frac{M^{n+}}{M}}$ and $E_{\frac{Ox}{Red}} - E_{\frac{M^{n+}}{M}} = 0$ [94]. In Figure 13a, for example, the dissolved actinide UCl_4 can oxidize Fe and any metal with a reduction potential lower than the Fe/$FeCl_3$ pair in chloride salt. Similarly, in Figure 13b, UF_4 can oxidize all metals with a reduction potential lower than the Cr/CrF_3 pair in fluoride salt. Additionally, as shown in Figure 13, the reduction potentials of major salt cations are far below the reduction potential of structural metals, which indicates that the cations of alkaline and alkaline earth elements are not expected to cause considerable corrosion of metals [94] instead, corrosion is typically caused by the dissolved actinides, fission products, moltens salt impurities, structural metal impurities, water contaminants, and oxide impurities.

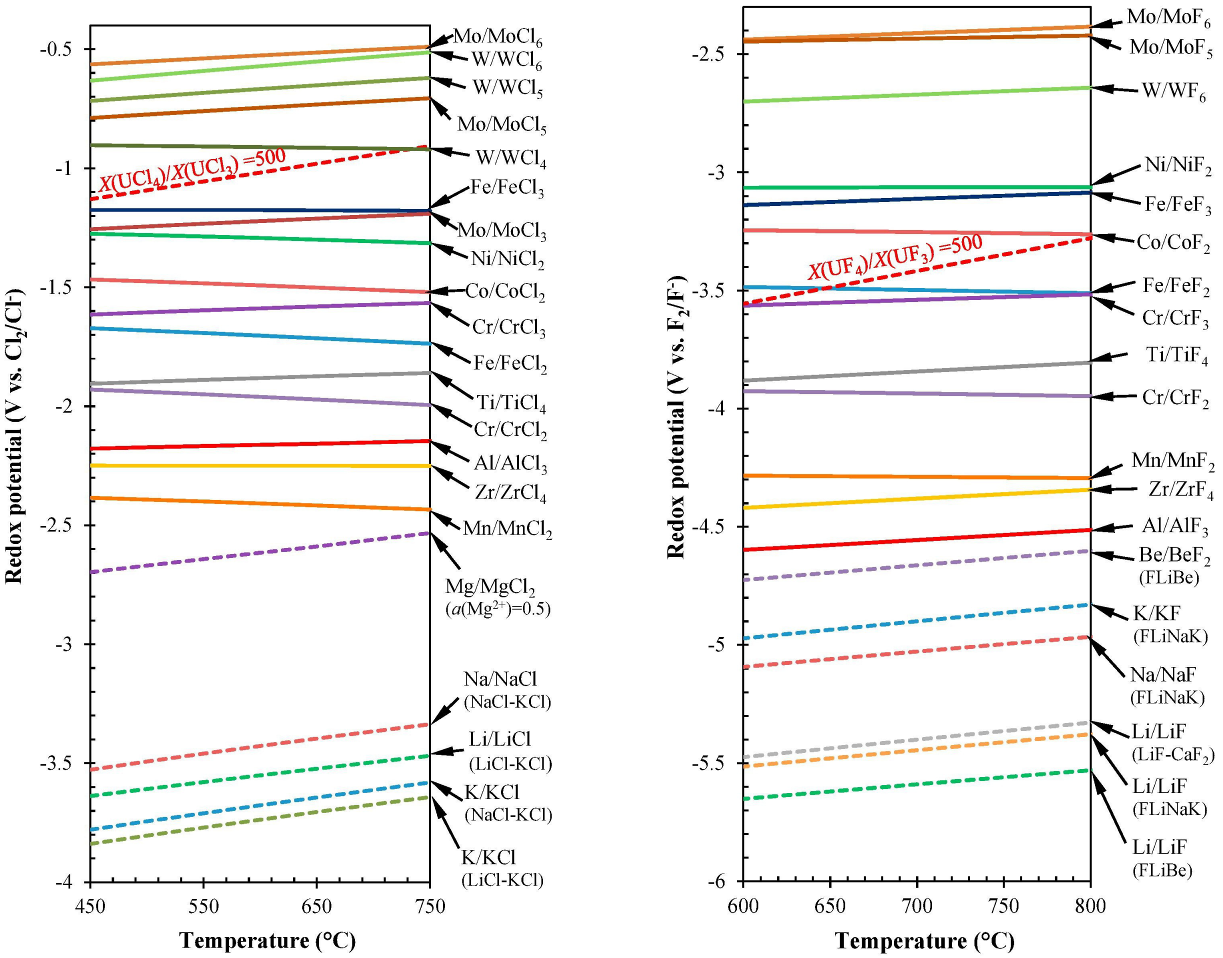

a)

(b)

Figure 13: Redox potential of various redox couples as a function of temperature in (a) chloride salts and (b) fluoride salts. Solid line: metal dissolution at $a_{M^{n+}} = 10^{-6}$; dotted line: reduction of species in the molten salt. The highest dotted lines in Figures 13a and 15b represent the reduction potential of UCl_4 to UCl_3, and UF_4 to UF_3, respectively. [41]

3.1.2. *MSTDB-TC and Modified Quasichemical Model (MQM)*

As shown in the above section, equilibrium redox potential series are helpful for estimating thermodynamic driving forces and identifying stable corrosion products. However, they are often calculated using approximations that neglect the complex, non-ideal interactions within concentrated and multi-component systems. More accurate computations of the Gibbs free energy of the salt as a function of its composition can provide critically important information as to the driving forces for specific reactions to take place. One approach is to use thermodynamic databases that include non-ideality, along with Gibbs free energy minimizers. Specifically, as presented in section II, the MSTDB-TC resource is open to authorized users and researchers, with practical predictive and real-time applications. Coupling the MSTDB-TC with a Gibbs energy minimization software (e.g., Thermochimica [95]) allows for representation of complex multi-cation and multi-anion reciprocal chloride and fluoride salt systems, which arise during reactor operation [61]. MSTDB-TC contains the standard Gibbs free energy of formation for pure substances as a function of temperature, as well as sophisticated models to calculate the activity coefficients of species dissolved in the salt mixture. Below, we briefly discuss what information exists in MSTDB-TC, particularly as pertaining to the effects of fission products and impurities. We then briefly recall the underlying assumptions behind the Modified Quasichemical Model (MQM) which is used to relate the composition of salts to their Gibbs free energy. Appendix A presents a more detailed presentation of the thermodynamic models for molten salt solutions.

The MSTDB-TC database is widely used for predicting thermodynamic behaviors in molten salt reactor environments, including corrosion and redox potentials. The latest MSTDB-TC (version 4.0) contains thermodynamic values for fluoride, chloride, and some iodide components and related systems of interest for molten salt reactor technology. Table 4 summarizes the evaluated endmembers and the number of pseudo-binary, pseudo-ternary, and higher-order systems.

Despite its utility, the database does not contain information for all properties of all elements, particularly regarding the prediction of effects introduced by impurities and fission products. This unavailability of data limits the accuracy of corrosion and redox modeling for reactor design, safety assessments, and material selection. One major limitation is the incomplete coverage of fission products and impurities. Although MSTDB-TC addresses many actinides and major salt constituents, it lacks robust thermodynamic assessments for a wide range of critical fission products, particularly lanthanides like promethium (Pm), europium (Eu), gadolinium (Gd), and samarium (Sm). Furthermore, noble metal fission products such as technetium (Tc), ruthenium (Ru), rhodium (Rh), and palladium (Pd) have only minimal modeling, particularly concerning their solubility and redox behaviors in chloride salt systems. Additionally, the database currently provides limited insights into the influence of volatile fission products such as cesium (Cs) and iodine (I). While some preliminary data exist, comprehensive and accurate predictive coverage for their chemical interactions and redox behavior remains insufficient. A significant lack of data availability also exists concerning the handling of minor impurities, notably oxygen (O), hydroxides (OH), hydrogen (H, H_2), and tellurium (Te). These species, although present in trace quantities, significantly affect corrosion and redox potentials but are poorly represented in MSTDB-TC. Moreover, noble gases like helium (He), neon (Ne), argon (Ar), krypton (Kr), and xenon (Xe) have Gibbs energy models included, but crucially, their solubilities in molten salts remain unaddressed.

Table 7: Summary of Missing or Underrepresented Elements in MSTDB-TC[193-196]

Category	Elements With No (or Partial) Data Availability
Lanthanide fission products	Promethium (Pm), europium (Eu), Gadolinium (Gd), Samarium (Sm)
Volatile fission products	Cesium (Cs), Iodine (I)
Noble metal fission products	Technetium (Tc), Ruthenium (Ru), Rhodium (Rh), Palladium (Pd)
Impurities	Oxygen (O), Hydroxide (OH), Hydrogen (H, H_2, HI), Tellurium (Te)
Noble gases	Helium (He), Neon (Ne), Argon (Ar), Krypton (Kr), Xenon (Xe)

Looking at the example of a redox potential for a chemical reaction, we recall the thermodynamic quantities that can be extracted from the use of MSTDB-TC and of Thermochimica. If reaction (12) is a heterogeneous reaction occurring at the salt/metal, its electrochemical driving force in the general form can be written as

$$\Delta\mu^{rxn} = \Delta\mu^{o,rxn} + \left(\frac{c_{M^{n+}}\gamma_{M^{n+}}c_{Red}\gamma_{Red}}{a_M c_{Ox}\gamma_{Ox}} * \frac{(c_{M^{n+}}{}^{\circ})^{-1}(c_{Red}{}^{\circ})^{-1}}{1 * (c_{Ox}{}^{\circ})^{-1}}\right) - nF\Delta\phi \tag{22}$$

Where $a_M = 1$ for pure metal, $\Delta\mu^{o,rxn}$ is the standard chemical potential difference of the reaction, and $\Delta\phi$ is the externally applied electric potential on the metal electrode during an experiment. In a reactor environment, $\Delta\phi$ = 0.

To fully grasp the strength of thermodynamic modeling of molten salts, it is critical to recall some fundamentals. Thermodynamic modeling of molten salt systems typically utilizes the Calculation of Phase Diagrams (CALPHAD) framework [96, 97]. The CALPHAD framework describes each phase in a system using a Gibbs energy model that is a function of temperature, pressure, and concentration. For solution phases, these models typically include an excess Gibbs energy term to account for non-ideal component interactions. Specifically, the Gibbs energy function of a solution can be expressed generally [98] as:

$$G = G^0 + G^{id} + G^{XS} \tag{23}$$

where G^0 is the proportional sum of the standard Gibbs energy of the pure endmembers, G^{id} is the ideal mixing term derived from the entropic effects of random mixing, and G^{XS} is the excess mixing (enthalpy) term representing non-ideality or the energy of attractive or repulsive forces among the components in the solution. Endmember in the molten salt context refers to the individual base salts of the pseudo- binary (i.e., systems of two-component salts that share a common anion, such as NaCl–KCl) and/or pseudo-ternary systems (such as NaCl–KCl–UCl_3) [61]. The values for *G* are generally obtained via optimizations (i.e., fit to selected models) based on the available phase and thermochemical data. Salt melt solutions are typically represented by the MQM developed primarily by Pelton, Blander, and Chartrand in a series of seminal papers [99–102], based on Fowler and Guggenheim's quasichemical theory [103]. The MQM captures the short-range ordering (SRO) present in molten salts, a crucial feature that ideal or regular solution models fail to represent. MQM solutions come in different forms from simple to complex. The Modified Quasichemical Model in the Quadruplet Approximation (MQMQA) is an extension of the two-sublattice model in the pair approximation; it is the commonly implemented version for molten salts and slags in CALPHAD databases like MSTDB-TC. MQMQA can treat simultaneously the FNN (First Nearest Neighbors) and SNN (Second Nearest Neighbor) SRO (Short-Range Order) in solutions using two sublattices. When one sublattice is occupied by only one species, or is empty, the model reduces to the MQM for one sublattice in the pair approximation. The coordination numbers and the ratio of the number of sites on the two sublattices are permitted to vary with composition, thereby making the model ideally suited to the treatment of liquid solutions such as molten salts. A significant computational simplification is achieved by formally treating the quadruplets as the "components" of the solution [102].

Thermodynamic system assessments rely on experimental and/or computationally derived data to parameterize selected thermodynamic models. For molten salt reactor-relevant systems, fundamental pure compound data such as standard enthalpies of formation, standard entropies, and heat capacities are often available for simpler phases. Experimentally obtained phase equilibria, including pseudo-binary and pseudo-ternary phase diagrams with reported melting points, phase transitions, and solubility limits, constitute a major source of input for thermodynamic modeling. Valuable complementary experimental data include measured enthalpies of mixing, as well as data from electrochemical and vapor pressure measurements. *In situ* Extended X-ray Absorption Fine Structure (EXAFS) measurements can further provide insight into species coordination in solution, informing the selection of coordination numbers and endmembers. Uncertainties in experimental data are incorporated into the convergence criteria of thermodynamic optimization software (e.g., the FactSage OptiSage module [104]); where not reported, uncertainties are assumed based on accepted ranges for similar measurements. Computationally derived values also contribute to developing Gibbs energy relations, including predictions of intermediate compound stability from electronic structure density functional theory (DFT) calculations [105, 106] and insights into coordination number distributions from MD simulations [107, 108] [61].

The general process of data validation includes using the assessed or extrapolated set of Gibbs functions and models to reproduce available phase equilibria and other thermodynamic observations. Crucially, predictions for the pseudo-ternary system derived solely from combining binary assessments require experimental validation. This is essential because the optimization process using only binary data can sometimes yield different sets of model parameters that describe the binary systems almost equally well. While these distinct parameter sets might accurately reproduce the binary phase diagrams, they can lead to different predictions for phase stability and properties when extrapolated to the ternary system. Therefore, experimental confirmation, particularly of key features like eutectic or peritectic points, is important to ensure the extrapolated ternary model is reliable [61].

3.1.3. Practical Use of the Databases - Energy References and Half-cell Potential Connection

Given the complexity of thermodynamic models for molten salt solutions, in what follows we demonstrate how they can be used to predict the redox potential associated with the corrosion of a pure metal. Further, this example also serves the purpose of performing an independent assessment of the accuracy of these databases. Apart from the Gibbs energy of molten salt, to assess the electrochemical reaction driving force defined in Equation (22), we also need the Gibbs energy of other participants in the reaction, such as pure metals and solid solutions. It is crucial to ensure that the thermodynamic models and databases for different material systems are compatible. Databases storing thermodynamic values relative to the same reference states are self-consistent and such databases can be combined for the calculation of chemical equilibria. The standard Gibbs free energies of compounds, such as the values listed in the Scientific Group Thermodata Europe (SGTE) [109] database, use the 'Standard Element Reference' (SER), such that enthalpies are defined relative to those of the pure elements in their defined reference phase at 298.15 K. The entropy of an element in a phase has an absolute value, but the enthalpy (and therefore the Gibbs energy) has no absolute value, and the values used in calculations for enthalpies and Gibbs free energies are thus defined relative to reference states. The most common reference state for the enthalpy is that of the element in its reference phase at 298.15 K. This reference phase is normally the stable phase at 105 Pa and 298.15 K. Thus, the Gibbs formation energy of a pure component can be calculated from

$$G(T) = \Delta_f H^0_{(298)} - S^0_{(298)} T + \int_{298}^{T} C_P\,(T) dT - T \int_{298}^{T} \left(\frac{C_p(T)}{T}\right) dT, \tag{24}$$

where $\Delta_f H^0_{(298)}$ is the standard enthalpy of formation from the element at SER and $S^0_{(298)}$ is the standard absolute entropy. $C_P(T)$ is the heat capacity at constant pressure. Among all the MQMs, the standard Gibbs energy of pure endmembers (g^0_m, $g^0_{\frac{A}{X}}$, $g^0_{\frac{AB}{XY}}$) are calculated from the SER states of their constituent elements, where the terms with ° represent the standard states of the species which the concentrations are referenced to. For example, at a given temperature, the standard Gibbs energy of CrCl₂ (pure liquid, T) is defined based on the following reaction:

$$Cr(SER,T) + Cl_2(SER,T) \rightarrow CrCl_2(pureliquid,T), \tag{25}$$

where Cr (SER, T) is pure solid Cr (BCC), and Cl_2 (SER, T) is pure gaseous Cl_2, at temperature T. The standard Gibbs energy of $CrCl_2$(pure liquid, T) compound is defined using its constituent elements, with their standard states Gibbs energies and chemical potentials obtained for the phases as based on SER:

$$\boldsymbol{G^0_{CrCl_2,liq,T} = \mu^0_{CrCl_2,liq,T} = \Delta_r G^0 + \mu^0_{Cr,SER,T} + \mu^0_{Cl_2,SER,T}} \tag{26}$$

where $\Delta_r G^0$ is the standard Gibbs free energy change of the chemical reaction. In this case, $\Delta_r G^0$ is the formation energy, $\Delta_f G^0$, of $CrCl_2$ (pure liquid, T), and $\Delta_f G_{Cr,SER,T} = \Delta_f G_{Cl,SER,T} = 0$ at SER by definition. Therefore, MSTDB-TC is in principle compatible with the pure element database, and the solid solution energy data calculated from the single sublattice polynomial or compound energy formulism [61].

During reactor corrosion, the corrosion product $CrCl_2$ does not exist in a pure liquid state, but rather dissolves in the base salt, such as NaCl. To connect MSTDB-TC to the cell potential (e.g., $E_{\frac{Cr^{2+}}{Cr}}\left(vs.\frac{Cl_2}{Cl^-}\right)$) frequently encountered in electrochemical experiments such as cyclic voltammetry, consider the following reaction occurring in the base salt:

$$Cr(s,T) + Cl_2(g,T) \rightarrow CrCl_2(dissolved,T). \tag{27}$$

The Gibbs energy change of reaction (22) is

$$\Delta G = \mu_{CrCl_2,dissolved,T} - \mu_{Cr,s,T} - \mu_{Cl_2,g,T}$$
$$= \mu^0_{CrCl_2,liq,T} + RT\ln a_{CrCl_2} - \mu^0_{Cr,s,T} - \left(\mu^0_{Cl_2,g,T} + RT\ln\frac{P_{Cl_2}}{P^0}\right)$$
$$= -nFE_{\frac{Cr^{2+}}{Cr}}\left(vs.\frac{Cl_2}{Cl^-}\right),$$

(28), (29), (30)

where $\mu^0_{Cr,s,T}$ and $\mu^0_{Cl_2,g,T}$ are derived from the standard Gibbs free energy of the pure elements, P^0 is the pressure of the standard state for the gas phase, and we assume unity for the pure metal activity. By comparing $E_{\frac{Cr^{2+}}{Cr}}\left(vs.\frac{Cl_2}{Cl^-}\right)$ calculated using MSTDB-TC with the documented equilibrium potential (open-circuit potential) derived from standard thermodynamic compilations or experiments, the database values can be validated. Note that in practice reaction (27) is the result of two reactions. The first reaction corresponds to the formation of $CrCl_2$ while the second reaction corresponds to the dissolution of $CrCl_2$. As such, the energy of dissolution is being approximated as the energy of melting, which implicitly assumes that there is no dissociation. For a salt which dissociates partly or completely during the dissolution there will be deviation from this approximation due to an energy of solvation.

The aforementioned calculations are repeated for three systems (Ni, Cr and Fe). Figure 14 compares equilibrium potentials for the M^{2+}/M relative to the standard Cl_2/Cl^- reference. Potentials calculated in this work using MSTDB-TC via Thermochimica [95] (solid lines with markers: Ni/$NiCl_2$(green), Fe/$FeCl_2$(blue), Cr/$CrCl_2$(purple)) are overlaid with corresponding values derived from standard thermodynamic compilations as reported by Guo et al. [41] and summarized in Section 3.1.1. The MSTDB-TC derived potentials were calculated using Equation (30), where standard chemical potential for the pure elements and the pure liquid $CrCl_2$ (potentially supercooled, as the standard state for the dissolved component) were obtained from MSTDB-TC, and $a_{Cl_2} = 1$. To evaluate the potential under the specific conditions reported in Ref. [41], where the standard state for M^{n+} was set at a concentration of 1 M, and the relevant ionic activity was specified as $a_{M^{n+}} = 10^{-6}$, this numerical value was used for the component activity a_{CrCl_2} in Equation (29). This operational step is employed because when interfacing component-based thermodynamic models with electrochemical formalisms (MQMQA [102]), it ensures the potential is evaluated at the specified activity level relative to the component-derived standard potential and the common anion (Cl_2/Cl^-) reference.

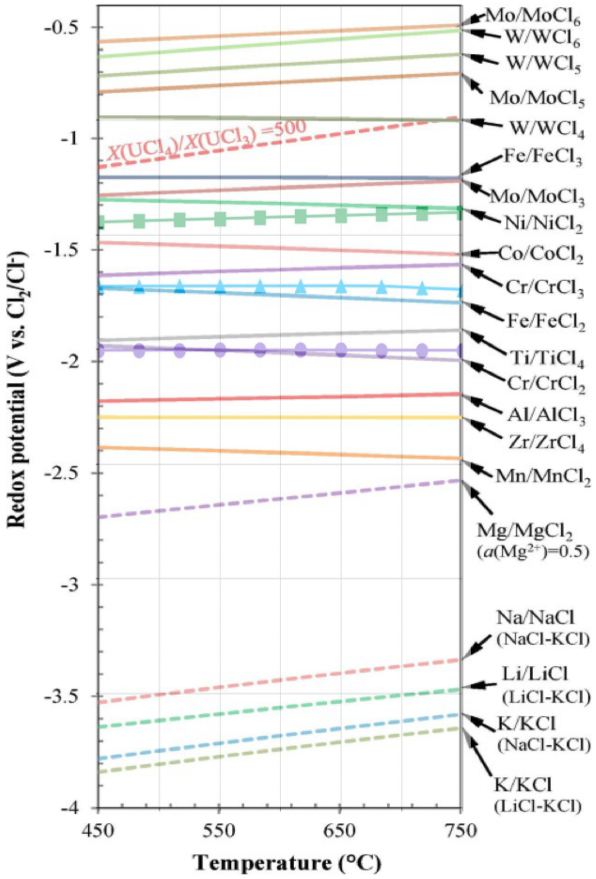

Figure 14: Comparison of redox potentials derived from MSTDB-TC (solid lines and dashed lines) and values calculated from standard thermodynamic compilations using Thermochimica (represented by solid lines with markers, from Ref. [41]). Marker colors have been set to match the thermodynamic database colors: Ni/NiCl$_2$ (green), Fe/FeCl$_2$ (blue), and Cr/CrCl$_2$ (purple).

As shown in Figure 14, the redox potentials derived from MSTDB-TC exhibit good agreement with those reported by Guo et al. [41] for all three metal systems (Ni, Fe, Cr). This consistency suggests that MSTDB-TC provides a reliable thermodynamic basis for estimating these redox potentials, yielding results comparable to those derived from other established thermodynamic data sources when standard electrochemical principles are applied; additionally, it is confirmed that the reference state used for molten salt and pure element species are compatible. The minor discrepancies observed are likely attributable to variations in the underlying thermodynamic functions - particularly the heat capacity ($Cp(T)$) data and models used for pure elements (M(s), Cl_2(g), and especially the liquid/supercooled MCl_2 state - between MSTDB-TC and the sources and fusion models utilized in Ref. [41].

To further validate the MSTDB-TC database, we examined the Cr/Cr^{2+} couple in FLiNaK salt at 600 C, comparing computational results with experimental data in Figure 15. Experimental measurements by Chan et al. (Chan et al. 2022) (Fig.15a) report the half-cell potential $E_{\frac{Cr^{2+}}{Cr}}\left(vs.\frac{F_2}{F^-}\right)$ at various Cr^{2+} molarities. In that work, Cr^{2+} was generated *in situ* from CrF_3 addition and was presumed to form Cr(s) and CrF_2 via the disproportionation reaction: $3CrF_2 \leftrightarrow 2CrF_3 + Cr$. Extrapolation of a linear fit to the experimental at low concentrations, to unit molarity

($\log(C_{Cr^{2+}}) = 0$), yields a half-cell standard electrode potential $E^{0}_{\frac{Cr^{2+}}{Cr}}$ of -3.41 $\left(vs.\frac{F_2}{F^-}\right)$. For comparison, we calculated potentials using MSTDB-TC with Thermochimica (Fig.15(b)). The potential is defined for the reaction Cr(s) + F$_2$(g) ↔ CrF$_2$ (in FLiNaK salt) as:

$$E^{0}_{\frac{Cr^{2+}}{Cr}} = -\frac{1}{nF}\left(\mu^{0}_{CrF_2} - \mu^{0}_{Cr} - \mu^{0}_{F_2}\right) \quad . \tag{31}$$

Standard chemical potentials μ^{0}_{Cr} and $\mu^{0}_{F_2}$ were independently computed, while mole fractions (X_{CrF_2}) ranging from 10^{-8} to 1 were converted to molarity (C_{CrF_2}) using an estimated FLiNaK density of 2.060 g/cm^3 [111] and using the FLiNaK average molar mass, assuming dilute CrF$_2$. A linear fit to the calculated $E_{\frac{Cr^{2+}}{Cr}}$ values at the three lowest concentrations (approximating the infinite dilution Henrian regime) extrapolated to a formal potential $E^{0',H}$ of -3.62 V vs. F$_2$/F$^-$ at unit molarity, showed reasonable agreement with the experimental -3.41 V. The observed Nernstian slope from this fit (0.0737) deviates from the theoretical value, $\frac{2.303RT}{nF} \approx 0.0866$, suggesting that even these low concentrations may not fully represent ideal dilute behavior. This deviation, alongside potential database inaccuracies or computational minimization nuances, likely contributes to the discrepancy between the modeled and experimental formal potentials.

While the calculated potential $E_{\frac{Cr^{2+}}{Cr}}\left(vs.\frac{F_2}{F^-}\right)$ is independent of the chosen standard state for CrF$_2$, the interpretation of activity and standard potentials ($E^{0'}$) varies. To explore this, we analyze $E_{\frac{Cr^{2+}}{Cr}}$ as a function of CrF$_2$ mole fraction, as depicted in Figure 15c. Both the Henrian (infinite dilution reference, mole fraction scale) and Raoultian (pure component reference) standard states for CrF$_2$ are notionally defined at unit mole fraction, indicated by a vertical dotted line. The Henrian standard state describes a hypothetical pure CrF$_2$ that retains the properties of an infinitely dilute solute in FLiNaK [112]. The Henrian formal potential, $E^{0',H}$, is obtained by extrapolating a linear fit of $E_{\frac{Cr^{2+}}{Cr}}$ vs. $\log_{10}(\mathrm{X_{CrF_2}})$ from the dilute region to $X_{CrF_2} = 1$. In contrast, the Raoultian standard potential, $E^{\circ,R}$, for the same overall reaction is directly calculated using the standard chemical potential of pure CrF$_2$ (solid) via the Nernst equation:

$$E^{\circ,R} = -\frac{1}{nF}\left(\mu^{\circ}{}_{CrF_2} - \mu^{\circ}{}_{Cr} - \mu^{\circ}{}_{F_2}\right) \tag{32}$$

Understanding the activity coefficient (γ_{CrF_2}) of CrF$_2$ in FLiNaK is essential for accurate corrosion modeling, as it quantifies deviations from ideal solution behavior. On a mole fraction scale, $\log_{10}(\gamma_{CrF_2})$ is calculated from the chemical potential of CrF$_2$ in solution (μ_{CrF_2}) and its standard state chemical potential ($\mu^{\circ}{}_{CrF_2}$) using:

$$\log_{10}(\gamma_{CrF_2}) = \frac{1}{2.303RT}(\mu_{CrF_2} - \mu^0_{CrF_2}) - \log_{10}(X_{CrF_2})$$

(33)

The difference between using Raoultian and Henrian reference lies in the choice of $\mu^0_{CrF_2}$. For the Raoultian reference, $\mu^0_{CrF_2}$ is $\mu^{0,R}_{CrF_2}$, derived from the chemical potential of pure solid CrF₂. For the Henrian reference, $\mu^0_{CrF_2}$ is $\mu^{0,H}_{CrF_2}$, derived from the formal potential $E^{0',H}$ (obtained from the $\mathrm{E}_{\frac{\mathrm{Cr}^{2+}}{Cr}}$ vs. $\log_{10}(\mathrm{X}_{\mathrm{CrF}_2})$ fit in Figure15(c) as $\mu^{0,H}_{CrF_2} = nFE^{0,H} + \mu^0_{Cr} + \mu^0_{F_2}$. Substituting these respective standard chemical potentials into Equation (33) yields the Raoultian ($\gamma^R_{CrF_2}$) and Henrian ($\gamma^H_{CrF_2}$) activity coefficients across the concentration range.

The limiting behaviors of these activity coefficients are distinct. By definition, activity is unity at the standard state. For the Raoultian reference, the standard state is pure CrF₂ ($X_{CrF_2} = 1$), thus $\gamma^R_{CrF_2} \rightarrow 1$ as $X_{CrF_2} \rightarrow 1$. For the Henrian reference, the standard state is a hypothetical $X_{CrF_2} = 1$ exhibiting ideal dilute behavior, where $\gamma^H_{CrF_2}$ is also defined as 1. However, the practical consequence is that $\gamma^H_{CrF_2} \rightarrow 1$ as $X_{CrF_2} \rightarrow 0$ (actual infinite dilution) [112]. Figure 15d illustrates these trends. The calculated $\log_{10}\gamma^R_{CrF_2}$ (red curve) correctly approaches 0 as $\log_{10}X_{CrF_2}$ approaches 0. However, $\log_{10}\gamma^H_{CrF_2}$ derived from the linear fit of $\mathrm{E}_{\frac{\mathrm{Cr}^{2+}}{Cr}}$ (black curve, labeled 'Henrian, from fit') does not approach 0 at very low X_{CrF_2}. This discrepancy arises because the fitted slope of $\mathrm{E}_{\frac{\mathrm{Cr}^{2+}}{Cr}}$ vs. $\log_{10}X_{CrF_2}$ deviates from the ideal Nernstian value, indicating that the fitted dilute region was not yet fully governed by Henry's Law. To illustrate ideal Henrian behavior, an alternative $\gamma^H_{CrF_2}$ (green curve, 'Henrian, ideal Nernst') was calculated by defining $\mu^{0,H}_{CrF_2}$ such that $\gamma^H_{CrF_2} = 1$ at the most dilute computed X_{CrF_2} point, i.e., $\mu^{0,H,ideal}_{CrF_2} = \mu^{0,\min(X_{CrF_2})}_{CrF_2} - RT\ln(1 * \min(X_{CrF_2}))$. This green curve correctly shows $\log_{10}\gamma^H_{CrF_2}$ approaching 0 at low concentrations.

The Raoultian activity coefficient, $\gamma^R_{CrF_2}$, approaches unity as $X_{CrF_2} \rightarrow 1$, as expected. Interestingly, $\gamma^R_{CrF_2}$ is close to unity at very high dilutions, suggesting the Raoultian activity coefficient at infinite dilution $\gamma^{R,\infty}_{CrF_2} \approx 1$. Both $\log_{10}\gamma^R_{CrF_2}$ and $\log_{10}\gamma^{H,ideal}_{CrF_2}$ display similar trends of deviation from ideality across the intermediate mole fractions, remaining relatively close to each other due to the aforementioned proximity $\gamma^{R,\infty}_{CrF_2}$ to 1. These fluctuations underscore the non-ideal nature of CrF₂ dissolution in FLiNaK. Comparing the Henrian and Raoultian references, the Henrian convention is advantageous as it simplifies activity to mole fraction ($a_i \approx X_i$) in sufficiently dilute solutions, a common regime for corrosion studies [112].

Overall, as shown in Figures 14 and 15 (see the comparison between *(a)* and *(b)*), predictions using the MSTDB-TC databases and Thermochimica are in excellent agreement with observations. As will be discussed in Section 4 and as demonstrated in Figure 15 (d), the activities of Cr^{2+} ions in FLiNak can be recorded/quantified, such that these tools can further be utilized as the basis for continuum scale corrosion models. Naturally, extensions of the MSTDB-TC database to include the effects of fission products and impurities will be necessary to deploy these models in realistic and prototypical service conditions. Finally, we note that the use of MSTDB-TC and Thermochimica remains complex and significant care must be taken to ensure that the data extracted from these tools are used correctly. These complexities are detailed in Appendix B.

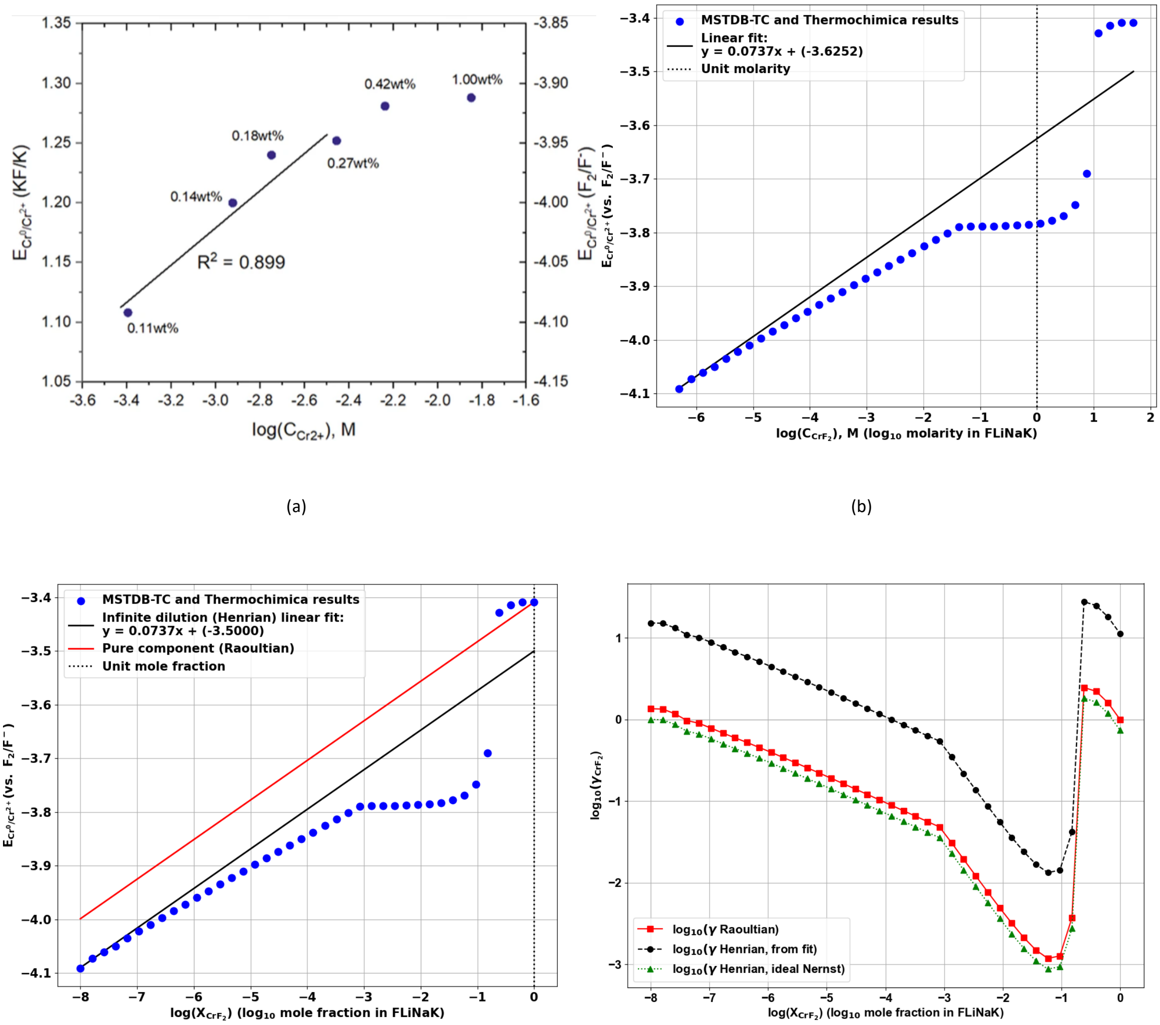

(a)

(b)

(c)

(d)

Figure 15: Thermodynamic properties of the Cr/Cr^{2+} couple in FLiNaK salt at 600°C, determined by experimental measurement and computational modeling using MSTDB-TC with Thermochimica. (a) Experimentally measured half- cell potential, ECr^{2+}/Cr ($vs. F_2/F^-$), plotted against the logarithm of Cr^{2+} molarity (mol/L) in FLiNaK. Data is taken from Ref. [110]. Note: The Y-axis for this panel is located on the right. (b) Computationally derived half-cell potential, ECr^{2+}/Cr ($vs. F_2/F^-$), plotted against the logarithm of Cr^{2+} molarity, calculated using MSTDB-TC and Thermochimica. These calculations mimic the experimental conditions shown in (a). (c) Calculated half-cell potential, ECr^{2+}/Cr ($vs. F_2/F^-$), plotted against the logarithm of the CrF_2 mole fraction in FLiNaK. The plot compares the Henrian linear fit (derived from the dilute region) with the potential calculated using the Raoultian standard state (pure CrF_2). (d) Logarithm of the calculated activity coefficient ($\log_{10}\gamma$) of CrF_2 in FLiNaK as a function of the logarithm of its mole fraction. Curves represent γ calculated using: (i) the Raoultian (pure component) standard reference, (ii) the Henrian standard reference derived from the linear fit of ECr^{2+}/Cr ($vs. F_2/F^-$) in the dilute region shown in (c), and (iii) a Henrian standard reference assuming ideal Nernstian behavior ($\gamma_H = 1$) at the most dilute calculated point.

3.2 Electric double layer - from aqueous solution to molten salts

The rate of reaction/corrosion in molten salts is expected to be altered/conditioned by the charge distribution in the vicinity of the salt/metal interface. Among other factors, the electric double layer controls the surface potential, which influences ion adsorption/desorption and electron transfer rates. It further modulates the local ionic concentration and thus the transport of reactants/products to and from the corrosion site, thus significantly impacting the activation energy barrier for electron transfer. The EDL not only contributes a capacitive current but also dictates the local reactant concentrations and potential drop that drive the faradaic reactions (e.g., the Frumkin correction [77]). Understanding the EDL structure is therefore crucial to being able to predict reaction rates at salt/metal interfaces. As will be shown in this section, to date, the community cannot yet comprehensively and rigorously predict the structure of this EDL nor its linkage to the materials composition. Further, under irradiation, the EDL is likely to be disturbed. Unfortunately, the net effects of irradiation on the EDL structure are not clearly understood. These epistemic gaps are of strong predictive consequence. Indeed, as will be discussed in Section 4, to date, all corrosion models must postulate reaction rates at the interface or use experimental data to fit the model against, and this severely hinders the predictiveness of corrosion models. Indeed, typical corrosion models employ the Butler-Volmer equation (with or without the Frumkin correction) to indirectly capture the effects of the EDL on the current density and overpotential. However, given that these parameters are inferred from experiments, blind predictions of the corrosion rate cannot be performed. In what follows we provide a state-of-the-art focused on modeling the EDL via both analytical and numerical methods. We first assess the quality and appropriateness of mean-field models, which approximate the local electrostatic field at any position in the fluid as being a local average that varies smoothly across geometric space, rather than as dynamically changing as the nearby surrounding atomic configurations change. We find that while mean-field approaches are well suited for studying aqueous corrosion, the deviations of the mean-field models from the real behavior of an EDL results in an inability to make quantitative predictions as current mean-field models do not capture how the electrostatic potential oscillates as a function of distance from the surface due to the EDL.

Mean-field models: The vast majority of the body of knowledge regarding EDLs is derived from the study of aqueous systems. In aqueous electrochemistry, the classical mean-field description is the Gouy-Chapman-Stern (GCS) model [77]. This model conceptualizes the EDL as consisting of a compact Stern layer (accounting for finite ion size and specific adsorption of immobile ions near the electrode) and an outer diffuse layer (mobile ions distributed according to electrostatic forces and thermal motion), depicted in Figure 16(a). These layers can be conceptualized as two capacitors in series. The diffuse layer is typically described by the Poisson-Boltzmann (PB) equation, which relates the electrostatic potential (ϕ) to the local charge density arising from point-like ions in a uniform dielectric continuum:

$$\frac{d^2\phi}{dx^2} = -\frac{e}{\epsilon\epsilon_0}\sum_j n_j^0 \, z_j \exp\left(\frac{-z_j e\phi}{k_B T}\right) \tag{33}$$

where ϵ is the dielectric constant of the medium, ϵ_0 is the vacuum electric permittivity, n_j^0 and z_j are the bulk number concentration and valence of ion j, respectively. ϕ is measured with respect to the bulk solution. Grahame [134] further refined the Stern layer by distinguishing between an inner Helmholtz plane (IHP) for specifically adsorbed, often desolated ions, and an outer Helmholtz plane (OHP) for the closest solvated ions, thereby providing a more detailed picture of ion adsorption and solvent effects at aqueous interfaces [135]. The graphic illustration of the Grahame model is shown in Figure 16(b). However, the foundational assumptions of the GCS and Grahame models—namely, ions as point charges, a dilute solution, and a continuous, uniform dielectric medium—render them fundamentally inadequate for describing the EDL in highly concentrated electrolytes like molten salts. In such systems, the finite size of ions and the discrete nature of the solvent become dominant. The excluded volume of ions significantly impacts their packing and distribution near the electrode, leading to phenomena not captured by classical theories.

To address these limitations, particularly for steric effects (i.e., the influence of the physical size, shape, orientation, or spatial arrangement of atoms/molecules), modifications to the PB equation as well as alternative modeling approaches have been developed. Liquid-state theories and simulation methods, often employing the primitive model (ions as charged hard spheres, solvent as a dielectric continuum, if present), can account for both electrostatic correlations and geometric packing constraints [135-137]. For computational efficiency and analytical tractability, simpler models incorporating size effects are widely used. Notably, the lattice-gas model, pioneered by Kornyshev for ionic liquids [138] and independently by Kilic, Bazant, and Ajdari for concentrated electrolytes [139] has become a popular framework. The lattice-gas model included a 'lattice saturation' effect: the ions are only allowed to pack up to a given maximum density in the double layer. This approach accounts for finite ion volumes and predicts non-classical EDL capacitance behavior, such as bell-shaped with a maximum at the potential of zero charge (PZC) or camel-shaped capacitance-voltage curves with two peaks, instead of the U-shape predicted by GCS theory. In both bell and camel-shaped cases, C_d decreases at large magnitudes of the potential. Most simply, this is because at increasing values of the potential, the ions reach their maximum density near the surface and the effective diffuse layer thickness grows larger, leading to a decrease in C_d ([31]. The underlying modified PB equation in these models often leads to Fermi-like distributions for ion concentrations at equilibrium.

For molten salt systems, two phenomena poorly described by GCS theory but captured by these advanced models are particularly relevant: crowding and overscreening [140], illustrated in Figure 16(c) and (d), respectively. The lattice-gas model effectively captures crowding, where high ion concentrations at the electrode surface, especially at relatively high applied voltages (($\frac{100k_BT}{e}$)), lead to the formation of multiple, dense counterion layers. However, standard lattice-gas models, while accounting for steric effects, are still mean-field in their treatment of electrostatics and may not fully capture strong short-range Coulomb correlations [135]. These correlations are crucial for understanding overscreening, a phenomenon typically observed at relatively lower voltages ($\frac{10k_BT}{e}$), where the first ion layer at the electrode surface accumulates more countercharge than the surface charge itself. This leads to subsequent layers experiencing a net charge of the opposite sign, which they, in turn, overscreen, resulting in oscillatory charge density and potential profiles extending from the surface until electroneutrality is achieved in the bulk [140]. Incorporating terms for short-range Coulomb correlations into these models allows for the prediction of such oscillatory profiles, which are consistent with findings from MD simulations of EDL structures in molten salts [141].

The distinct EDL structures in molten salts discussed here, such as ion crowding and potential oscillations, directly impact the interfacial electric field, local reactant concentrations, and adsorption phenomena—all critical factors in determining corrosion mechanisms and rates. Understanding these features, which represent a significant departure from classical dilute solution models, marks crucial progress toward more accurately predicting and mitigating corrosion in these extreme environments.

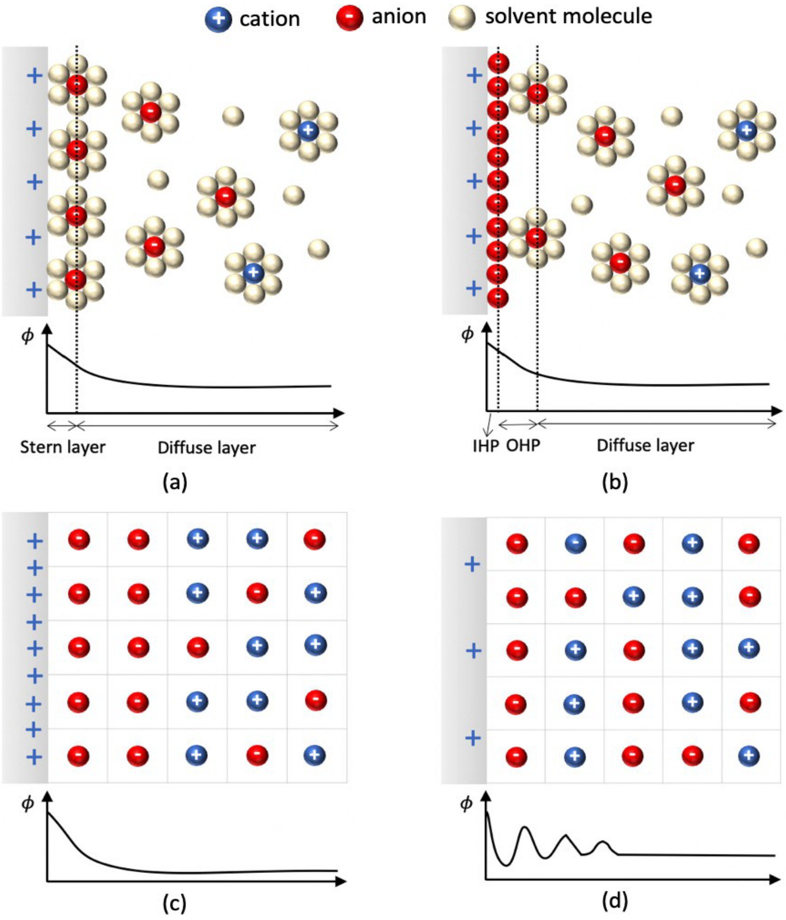

Figure 16: Schematic illustration of different EDL models and their corresponding electrostatic potential (ϕ) profiles. (a) The Gouy-Chapman-Stern (GCS) model, typical for dilute aqueous solutions. (b) The Grahame model for aqueous solutions, distinguishing inner and outer Helmholtz planes. (c) The lattice-gas model depicting ion crowding near the electrode in concentrated electrolytes (e.g., ionic liquids/molten salts) at relatively high applied potential. (d) EDL structure exhibiting overscreening due to strong ion-ion correlations in concentrated electrolytes at relatively low applied potential, leading to an oscillatory potential profile. Figures are reproduced based on Refs. [135, 140, 142].

Atomic scale models: As stated previously, over the past few years, the structure of these double layers has been studied by means of Monte Carlo (MC) simulations [197] and MD, and electronic structure DFT. These methods reveal detailed ionic layering, potential-dependent capacitance, and surface-specific chemistry relevant to electrochemical devices and molten salt reactors. For example, in [199] electronic structure DFT was applied to a series of chloride salts (KCl, LiCl and LiKCl): the DFT calculation outputs were found to qualitatively match those from Monte Carlo simulations and shown to predict realistic trends as to the effects of temperature and potential on the differential capacitance. Over the years, significant improvements to MD potentials have been made such that while these modeling studies are not yet quantitative, they now reveal important trends as to the effect of salt composition on the capacitance and EDL structure. For example, a recent study [203] relying on the use of molecular dynamics simulations reveals that: "in FLiBe, screening involves changes in Be–F–Be angles and alignment of the oligomers parallel to the electrode, while in FLiNaK, the electric field is screened mainly by rearrangement of individual ions, predominantly the polarizable potassium cation". Further the same study illustrates the important data that can be gathered using these methods. For example, it is shown that the differential capacitance in FLiBE is stronger than in FLiNaK. Thanks to the rapid progress in developing interatomic potentials, studies are now beginning to consider actinide containing salts, such as LiCl-KCl-UCl [202]. Table 8 lists some of the atomic scale studies and systems studied.

Overall, the aforementioned body of work clearly delineates important new research avenues that could address the significant epistemic gap pertaining to our understanding of the EDL structure in molten salts. To date, studies are not yet quantitative due to the idealization/simplification of the electrode. Further, a limited number of systems have been studied and the effects of impurities have not been studied comprehensively. We note that machine learning potentials and REAXFF potentials, such as that recently developed of FLiNaK-NiCr [198] can enable far more realistic representation/quantification of the charge transfer between the salt and the metal, thereby opening up the prospects of comprehensively linking the composition of salts to the EDL.

Table 8: Systems Studied in EDL Simulations of Molten Salts

Study	Molten Salt System	Method	Key Focus
[199] Frischknecht et al. (2014)	KCl, LiCl, LiKCl	DFT	Ion density profiles, capacitance at planar electrodes
[200] Kłos & Lamperski (2019)	LiCl, KCl, NaCl with hard/soft repulsions	MD & Monte Carlo	Effect of short-range interactions on EDL structure
[201] Vatamanu et al. (2010)	LiCl	Classical MD	Layering and potential-dependent capacitance on graphite electrodes
[202] U–LiCl-KCl (2024)	LiCl-KCl-UCl_3 mixture	MD	EDL and interfacial energy near uranium electrodes
[203] Lankford et al.	FLiBe, FLiNaK	Constant potential-MD	EDL structure

3.3 Heat Capacity, Viscosity, Density, Diffusion and other Properties

In this section we further detail how atomic scale simulations can be used to extract other critically important properties of molten salts. Specifically, focus is placed on several key properties: the viscosity (μ) -which is particularly hard to measure, the heat capacity (Cp), thermal conductivity, density, and chemical diffusivities. Overall, the accuracy of atomic scale simulations is remarkable. This is best illustrated in the work of Chen et al. [204] who leveraged ab initio MD to simulate the density, diffusion, thermal conductivity and viscosity of LiCl, KCl, and eutectic LiCl-KCl salts. Remarkably, the simulations of all aforementioned quantities, which were performed over a wide range of temperatures, were in excellent quantitative agreement with experimental data. More generally, Table 9 presents some of the influential atomic scale studies of the viscosity, density and thermal conductivities of salts computed using different atomic scale models for both chloride and fluoride salts. Recall that from a fundamental standpoint, the viscosity and thermal conductivity of salts can be obtained via the use of the Green-Kubo relations or via the use of nonequilibrium MD. As detailed in Table 9, atomic scale simulations have been particularly successful at extracting the viscosity, densities and thermal conductivities of salts both from a quantitative and a qualitative standpoint. The data gathered from these simulations can naturally be used to develop chemical models for the salt state, as illustrated in the work of Smith et al. [206]. Critically, the majority of these simulations rely on the use of AIMD which, while accurate, is computationally expensive. As detailed in Attarian et al. [207], the rapid evolution and progress in the development of complex inter-atomic potentials via the use of machine learning paves the way to consider the vast design space of multicomponent salts and to eventually populate a large database of thermophysical properties of molten salts.

Most studies that have been proposed largely focused on the model salts (i.e., discarding the effects of impurities, and fission products). However, in recent years, AIMD and molecular dynamics simulations have seen their first deployment to study impurities, fission products, and lanthanides in various molten salts. Among others, Emerson et al. showed the broad, network-forming nature of $LaCl_3$–NaCl. Zhu et al. studied the effect of La on a series of properties in LiCl-KCl-CsCl-$LaCl_3$ melts. These include the self-diffusion coefficient, viscosity, ionic conductivity, heat capacity, thermal expansion coefficient, and thermal conductivity. This study clearly shows the important impact of fission products on thermophysical properties of salts. For example, the heat capacity was seen to adopt a non-monotonous dependence on $LaCl_3$ concentrations, with an overall effect which was not very significant over the range of wt% of $LaCl_3$ considered (0 to 12). On the contrary, $LaCl_3$ was found to have decreased the thermal expansion coefficient by up to 8 % [210,211].

Overall, while these results are promising, it must be noted that the literature remains particularly sparse and disconnected. Given the increased interest in studying thermophysical properties of salts and the prospect of machine learning based methods, it is likely that additional knowledge will be added to fill these gaps/deficiencies, in the coming years.

Table 9: Important atomic scale studies of thermophysical salts [204-211]

Study / year	Salt(s)	Interaction Model	Key Take-aways	Quantities computed
Chen et al. 2015 [205]	LiCl-KCl eutectic, LiCl, KCl	Ab-initio MD (DFT/PBE)	Predicted shear viscosity within ≈15 % of high-T data; proved fully first-principles route	Ionic conductivities, shear viscosities, thermal conductivities, density, diffusion coefficients
Smith et al. 2020 [206]	$LiF–BeF_2$ (FLiBe) series	Polarizable-ion model (PIM)	Excellent agreement with experimental data	Heat capacities, molar enthalpies, thermal expansions, density, molar volumes, thermal conductivity
Attarian et al. 2024 [207]	$NaCl–MgCl_2$ binary	ML Atomic-Cluster-Expansion (ACE)	Machine-learned force field reaches <5 % error vs AIMD while running 100× faster. Density is predicted within 6 % for NaCal	Density, radial distribution function, viscosity
Lambrecht et al. 2022 [208]	$MgCl_2$-NaCl-KCl	MD	Moderate overestimation of the thermal conductivity	Thermal conductivity, viscosity
Andersson, 2022 [209]	NaCl-UCl_3	AIMD	Excellent agreement with experimental data. Loss of accuracy is however noted for the density at a high fraction of UCl_3	Density, heat capacity, Diffusion coefficient, radial distribution functions, compressibility

3.4 Summary

This section presented a state-of-the-art overview of modeling techniques used to predict critical properties of molten salts, especially in the context of molten salt reactors (MSRs). Key focus areas included predicting electrochemical driving forces for corrosion (Red/Ox potential), understanding the salt/metal interface (especially the electric double layer), and evaluating thermophysical properties such as viscosity and heat capacity. Electrochemical predictions rely heavily on thermodynamic modeling using databases like MSTDB-TC, which show strong agreement with experimental data but currently lack coverage for impurities and fission products. These gaps are significant because such elements can dramatically affect corrosion behavior. Models based on the Modified Quasi-Chemical Model (MQM) and tools like Thermochimica have demonstrated high accuracy in reproducing redox potentials. However, further refinement and validation are recommended to ensure predictive reliability under realistic reactor conditions.

In parallel, the quantitative effects of the EDL, a key factor in governing corrosion kinetics at the salt/metal interface, remains poorly understood in molten salts. Molecular dynamics and density functional theory simulations have revealed insights and data about ion crowding and overscreening phenomena, yet current models are limited by simplified system assumptions and a lack of data on impurities and radiation effects. More realistic and complex EDL modeling, using machine learning and REAXFF potentials, is a promising direction of modeling advances. Thermophysical properties such as viscosity, density, diffusion coefficients, and heat capacity have been extensively modeled using ab initio and molecular dynamics simulations. These models, though computationally intensive, often agree well with experimental data and have a crucial role in populating property databases. Increasing the use of interatomic potentials derived from machine learning is enabling exploration of multi-component salts and the effects of fission products and impurities. Nonetheless, the existing literature is sparse, and more coordinated studies are needed to ensure comprehensive coverage. In summary, while the current modeling framework provides robust tools for evaluating molten salt behavior, significant challenges remain—particularly in incorporating impurities, fission products, and interfacial reaction rates. Ongoing developments in databases, atomic scale simulations, and machine learning are expected to bridge these gaps, enabling more predictive and transferable corrosion models for use in advanced reactor designs.

4 Review of Models for Molten Salt Corrosion

This section presents a concise overview of modeling efforts to predict molten salt corrosion. The overarching goal of the modeling community is to develop comprehensive models that relate the salt and metal compositions (including impurities and fission products) to all features of corrosion both in equilibrium and out-of-equilibrium conditions (such as under irradiation). Key metrics of interest are the mass loss over time, the depth of the corrosion front, change of composition of the metal being corroded, and morphologies of the corrosion front. Note that the sole investigation of mass loss over time is not sufficient to provide a sense of the deleterious effects of corrosion on the integrity of the vessel. This fact was already realized and detailed in the MSRE reports which showed that cracks or other salt incursions could lead to stress intensities in the vessel [226,227].

The complexity associated with understanding molten salt corrosion arises from the intricate interplay between chemical compositions and corrosion mechanisms, and the influence on chemistry of the electrical double layer at metal-salt interfaces. Additionally, numerous numerical challenges exist in developing stable and computationally efficient corrosion models. To fully grasp the several competing processes mediating molten salt corrosion (i.e., diffusion in the bulk, electron transfer at the interface, diffusion in the salt, etc.), this section of the report first recalls the different unit processes that can mediate corrosion, using experimental tests as motivation. Among other variations, the differences between planar corrosion and dealloying corrosion are discussed. Dealloying corrosion is a selective corrosion process where one or more elements are preferentially dissolved and removed from an alloy, leaving behind a weakened, porous structure. This selective removal typically occurs due to differences in the electrochemical potentials of the alloy's constituent elements (e.g. Ni vs Cr as per Section 3), and chemical kinetic effects. In terms of chemical kinetic effects, special attention must be paid to the crucial role of grain boundaries, which can accelerate diffusion and facilitate rapid ingress of molten salts into metals, and to the likely formation of Kirkendall voids in microstructures. These voids form inside metals during diffusion processes, occurring due to unequal diffusion rates of different atomic species of alloy compositions in the structural materials. We note that the effect of grain boundaries on the topology of the corrosion front likely depends on the grain boundary character.

After laying out the fundamental aspects of molten salt corrosion, we surveyed various modeling methodologies developed to predict corrosion behavior. Currently, no single model exists that comprehensively predicts how metal and salt compositions, inclusive of impurities and fission products, simultaneously influence corrosion mode, mass loss, and compositional changes in the metal. A significant portion of this limitation is largely due to the incompleteness of existing thermodynamic databases and due to the incompleteness of the current understanding of the electrical double layer structure (and associated phenomena). Nonetheless, numerous models have been proposed to predict either the composition change, or the mass loss and composition change in the metal or the corrosion mode and metal composition change (among others). Importantly, as will be shown, some models have been successfully connected to thermodynamic and thermo-kinetic databases (such as CALPHAD for the metal and MSTDB-TC for the salts); thereby paving the way to comprehensively relate composition to corrosion rates, to the morphology of the corrosion front, and to microstructure changes in the metal. Despite these advancements, the extrapolative capabilities of existing corrosion models remain relatively untested, with most demonstrations limited to semi-empirically interpolating rates within calibrated composition and temperature ranges. Therefore, as modeling techniques evolve to non-empirical predictions, it will become increasingly important to design targeted experiments for rigorous calibration and validation, specifically assessing their predictive accuracy outside known data ranges. In other words, while significant progress has been made over the past years to bridge the gap between modeling and simulation efforts and characterization, continued efforts will remain necessary to develop utilitarian composition sensitive corrosion models.

The later portion of this section succinctly outlines various modeling approaches utilized for predicting molten salt corrosion rates and morphologies, including empirical models, one-dimensional thermokinetic models, advanced phase-field simulations, and surrogate models. The intent is to evaluate practical methodologies suitable for assessing the potential impacts of fission products on molten salt properties, rather than providing extensive mathematical derivations, which are available in Appendix A. Broadly, modeling approaches discussed in the literature are categorized into empirical and mechanistic models, each serving fundamentally different purposes. Empirical (phenomenological) models offer simplicity and ease of use but are typically limited to interpolation within or near data ranges of known properties and behavior, lacking robust predictive power as compositions/conditions are changed and providing no or limited causal insights. Conversely, mechanistic models, grounded in fundamental physical principles, hold the potential for predictive extrapolation, albeit contingent upon assumptions and simplifications necessary to manage the multi-physics complexities involved. Physics-based models typically encompass sharp-interface or diffuse-interface approaches, differing in how metal-salt interfaces are numerically treated: either assuming the compositions change like a step function at the interface, or in a continuous way, respectively. Physics-based models' computational requirements vary significantly based on model complexity and underlying assumptions regarding coupled phenomena such as charge and ionic transport. Due to these numerical complexities, surrogate models have emerged as attractive alternatives, capable of offering high-fidelity predictions at significantly lower computational costs compared to traditional physics-based simulations. In multi-scale modeling approaches, a combination of physics-based and surrogate-based modeling can be used. The incorporation of surrogate models thus represents promising tools for rapid assessment and decision making within molten salt corrosion research.

Finally, this section concludes by summarizing and comparing the discussed modeling methodologies, highlighting their strengths, limitations, computational efficiency, ease of use, and potential for extrapolation. It also outlines contemporary strategies for developing practical, predictive corrosion models that effectively incorporate the influences of impurities and fission products. These tools may support informed reactor design, materials selection, and reviews, for safe and efficient molten salt reactor operation.

4.3 Unit Processes Mediating Corrosion

This section briefly presents the complex processes that impact and condition corrosion of metals exposed to molten salts. Note that molten salt corrosion experiments are inherently challenging due to demanding high temperatures, potential salt impurities, and requisite long durations. Computational simulations therefore offer a valuable complementary approach, enabling the prediction of structural material degradation, greater control over system parameters, and deeper investigation into atomic scale corrosion mechanisms. Accurately predicting mass loss, corrosion depth, and the overall microstructure and composition evolution of the corroded metal during reactor operation hinges on a comprehensive understanding of the fundamental corrosion steps and their coupled interactions. Figure 17(a) is a sketch representing the corrosion of a structural alloy in contact with a molten salt phase. Some corrosion modes involve selective corrosion of the less noble species. Here the phrase 'more noble species' refers to species more resistant to corrosion, and which does not easily oxidize.

At the interfacial region, the corrosion process can be broadly characterized by the following steps: (1) oxidation/dissolution of the less noble atoms (e.g., Cr in a $Ni - Cr$ alloy), (2) diffusion of corrosion products/reactants in the salt away from/toward the interface, (3) diffusion of reactants in the solid, including along the grain boundary, (4) surface diffusion of the more noble atoms (e.g., Ni in a Ni−Cr alloy), and (5) surface charging causing the salt-ion ordering and electric double layer.

Due to the competition and correlation of the corrosion steps, a range of corrosion modes can occur resulting in different interfacial morphologies, with a few typical modes shown in Figure 17(b) and their corresponding experimental characterization results in Figure 17(c). These corrosion modes include planar corrosion, preferential grain boundary dealloying corrosion and bulk dealloying corrosion. In a comprehensive study, Terrapower clearly demonstrated and illustrated the range of corroded microstructure that can be observed experimentally [212]. Importantly, depending on the location, different corrosion fronts can be observed for the same material exposed to the same conditions such that overall, corroded morphologies are particularly complex. Figure 17(b1) depicts a slowly advancing corrosion front, which is passivated by the enrichment of more noble species from the alloy at the interface. This enrichment is represented by the increasing red intensity toward the interface. In Figure 17(c1), $Ni - 20Cr$ was exposed to molten $FLiBe$ for 1000 h. We note that often voids can be observed. These can reach a couple of microns in diameter. They are typically separately distributed within the near-surface layer, but not preferentially at grain boundaries. Figure 17(b2) shows an example of preferential corrosion through grain boundaries. The experimental counterpart is shown in Figure 17(c2) which shows a 316 stainless steel sample in graphite capsules at 700℃ after 3000 h [14]; where the least noble species is depleting mostly along the grain boundary, as observed in Figure 17(c2), which shows a 316 stainless steel sample in graphite capsules at 700℃ after 3000 h [14]. Figure 17(b3) illustrated yet another corrosion morphology. Specifically, it shows bicontinuous-like structure with nodes rich in the more noble species, like the characterized $Ni - 20Cr$ surface in KCl–$MgCl_2$ at 800℃ after 200 min [15] in Figure 17(c3). Importantly, voids deep into the base metal are typically observed. This is illustrated in Fig. 17(b4), which depicts that voids deep in the alloy bulk (at distances beyond 50 micrometers from the surface) can also appear. Such voids have been observed in Hastelloy alloy N in LiF–BeF_2–ThF_4–UF_4 at 700℃ after 4741 h [16]. The resulting morphology and mass loss from corrosion are the results of thermodynamic and kinetic coupling between salt and alloy across time and length scale. In other studies conducted by Terrapower in which a series of alloys (e.g., 316H, alloy 600, alloy N, etc.) were exposed to chloride salts in a microloop [212], voids were commonly observed in all materials tests. These were identified as Kirkendall voids, formed due to differential diffusion rates of alloying elements, causing vacancies to accumulate into extensive porous structures beneath the alloy surface. This mechanism significantly impacts the mechanical integrity and corrosion resistance of alloys.

This concise overview of the different corrosion modes that are typically observed as metals are exposed to molten salts clearly shows that the sole consideration of mass loss provides a largely incomplete view of the effects of corrosion on the composition and microstructure of metals. Thus, in what follows, models will be critically presented and their ability to predict the morphology of the corrosion front, the change in composition in the metal, localized grain boundary attacks and voids will be discussed. In addition, the abilities of models to predict the effects of composition of the salt and of the metals, including fission products will also be presented.

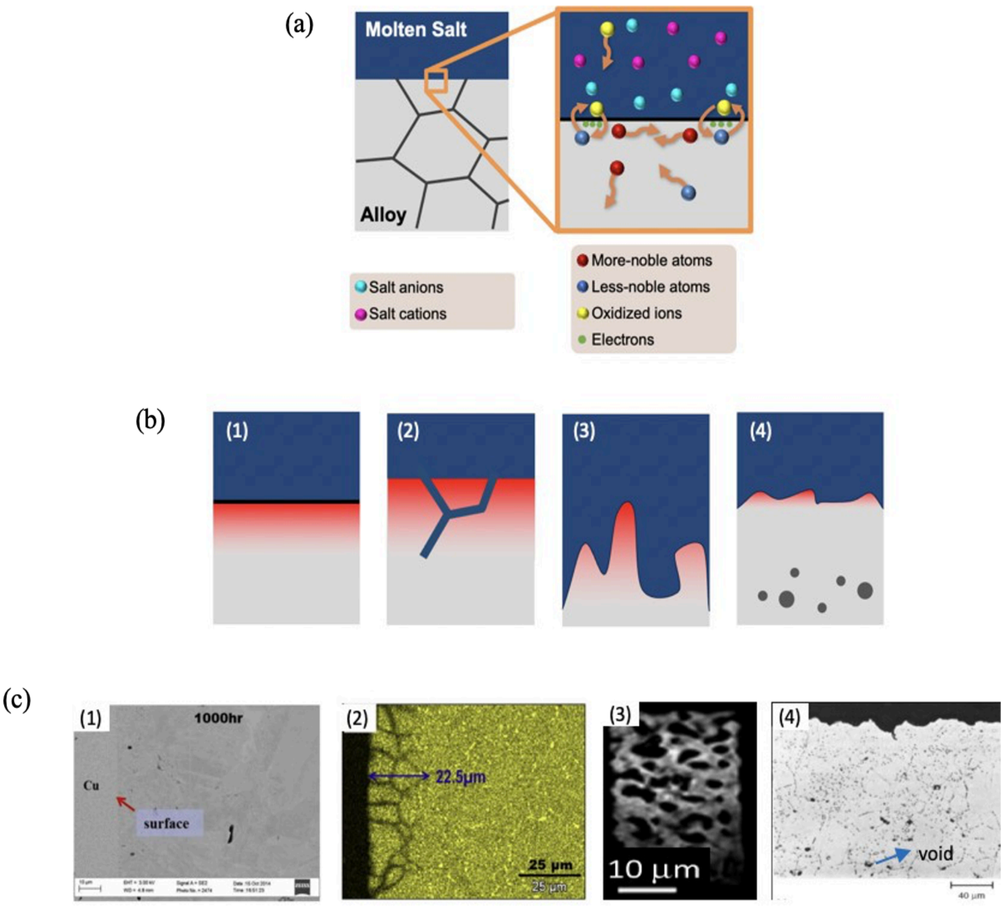

Figure 17: Sketch of structural alloy corrosion in molten salt and experimental measurements. (a) magnification of the interfacial corrosion steps, and (b) four typical corrosion modes. (b1) flat corrosion front, (b2) grain boundary attack, (b3) dealloying corrosion leading to a bicontinuous microstructure, (b4) voids deep in the alloy bulk. (c) experimental measurements with similar interfacial morphology to (b). (c1) is a cross-sectional Scanning Electron Microscope (SEM) image of $Ni-20Cr$ exposed to molten *FLiBe* at 700℃ after 1000 h [13]; (c2) shows an EDS map of Cr distribution in near-surface layer of a corroded 316 stainless steel sample in graphite capsules at 700◦C after 3000 h [14], (c3) shows $Ni-20Cr$ in KCl– $MgCl_2$ at 800°C after 200 min [15], and (c4) shows Hastelloy alloy N in LiF– BeF_2–ThF_4–UF_4 at 700°C after 4741 h [16].

4.4 Empirical Laws: Applications and Underlying Assumptions

The simplest form of models that can be used to ‘predict’ molten salt corrosion is empirical laws. Many attempts have been made to fit macroscopically measured corrosion rate as a function of time in various fields of study such as aqueous corrosion, liquid metal dealloying, and corrosion in molten salts for next generation concentrated solar power and MSRs. In general, empirical models are macroscopic models that can potentially simulate corrosion processes over long periods at low computing cost. They allow for the fit/prediction of corrosion rates over time and help distinguish between interface-controlled and diffusion-controlled mechanisms. These models generally focus on the mass loss and depth of corrosion as a function of time. Typically, they are 1D models and only provide an average value of the corrosion state and therefore do not capture the complexities of advanced corrosion fronts, such as those along grain boundaries. In addition, the fit of these models is highly sensitive to factors such as reactants, temperature, and fluid and flow properties. As a result, while these models can potentially make predictions that are interpolative (within the range of compositions and temperatures for which they have been fitted) these empirical models cannot be used for reliable extrapolative predictions (outside of the range of compositions and temperatures for which they have been fitted). Thus, fully empirical models, which are disconnected from the thermodynamics of the system, cannot be used to reliably help with material selection and component design. Further they cannot consider any complex effects of composition, fission products etc. as they are simple fits to experimental data. Thus, building a comprehensive understanding of the linkage between composition (i.e., salt, metal) and mass loss from the use of empirical laws would require extensive testing. Despite their limitations, we note that empirical models could, in principle, be used to extrapolate corrosion to longer times, modeling the evolution of mass loss and corrosion depth from the use of short to moderately long experiments. To date, an assessment or general metric to assess the minimum duration of experiments necessary to calibrate the models (for any given system and set of conditions) has not been proposed. Establishing methods to estimate the minimum durations of measurements would enable a more optimal design of experiments. In what follows we briefly recall the principle and foundations of empirical models.

Typical salt and material compositions for MSRs do not involve formation of a corrosion passivating oxide layer. Therefore, only two 1D empirical laws are commonly used to describe the corrosion rate: linear and parabolic laws.

The 1D empirical linear law is expressed as:

$$x = k_l t + x_0 \tag{34}$$

and the corresponding velocity of the corrosion front is simply given by:

$$v = k_l \tag{35}$$

where x is a length and k_l is a linear rate constant. Depending on the application, this length may represent motion of the corrosion front (i.e. how much metal was lost), the thickness of the formed oxide layer, or the depth of the resulting porous metal structure. This law can also be expressed in terms of mass loss over time, where the velocity corresponds to the corrosion rate. However, both formulations are equivalent.

The linear form can be rationalized on the basis of the competition between different rate limiting processes. Indeed, linear models are typically related to an interface-controlled mechanism. However, for dealloying, reference [15] has suggested that a linear rate may also arise from a second interface-controlled step: the diffusion of the more noble metal along the solid/liquid interface. In both cases, the linear law can be related to the rate-limiting step of the reaction, which depends on the concentrations of reactants and the rate constants. This is, in fact, the basis of the Butler-Volmer (BV) expression, which relates the reaction rate to the concentrations of reactants and the activation energy barriers. Because diffusivity is non-limiting here, with continuous removal of products and a large excess of the corroding salt, concentrations of reactants can be approximated as constant, and the corrosion rate can thus be approximated as constant. For aqueous corrosion, a linear law was assessed for several systems such as AuAg dealloying at room temperature with nitric acid flow [115]. For molten salt corrosion, such a law was observed with 45 Steel at 500°C in molten nitrate salts [116]. However, although a linear law often describes the initial stages of corrosion, diffusion may progressively become rate-limiting, particularly if a so-called diffusive layer exists in the near surface region of the solid, where the elements are gradually leached from the solid with the rate of diffusion through the diffusive layer being significantly rate-determining for their removal. In practice, the elemental concentration profile of such diffusion layers is expected to be impacted by the salt circulation in the reactor.

There are other systems which are better described by the 1D empirical parabolic law, expressed as:

$$x^2 = k_p t + x_0^2 \tag{36}$$

and the corresponding velocity of the corrosion front is thus given by:

$$v = \frac{k_p}{2\sqrt{k_p t + x_0^2}} \tag{37}$$

with k_p, a parabolic rate constant.

The parabolic form is typically attributed to long-range diffusion-limiting processes. Simple models using Fick's laws and Laplace transform for resolution with simplified interface boundary conditions easily justify the parabolic law. Importantly, the expression of the diffusion coefficient differs depending on the medium. Mainly, Arrhenius theory is used for solids while the Stokes-Einstein theory is applied for liquid phases. As diffusion is supposed to be limiting for the parabolic law, Nernst's local equilibrium applies at the interface.

For classical planar corrosion without oxide formation, if diffusion is rate limiting, an analytical solution similar to Cottrell's expression for diffusion-controlled current can easily justify a parabolic corrosion law. Below illustrates the 1D Cottrell equation, supposing a case where a liquid limiting diffusive species, A, is coming to the interface (typically A would be the oxidant), Here, Nernst's local equilibrium is simplified to $C_A(0,t) = 0$ for $t > 0$, with the concentration of A denoted by $C_A(x,t)$. We suppose, as well, that the concentration of A remains constant far away from interface, $\lim_{x\to\infty} C_A(x,t) = C_A^*$, and that the concentration of A was homogeneous before corrosion $C_A(x,0) = C_A^*$. Using Fick's diffusion equations, the diffusivity of A D_A, and leveraging a Laplace transform, one obtains:

$$\frac{\partial C_A(x,t)}{\partial t} = D_A \frac{\partial^2 C_A(x,t)}{\partial x^2} \tag{38}$$

$$C_A(x,t) = \frac{2C_0}{\sqrt{\pi}} \int_0^{\frac{x}{2\sqrt{D_A t}}} e^{-u^2}\, du = C_0 \operatorname{erf}\left(\frac{x}{2\sqrt{D_A t}}\right) \tag{39}$$

Moreover, as the molar consumption rate per unit area is limited by the diffusion of A, it is equal to $\frac{J_A(0,t)}{\nu_A}$ with $J_A(0,t)$ the flux of A coming from the liquid and ν_A the the stoichiometric coefficient of species A in the corrosion reaction. Using Fick's laws $J_A(0,t) = -D_A \left.\frac{\partial C_A(x,t)}{\partial x}\right|_{x=0}$. Finally, we get

$$v = \frac{M_M.\nu_M}{\rho_M \nu_A} \frac{C_A^*}{\sqrt{\pi D_A t}} \tag{40}$$

with v the velocity corresponding to the length described above and M_M, ν_M, ρ_M respectively the molar mass, the stoichiometric coefficient, and the mass density of the species M being corroded. This corrosion front velocity can be related to a current density (when only half of the reaction is considered) as follows:

$$i(t) = \frac{nFSC_A^*}{\nu_A.\sqrt{\pi D_A t}} \tag{41}$$

Where i is the equivalent corrosion current density, *n* the number of electrons exchanged for a single reaction, *F* Faraday's constant, and *S* the total surface of metal M exposed to corrosion. It must be emphasized here that the rate-limiting diffusive species could be any species involved in Nernst's local equilibrium at the interface (i.e. oxidants, products, or reactants).

In molten salts, the parabolic law can be fitted in two different regimes of corrosion: above the parting limit and below the parting limit. The 'parting limit' is a threshold of the least noble element in the alloy, a composition range below which the corrosion front remains planar because there is no substantial difference in the dissolution rate of different elements. As a result of this behavior, below the parting limit, the parabolic law can often be justified by the rate-limiting diffusion of liquid species in the porous corroded area. One can use an effective diffusion coefficient considering rugosity ε and tortuosity τ to adapt Cottrell's equation:

$$D_{\text{eff}} = \frac{D_0\, \varepsilon}{\tau^2} \tag{42}$$

where ε is the rugosity and τ is the tortuosity of the structure. τ was properly defined in [120,121] as a 3D parameter equal to the ratio of a tortuous diffusion path and a straight diffusion path.

The parabolic law was fitted in this manner for corrosion of Ni–20Cr dealloying in KCl–$MgCl_2$ molten salt at 800 °C [15]. Early studies similarly showed that the corrosion of Ni-20Cr in KCl-NaCl mixtures between 700°C and 800°C, under oxygen gas injection, also followed a parabolic law with respect to the growth of the porous layer over the ten first hours [117]. Finally, liquid metal dealloying experiments, which lead to similar corrosion morphologies as those observed experimentally in molten salt corrosion [118,119], showed that reactants were not always the rate-limiting diffusive species: in Ti-Ta dealloying in contact with liquid Cu, diffusion away from the interface of Ti was rate limiting and inducing parabolic law [120].

Below the parting limit (i.e., the critical concentration of the least noble species above which selective dissolution occurs), corrosion in molten salts kinetics is often governed by diffusion of the less noble element from the bulk solid to the interface. Once again, Cottrell's law can be adapted using Arrhenius theory for the expression of diffusivity, and a 1D empirical parabolic law can be used. This was evidenced in dealloying of MgCd in both a Choline Chloride (ChCl) and Urea eutectic mixture (ChCl-Urea), and 1-Butyl-3-Methylimidazoliumm bis-Trifluoromethylsulfonate (BMImTfSI), at a temperature of up to 210°C [123]. A parabolic law was fitted and explained with the same reasoning as for corrosion of Ni-based alloys in NaCl-KCl-$MgCl_2$ at temperature above 600°C [26]. Nevertheless, systems following a parabolic law may revert to linear behavior under certain conditions. In corrosion processes without a protective oxide layer, the diffusion layer may reach a maximum thickness, after which species fluxes become constant, resulting in a linear corrosion rate. This limiting diffusion thickness may arise from convection or from structural constraints of the porous layer.

Other kinetic rate forms have also been observed, particularly in corrosion processes that involve oxide formation. These include logarithmic and inverse logarithmic depletion behaviors [124,125], reflecting distinct mechanisms depending on temperature and chemical environment. Various models, such as those by Cabrera-Mott or Ely and Wilkinson, have been proposed to explain these behaviors. With passivation of the interface by more noble elements, dealloying in molten salts may also experience logarithmic depletion laws at early stages, as simulated in [126] and seen in [127]. Corrosion rate regressions over time can exhibit a wide range of mathematical forms. Time-dependent power laws have been fit for various applications where both diffusion and interfacial reaction contribute [128].

Finally, recent work has attempted to perform non-physical empirical regressions that are completely phenomenological, such as Gaussian process regression techniques with varied kernels to predict the corrosion rate over time [129]. These higher-level regressions may be more extensible to complex regressions using other parameters than time to predict the corrosion rate (for example, regressions that include the atomic properties of the individual elements and compounds among the parameters).

4.5 Electrochemical Kinetic Models

As stated in the Section 2 of this technical letter report, electrochemical methods are often used to study molten salt reactions and to extract important quantities of interest for describing the intrinsic unit steps associated with corrosion (e.g., diffusion, reaction at the interface). Interpretation of these experiments often leverages analytical models. Interestingly, these models can also be leveraged to predict molten salt corrosion. Similarly to empirical corrosion models, electrochemical kinetic models (EKM) are typically limited to one-dimensional corrosion front models. Importantly, EKM are generally entirely concerned with the reaction rates at the salt-metal interface. As such, they are ill suited to predict corrosion over extended periods of time. Indeed, EKM tend to have linear rate forms whereas extended exposure to molten salts typically yields parabolic rate forms. Nonetheless EKM have the key advantage of being compatible with the use of thermodynamic databases such as MSTDB-TC. As such, these models could shed light on the linkage between molten salt composition, metal composition and oxidation rates at the interface. As will be presented below, EKMs largely rely on the Butler-Volmer equation. Pragmatically, the Butler-Volmer equation describes the electron transfer rate at the salt-metal interface, given an imposed overpotential. In practice, these models also necessitate significant calibration (which can be performed via the use of cyclic voltammetry) to accurately predict reaction rates. The need for calibration is largely due to our imperfect knowledge of the structure of the EDL. Despite their limited use, EKMs are briefly summarized below as they lay the foundation for the development of integrated modeling approaches.

The net rate for a redox reaction at the metal-salt interface can be related to the current according to Faraday's law:

$$\Delta m = \frac{IM\Delta t}{nF} \tag{43}$$

where Δm is the weight dissolved from the electrode, M is the molar mass of the oxidized species, Δt is the time passed, and I is the current passed through the metal-salt system. Specifically, the heterogeneous reaction kinetics can be described by the current-potential characteristic [77]

$$i = FAk_s \left\{ c_O^s \exp\left[-\frac{\alpha nF}{RT}\left(E - E^{0'}\right)\right] - c_R^s \exp\left[\frac{(1-\alpha)nF}{RT}\left(E - E^{0'}\right)\right]\right\} \tag{44}$$

where i is the Faradaic current density in units of $[C \cdot s^{-1} \cdot m^{-2}]$, A is the surface area of the active electrode in units of $[m^2]$, k_s is the standard rate constant in units of $\left[\frac{m}{s}\right]$, c_j^s is the concentration next to the interface in units of $\left[\frac{mol}{m^3}\right]$, α is the unitless transfer coefficient and is indicative of the symmetry of the energy barrier [213] for a single electron transfer step.

The Faradaic current reflects the competition between the forward and backward reaction. The current, and current density, can be described in terms of the overpotential, $\eta = E - E_{eq}$ (defined as the deviation from the equilibrium potential). This relationship is given by the current-overpotential equation [77].

$$i = i_0 \left[\frac{c_O^s}{c_O^b} \exp\left(-\frac{\alpha nF}{RT}\eta\right) - \frac{c_R^s}{c_R^b} \exp\left(\frac{(1-\alpha)nF}{RT}\eta\right)\right] \tag{45}$$

where c_j^b is the bulk concentration. The exchange current density can be calculated from $i_0 = FAk_s(c_O^b)^{(1-\alpha)}(c_R^b)^{\alpha}$, with variables as defined above, assuming ideal mixing among all species. If the molten salt is well stirred such that the surface concentrations do not differ appreciably from the bulk values, then Equation (45) becomes

$$i = i_0 \left[\exp\left(\frac{-\alpha nF}{RT}\eta\right) - \exp\left(\frac{(1-\alpha)nF}{RT}\eta\right)\right], \tag{46}$$

which is known as the Butler-Volmer (BV) equation. At the corrosion potential where the net current for all electrode reactions on the metal surface is zero, the rates of the reverse reactions for both the metal dissolution and oxidant reduction are typically negligible [41]. This leads to the Tafel equations where the cathodic and anodic current densities are $i_c = i_{c0} \exp\left(-\frac{\alpha_c nF}{RT}\eta_c\right)$ and $i_a = -i_{a0} \exp\left(-\frac{\alpha_a nF}{RT}\eta_a\right)$, respectively. Additionally, under low overpotential η, linearization of Equation (46) leads to

$$i = -i_0 \frac{nF\eta}{RT}. \tag{47}$$

The standard kinetic BV model is based on a dilute solution approximation [130]. In molten salts, the concentration of ions (e.g., Na+, Cl-, Li+, F-) is much higher than in dilute aqueous solutions. Additionally, the high-temperature molten salt mixture results in ions in close proximity to each other; the high ionic strength further results in strong short-range ordering, which alters the corrosion process significantly compared to dilute systems. To generalize the BV model to account for concentrated solutions, in a seminal paper by Bazant [130], the electrochemical potential was expressed as follows:

$$\overline{\mu}_i = RTlna_i + \mu_i^0 + z_i e\phi_i = RTln\tilde{c}_i + \overline{\mu}_i^{ex} \tag{48}$$

where $\tilde{c}_i$ is a dimensionless concentration from the species concentration divided by its standard state, $z_i e$ is the charge, ϕ_i is the coulomb potential of mean force, and the excess electrochemical potential $\overline{\mu}_i^{ex} = \mu_i^0 + RTln\gamma_i + z_i F\phi_i$. In Ref. [130], instead of the total free energy, the excess electrochemical energy landscape is explored (as shown in Figure 18(a)), since the dimensionless concentration term in Equation (48), $RTln\tilde{c}_i$, encompasses the effects of fluctuations. Based on the excess electrochemical potential of the transition state, $\overline{\mu}_{\ddagger}^{ex}$, defined by Bazant, the postulated reaction excess electrochemical potential is separated into chemical and electrical components. For a general Faradaic reaction $O + ne^- \rightarrow R$, the transition state excess electrochemical potential is:

$$\overline{\mu}_{\ddagger}^{ex} = RTln\gamma_{\ddagger} + (1-\alpha)(z_O e\phi_O - ne\phi_e + \mu_O^0 + n\mu_e^0) + \alpha(z_R e\phi_R + \mu_R^0). \tag{49}$$

Such that $\overline{\mu}_{\ddagger}^{ex}$ is calculated by: (1) averaging the standard chemical potential of the initial and final states as shown in Figure 18(c), contrary to Ref. [131] where the transition state standard chemical free energy is independent from the reactant and product energies, (2) averaging the electrostatic potential as shown in Figure 18(b), which assumes a constant electric field across the reaction coordinate, (3) including the transition state excess mixing potential as shown in Figure 18(d). Specifically, in Figure 18(b), the solid vertical line represents the transition state along the reaction coordinate, and its intersect with the applied potential $\Delta\phi^{app}$ determines the electrostatic overpotential for the forward and backward reactions $\alpha nF\eta$ and $\beta nF\eta$ where $\beta = 1 - \alpha$, similar to shown in Refs. [132,133]. In Figure 18(c) and (d), μ_{ref}^0 γ_{ref} are associated with the reference states which need to be consistent between the initial and the final states.

Using $\overline{\mu}_{\ddagger}^{ex}$, the concentrated solution-corrected exchange current is given by:

$$I_0 = \frac{k_0 ne(a_O a_e^n)^{1-\alpha} a_R^\alpha}{\gamma_{\ddagger}} = k_0 ne(\tilde{c}_O \tilde{c}_e^n)^{1-\alpha}(\tilde{c})_R^\alpha \left[\frac{(\gamma_O \gamma_e^n)^{(1-\alpha)}\gamma_R^\alpha}{\gamma_{\ddagger}}\right] \tag{50}$$

where k_0 is the reaction rate constant and the factor in the brackets is a thermodynamics-based term to account for the electrostatic potential.

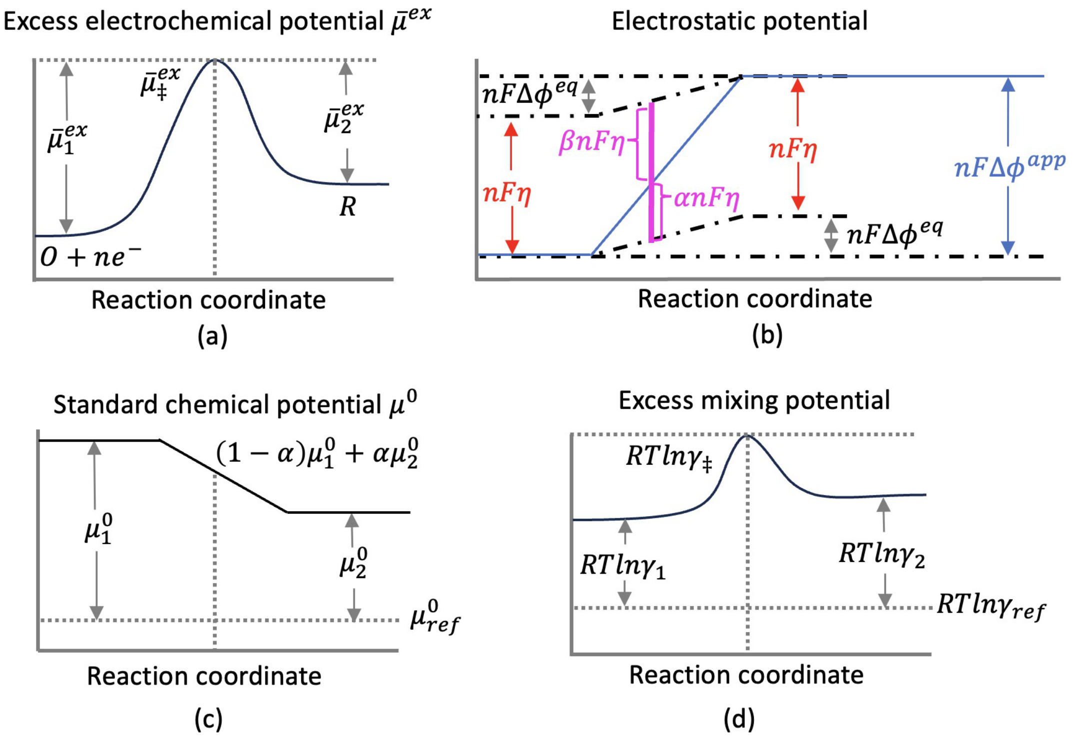

Figure 18: Electrochemical potential landscape of the Faradaic reaction O + ne– ⇌ R, postulated based on the thermodynamically consistent nonequilibrium theory [130]. (a), (b), (c), and (d) are, respectively, the excess electrochemical potential, electrostatic potential, standard chemical potential, and excess mixing potential of the reactants, products, and the transition state. The subscripts indicate states along the reaction coordinate.

Marcus kinetics is a microscopic theory of charge transfer that provides justification for the BV equation and a means to estimate its parameters based on the solvent reorganization. Bazant [130] extended the classic Marcus theory for concentrated solutions and nonequilibrium thermodynamics. Considering a forward (cathodic) reaction with one electron transferred the barrier for the reaction is defined as

$$\Delta G_c^{ex} = \frac{\lambda}{4}(1 + \frac{\Delta G^{ex}}{\lambda})^2 \tag{51}$$

where λ is the reorganization energy, and $\Delta G^{ex} = F\eta + RTln\frac{\tilde{c}_O\tilde{c}_e}{\tilde{c}_R}$. In Ref. [77], the forward reaction energy of an electrode reaction is defined as

$$\Delta G_f^{\ddagger} = \frac{\lambda}{4}\left[1 + \frac{F\left(E - E^{0'}\right)}{\lambda}\right]^2 \tag{52}$$

To reveal the differences and similarities between the descriptions from the two sources, $E - E^{0'}$ in Equation (52) can be written as $\frac{RT}{F}ln\frac{\tilde{c}_O\tilde{c}_e}{\tilde{c}_R}$ using the Nernst Equation. Comparing Equation (51) with Equation (52), one can easily see that $\Delta G_c^{ex} = \Delta G_f^{\ddagger}$ at equilibrium state when $\eta = 0$. The former can capture the overpotential effect out of equilibrium. The distinctions between the treatments of Marcus kinetics can also be revealed similarly through the relationship between α and λ. In Ref. [130],

$$\alpha_{Bazant} = \frac{1}{2}\left(1 + \frac{RT}{\lambda} ln \frac{\tilde{c}_O \tilde{c}_e}{\tilde{c}_R}\right), \tag{53}$$

and in Ref. [77],

$$\alpha_{Bard} = \frac{1}{2} + \frac{F\left(E - E^{0'}\right)}{4\lambda} \tag{54}$$

(neglecting the work required to bring the reactants and products together). Note that in Marcus theory and these extensions of Marcus theory, α changes with concentration, overpotential, and temperature. Due to the difference in the prefactor in Faraday current density i, to compare α_{Bazant} with α_{Bard}, the former is converted to $\alpha_{Bazant'} = \alpha_{Bazant} - \frac{F\left(E-E^{0'}\right)}{4\lambda}$. Using Nernst's equation, it can be shown again that $\alpha_{Bazant'} = \alpha_{Bard}$ at equilibrium. Using their respective definitions, the current-overpotential equation from Bazant is

$$I = I_0 \mathrm{e}^{-(\frac{ne\eta)^2}{4k_BT\lambda})} \left(\mathrm{e}^{-(\alpha_{Bazant})*\frac{ne\eta}{k_BT}} - \mathrm{e}^{(1-\alpha_{Bazant})*\frac{ne\eta}{k_BT}}\right) \tag{55}$$

where the exchange current is

$$I_0 = nek_0 \mathrm{e}^{-\frac{\lambda}{4k_BT}} (\tilde{c}_O \tilde{c}_e^n)^{\frac{3-2\alpha_{Bazant}}{4}} \tilde{c}_R^{\frac{1+2\alpha_{Bazant}}{4}} \tag{56}$$

and the current-overpotential equation from Bard is

$$I = I_0 \mathrm{e}^{-\frac{F^2\eta\left(E_{eq}-E^{0'}\right)}{4\lambda RT}} \left[\frac{c_O^s}{c_O^b} \mathrm{e}^{-\frac{\alpha_{Bard}F\eta}{RT}} - \frac{c_R^s}{c_R^b} \mathrm{e}^{\frac{(1-\alpha_{Bard})F\eta}{RT}}\right] \tag{57}$$

$$I_0 = Fk_0 (c_O^b)^{1-\alpha_{Bard}} (c_R^b)^{\alpha_{Bard}} \tag{58}$$

For the important case of $E_{eq} = E^{0'}$, the current-overpotential equation for Marcus kinetics from Bard adopts the same form as for BV kinetics. Specifically, at $E_{eq} = E^{0'}$, the concentrations of the oxidized and reduced species are equal, and the system is at equilibrium at the formal potential. At near equilibrium, $\alpha_{Bazant} \approx \alpha_{Bard} \approx 0.5$.

Therefore, when η is small (meaning that the system is near equilibrium), α approaches 0.5 and Marcus kinetics approaches a limit where the rate form is the same as in BV kinetics.

4.5.1 Sharp-interface Models

The aforementioned models (i.e., empirical models and EKM) are either inherently limited to the treatment of interface reactions (i.e. EKM) or to models empirically fit to experimental data. However, as discussed previously, a foundation for the use of parabolic fits to experimental data can be justified by considering a simple diffusion-limited process. Based on these simple principles, utilitarian diffusion models have been proposed. Although they could in principle be used to simulate 3D systems–albeit by neglecting surface energies–, these models are typically used in one-dimensional simulation. The idea is to track the diffusion of species in the metal in consequence to oxidation reactions at the interface. In turn, the reaction rate at the interface naturally drives the motion of the corrosion front. Diffusion models cannot–by themselves–be used to predict morphological changes to the corrosion front or significant microstructure changes. However, they (i) can fully account for the evolution of the composition in the metal [216], (ii) can, importantly, account for the evolution of the composition of the salt, (iii) can utilize thermodynamic (i.e., MSTDB-TC for the salt and CALPHAD for the metal) and thermokinetic databases or experimentally reported redox potentials [216, 214]. For example, these models can leverage Nernst law and the Butler-Volmer equation [214] to estimate the driving force for oxidation as well as the reaction rates at interfaces. Critically, this opens the possibility of formally and rigorously linking the system's composition (salt and metal) to corrosion rate and motion of the corrosion front. We note that so far, none of the diffusion models proposed in the literature combine (i), (ii) and (iii). However, the formalism could in principle combine (i), (ii) and (iii) with relatively simple extensions. Further, diffusion models have the advantage of being particularly efficient from a numerical standpoint such that they can be used to explore the long-term evolution of corroded metals over time.

It should be noted that these types of diffusion models (if not extended beyond diffusion) will remain limited by (a) the data available in thermodynamic databases, (b) the complexities of reaction rates at real interfaces, and (c) the fact that diffusion through the solid often takes place along grain boundaries which may involve more complex rate forms than those considered by simple diffusion models [215].

Here, we illustrate the power and prospects of diffusion models by briefly synthesizing the model proposed in [143], which is one of the most advanced diffusion models proposed to date. In this study a simple homogenization model with a coupled thermodynamic-kinetic approach has been used to model the simultaneous corrosion, diffusion and Cr flux corresponding to the Cr loss estimated from measured (EDS) concentration profiles employed as a boundary condition at the alloy surface to simulate the corrosion process. While recognizing that the Cr corrosion occurs primarily along grain boundaries, the model simplifies the Cr depletion as being described simply by its total concentration at any given depth from the surface. The model relies on the formalism of Aagren and Larsson [217] to track the diffusion of Ni and Cr using a lattice frame. Importantly, the driving forces mediating the flux are provided via the use of a CALPHAD based thermodynamic database, TCNI8, to calculate the activities of the elements in the solid. The diffusion constants were obtained through homogenization methods. It is noted though that this one-dimensional diffusion model used the experimentally measured mass loss to set up flux boundary conditions (this is shown in Figure 19 b). As such this model does not predict the corrosion rate but rather the evolution of the composition of the underlying metal as corrosion proceeds. In practice, as discussed in the above, these types of frameworks, could in principle be extended to include the salt thermodynamics, to also predict diffusion in a salt, and to estimate the reaction rate at the interface as a function of time. In practice, such type of model has not been proposed.

The aforementioned diffusion model provides average element concentrations and phase fractions as a function of time and distance. For example, Figure 19a compares the measured and modeled Cr concentration profiles in Ni-7Cr, Ni-16Cr and Ni-24Cr alloy specimens after exposure in KCl–$MgCl_2$ eutectic salt for 2614 h at 800◦C. As shown, the work of Pillai et al. is in good agreement with the measured values. In practice, though, the experimentally reported corrosion profiles show significant grain boundary attack, which may be the cause of the visible dips in the Cr concentration profiles for Ni-16Cr and Ni-24Cr alloy in Figure 19 at around 20 μm deep into the alloy**.** Despite these limitations, the excellent match shown in Figure 19, spanning multiple NiCr compositions, clearly illustrates the power of integrating thermodynamic databases as an integral part of the computational workflow.

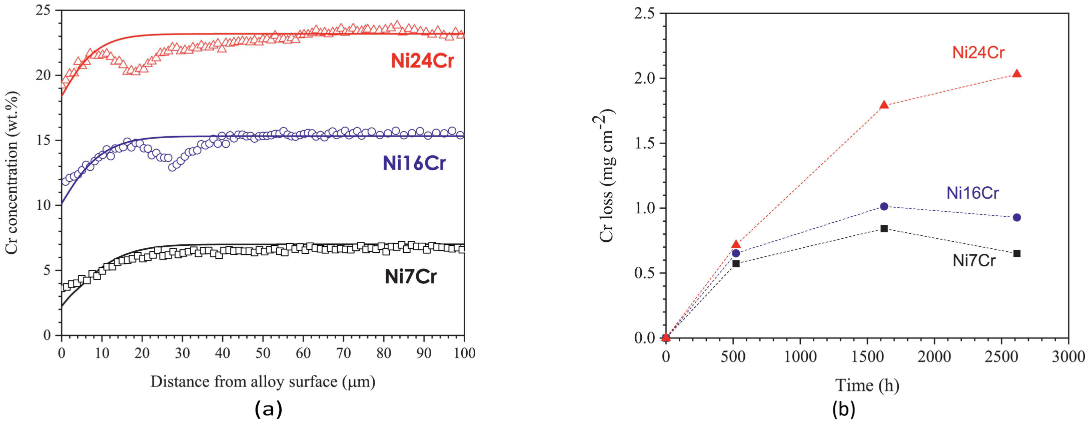

(a) (b)

Figure 19: Experimental and computational analysis of Ni-7Cr, Ni-16Cr and Ni-24Cr in purified binary KCl– MgCl2 salt at 800◦C, taken from [143]. (a) is a comparison between measured (symbols) and calculated Cr concentration profiles (lines) in the alloy specimens after exposure for 2614 h; (b) is the Cr loss estimated from measured Cr concentration profiles (average of profiles measured at 3 locations) in the alloy specimens after exposure for 522 h, 1625 h and 2614 h in the salts.

4.5.2 Diffuse-interface Models

The aforementioned models are particularly relevant for cases in which the corrosion front remains mostly planar, or otherwise sufficiently described by approximating the compositions as simply varying as a function of depth. In practice, and as stated previously, the vast majority of SEM images reporting corrosion fronts, including those emanating from the original MSRE, show that typical corroded microstructure is often characterized as complex microstructures characterized by grain boundary attacks, voids or even bicontinuous structures. Further, as detailed previously, diffusion models to date have not yet been used and extended to consider diffusion in both the salt and the metal. Importantly, simple diffusion models typically discard the role of interface energy and of diffusion transverse to the interface on both corrosion kinetics and on the morphology of the corrosion front. As will be discussed in this section, these phenomena can be large drivers of complex evolution of microstructures. Specific focus is placed here on a critical assessment of phase-field models, which treat the interface as a region where all variables (such as concentration) vary continuously, as explained further below. We note that the literature proposes several types of phase-field modeling approaches tailored to address different types of problems (e.g. formation of bicontinuous structures, mass loss over extended periods of time). For interested readers, a thorough and detailed presentation of the different phase-field formalisms is presented in Appendix C. Here, focus is placed on recalling the basic principles behind phase-field models and in discussing applications of phase-field models. Specifically, two use cases are presented. First a phase-field model, using a relatively thick diffusive interface is used to predict corrosion rates, mass loss, and motion, of a planar corrosion front, while leveraging MSTDB-TC to compute driving forces for corrosion. Second, a multi-phase-field model using a thinner description of the interface is presented. This model pays particular attention to the role of diffusion at interfaces such as the solid-liquid interface and along grain boundaries. This example illustrates how phase-field model can be used to address the critical problem of grain boundaries attacks.

Overall, phase-field models resolve the composition and phase (i.e., salt, solid) fields over complex volumes. In comparison to diffusion models, they typically treat diffusion in both solid and liquid phases and fully account for the effect of surface energy of the microstructure. They can leverage thermodynamic databases in the salt and in the metal to relate composition to both corrosion rates and morphology of the corrosion front. However, similarly to other models, they are limited by our lack of knowledge of the link between the structure of the electric double layer and salt composition, which pragmatically translates into the need for fitting parameters for the electron transfer rates at interfaces. Further, the models are typically far more computationally onerous than diffusion models. However, most phase-field codes are parallelized thereby enabling their use for long term simulations when the interfaces are quite diffuse. In contrast, models finely resolving transports transversely to the interface or along grain boundaries (whereby species transport can be exceedingly fast) are typically limited to simulating small volumes (i.e. ~200nm^2) over short periods of time (i.e. microseconds). As will be discussed later in the document, surrogate models can be leveraged to accelerate these simulations. Here below we first recall the foundations of phase-field models.

Sharp-interface models impose a mathematical difficulty of tracking the interface location or applying the adaptivity of the shrinking mesh due to phase transformation. In contrast, the diffuse-interface approach represents the microstructural features such as grains and phases using spatially-varying non-conserved variable fields, therefore can account for interfacial or grain boundary movements. Figure 20 illustrates the differences between diffuse-interface and sharp-interface models. Diffuse-interface models use a continuous field variable, typically one within one phase/grain and zero in the adjacent phases/grains with a smooth transition in-between, whereas the quantities associated with the sharp-interface models are discontinuous across the interface. Among the diffuse-interface modeling techniques, the phase-field method (PFM) is a powerful and widely recognized tool and very popular for simulating processes at the mesoscale level. The range of applicability is growing quickly, because of increasing computer power, among other reasons. Besides solidification [149] and solid-state phase transformations [150], PFM is applied for simulating grain growth [151], dislocation dynamics [152, 153], crack propagation [154], and solid-state sintering [155]. Most relevant to the current review topic is electrochemical phase-field modeling, which is a challenging area due to the large driving force and small-time scale frequently encountered in electrochemical problems.

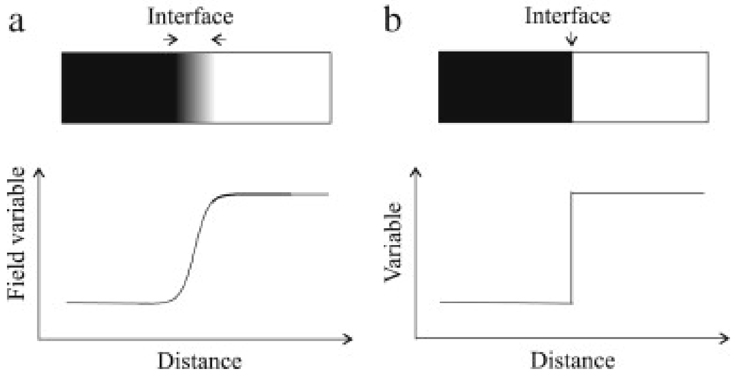

Figure 20: (a) Diffuse-interface model: properties evolve continuously between their equilibrium values in the neighboring grains. (b) Sharp-interface model: properties are discontinuous at the interface [156].

Several distinct PFM have been formulated over the years that differ in the variables being solved, assumptions being made, and diffuse interface being treated. In PFM, the interface is treated as diffuse with a finite width, and a continuous variable is used to represent the local phase fraction as a function of distance across that finite width. For a simple PFM considering an interface between two phases, the phase variable will range between values of 0 and 1. In this case, the phase value will vary between 0 and 1 continuously across the diffuse interface: this introduction of continuity across the interface is the main benefit of phase-field models. By utilizing the phase-field variable's value as an additional dimension, and including it in differential equations, those equations become more easily solvable (both analytically and computationally) relative to a scenario where the separation between the phases is treated as a discontinuous step, as discontinuities present challenges for solving many differential equations (see Figure 20). Further phase-field models also simultaneously track the evolution of the system composition locally by adoption of the Cahn-Hilliard framework. In general, the molar fraction of each component is represented as a conservative field variable $x_i (i = 1,2, \dots N)$, where i denotes the species and N is the total number of species in the system. The molar fractions of all components sum to unity: $\sum_{i=1}^{N} x_i = 1$. The phase-fields of the grains/phases are represented by non-conserved field variables $\xi_\alpha (\alpha = 1,2, \dots P)$, where α denotes the grain/phase and P is the total number of grains/phases and $\sum_{\alpha=1}^{P} \xi_\alpha = 1$.

Many classes of PFM approaches have been proposed throughout the literature; the distinct signatures of each class of model are briefly summarized below. The reader is referred to Appendix C for a more comprehensive discussion. In the Kim-Kim-Suzuki (KKS) model [157], the molar fraction of each species i in phase α ($x_{i,\alpha}$) is solved from the quasi-equilibrium condition and mass conservation condition (refer to Ref. [157] for derivations and details). The KKS model describes diffuse interfaces by imposing a local quasi-equilibrium condition: the diffusional potentials of all species are constrained to be equal between coexisting phases at each point within the interface ($\tilde{\mu}_{i,\alpha} = \tilde{\mu}_{i,\beta}$). This partitioning of compositions ensures the interfacial energy is decoupled from the bulk thermodynamic driving forces, thereby preserving a consistently defined interfacial energy. Computationally, this condition is enforced locally throughout the domain by solving for phase compositions $x_{i,\alpha}$ as field variables, although only the composition corresponding to the locally dominant phase(s) holds direct physical meaning. For systems with P phases and N species, this necessitates solving $(P-1)(N-1)$ local equilibrium equations, which can be computationally expensive. This approach contrasts with other multi-phase-field methodologies, such as grand potential (GP) [158] based models or the Wheeler-Boettinger-McFadden (WBM) formulation [159], which employ different strategies for handling multiple phases and components. In GP models, the quasi-equilibrium condition is implicitly satisfied through the direct solution of the diffusional potential fields ($\tilde{\mu}_i$), contrasting with the KKS approach of solving for phase compositions ($x_{i,\alpha}$). This typically yields a reduction in computational expense relative to KKS models, especially for systems with high degree of freedom. A critical prerequisite for GP models is the invertibility of the phase electrochemical free energy functions, $f_\alpha(\{x_i\},\{\xi_\alpha\})$, such that an explicit functional relationship $x_{i,\alpha}(\mu_{i,\alpha})$ exists. In WBM-type models, single composition fields (x_i) replace the phase-specific compositions ($x_{i,\alpha}$) used in KKS models. The local free energy density is formulated as an interpolation of the bulk free energy functions of the constituent phase, evaluated at the common composition x_i. While this results in a simpler formulation compared to KKS and GP-based models, a known artifact is that the bulk energy contributes to the calculated interfacial energy. This spurious contribution can be mitigated by using a small interfacial width parameter.

Here the general form of electrochemical PFM is presented. Field variables evolved with time and space to reduce the total free energy of the system $\mathcal{F}$, represented by a Ginzburg-Landau type functional:

$$\mathcal{F}(\{x_i\},\{\xi_\alpha\},\phi) = \int_V f_{chem}(\{x_i\},\{\xi_\alpha\}) + f_{elec}(\{x_i\},\{\xi_\alpha\},\phi) + f_{intf}(\{\xi_\alpha\}) + f_{grad}(\{x_i\}) \tag{59}$$

where ϕ is the electrostatic potential field variable, and f_{chem} is the local chemical free energy density written as the sum of the weighted bulk chemical energy of grains/phases present:

$$f_{chem}(\{x_i\},\{\xi_\alpha\}) = \sum_{\alpha=1}^{P} h_\alpha(\{\xi_\alpha\}) f_\alpha(\{x_i\},\{\xi_\alpha\}), \tag{60}$$

where $h_\alpha(\{\xi_\alpha\})$ is the interpolation function of phase α, and ideally $\sum_{\alpha=1}^{P} h_\alpha(\{\xi_\alpha\}) = 1$. $f_\alpha(\{x_i\},\{\xi_\alpha\})$ is the local chemical energy density of phase α, and it depends strongly on the chosen thermodynamic model (e.g., simple polynomial, regular solution) and the PFM flavor. $f_{elec}(\{x_i\},\{\xi_\alpha\},\phi)$ is the local electrostatic energy density, of which the specific form depends on the electrochemical assumptions discussed in Section 4.4.2.2. The local energy density f_{chem} and f_{elec} dictate phase stability and equilibrium compositions. The interfacial energy density,

$f_{intf}(\{\xi_\alpha\})$, establishes a diffuse interface between phases, governing its equilibrium thickness and specific energy. It typically consists of two main components: a local potential (such as a double-well or double-obstacle function for the two-phase interfaces (Steinbach 2009)) that energetically favors the distinct bulk phases over mixed states, and a gradient energy term, $\sum_{\alpha=1}^{P} \frac{\kappa_{\xi,\alpha}}{2} |\nabla \xi_\alpha|^2$, which penalizes sharp spatial variations in the phase-fields, and $\kappa_{\xi,\alpha}$ is the gradient energy coefficient of phase α. Asymptotic analysis in the sharp-interface limit provides a rigorous link between the parameters in f_{intf} and the physical interface properties [161]. An optional gradient term for concentration is:

$$f_{grad}(\{x_i\}) = \sum_{i=1}^{N} \frac{\kappa_{x,i}}{2} |\nabla x_i|^2 \tag{61}$$

which is sometimes needed to create a smooth interface for the composition variables such as in the WBM-type models; KKS and GP-type models generally do not contain $f_{grad}(\{x_i\})$ because the interfacial composition variables are already partitioned based on the quasi-equilibrium condition.

The phase and composition variables are typically solved by evolving with time and space to minimize the total free energy $\mathcal{F}$. The evolution of the $N-1$ independent conserved x_i is governed by the Cahn-Hilliard equation [162]

$$\frac{\partial x_i}{\partial t} = -\nabla \cdot \mathbf{J}_\mathrm{i} = \nabla \cdot \sum_{j=1}^{N-1} \left[M_{ij}(\{x_i\},\{\xi_\alpha\}) \nabla \tilde{\tilde{\mu}}_j \right] = \nabla \cdot \sum_{j=1}^{N-1} \left[M_{ij}(\{x_i\},\{\xi_\alpha\}) \nabla \frac{\delta \mathcal{F}(\{x_i\},\{\xi_\alpha\},\phi)}{\delta x_j} \right] \tag{62}$$

where $\mathrm{J_I}$ is the flux of species i and usually $M_{ij}(\{x_i\},\{\xi_\alpha\}) = \sum_\alpha h_\alpha(\{\xi_\alpha\}) M_{ij,\alpha}(\{x_i\})$, $M_{ij,\alpha}$ is the mobility of phase α for interdiffusion in a volume fixed frame [163] and related to diffusivity, and $\tilde{\tilde{\mu}}_j$ is the diffusional electrochemical potential. Equation (82) describes diffusion driven by gradients in $\tilde{\tilde{\mu}}_j$. It is important to note that chemical potentials are computed from the use of simple chemical models or can be extracted from thermodynamic databases. Recall, however, that the complexity of the MSTDB-TC requires particular attention to extract unique and meaningful values of the chemical potential of each species. The evolution of phase-field (interface motion, phase transformation) is governed by the Allen-Cahn equation [164]

$$\frac{\partial \xi_\alpha}{\partial t} = -M_\xi \frac{\delta \mathcal{F}(\{x_i\},\{\xi_\alpha\},\phi)}{\delta \xi_\alpha} \tag{63}$$

where M_ξ is the interfacial mobility, and $\frac{\delta \mathcal{F}}{\delta \xi_\alpha}$ represents the thermodynamic driving force. Appendix C provides additional details related to the distinction between different phase-field models, particularly in what concerns the treatment of the electrostatic charges. The following briefly illustrates two distinct applications of the PFM, using different formulations. In a first category of PFM examples, Bhave et al. have contributed two key PFM studies on the molten salt corrosion of Ni-Cr alloys in FLiBe salt [169, 184], both employing the electrochemical assumptions and formulations detailed in Appendix C. In the first study, which lays out the foundation for a PFM model for molten salt corrosion, a few ions can dissolve in the salt (i.e., Ni and Cr) and impurities, specifically HF, are assumed to drive the corrosion process. In contrast all other species in the salt are assumed not to follow any redox reaction. The solid is treated as having grain boundaries with the possibility for diffusion rates for Cr along these grain boundaries differing from its bulk diffusion rate. Further, electroneutrality is imposed in the system. The chemical potential of Ni and Cr are extracted from CALPHAD. The model is then applied in the context of 1D, 2D and 3D simulations. The driving forces for the reactions to take place (i.e., the redox potential) are directly extracted from experimental data and the overall effect of Cr and Ni in the salt is modeled in the dilute limit. The interface width is relatively broad, on the order of a micrometer. Following calibration of the model, a series of simulations were performed and compared to experimental data. The results of these simulations are shown in Figure 21. As shown in Figure 21 (a), 2D simulations clearly demonstrate that the total mass loss in Ni-Cr alloys is primarily manifested as Cr depletion concentrated along grain boundaries (GBs), and within small grains near the surface, aligning with the corrosion model depicted in Figure 17(b2). A 1D sensitivity analysis identified the Cr diffusion coefficient as the most influential parameter on predicted Cr mass loss. Furthermore, their 3D model predicted a mass loss of approximately 0.45 mg/cm^2 for Ni-5Cr alloy in FLiBe salt after 1000 h, achieving an average Root Mean Square Error (RMSE) of 29 % when compared to experimental data [13]. Note that the effect of grain boundary character is not considered in these studies: further comparison between a 1D and higher dimensions study clearly demonstrate that the role of grain boundaries should be considered to acceptably predict Cr corrosion kinetics for this system.

As shown, these types of phase-field models, as opposed to the simpler sharp-interface models proposed in the literature, can simultaneously capture mass loss and change in local compositions mediated by grain boundary transport - note that these could be extended to emulate grain boundary effects. Further, as with the 1D semi-empirical sharp-interface models, these models could also leverage the MSTDB-TC databases to start addressing the role of impurities once those are included in the databases. This exemplary simulation is the first to consider the effects of impurities in the salt. Further, we note that corrosion experiments and simulations of extended periods of time were performed. Despite these encouraging results, this model remains limited in the treatment of the salt (dilute limit) and does not account for dynamic grain boundaries (such as migration of the grain boundaries), and largely relies on experimental data for calibration, cannot account for Kirkendall voids etc. However, such frameworks could be extended to, in the future fully account for these effects.

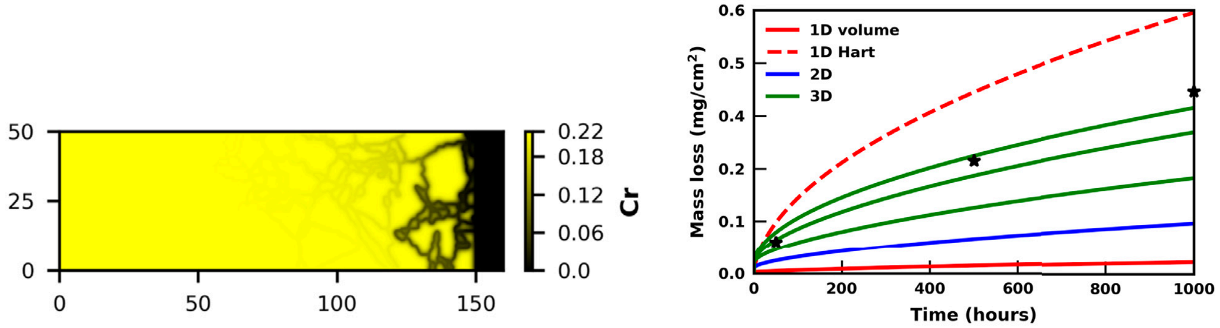

Figure 21: (a) Predicted Cr concentration from 2D simulations of moltens salt corrosion after 1000 h of corrosion in Ni-20Cr. The Cr depletion is concentrated along GBs and the small grains close to the surface, (b) predicted and experimentally measured (asterisks) mass loss as a function of time for 1D, 2D and 3D simulations. Multiple 3D simulations are performed showing the impact of microstructure variability.

Building on this foundation, a subsequent study [184] utilized the 2D phase-field model from previous work [169] to explore the effectiveness of Ni coatings in mitigating corrosion of Ni-Cr alloys in FLiBe. This research aimed to elucidate the significant variability reported in the literature regarding the performance of pure Ni coatings. The simulations captured a tenfold decrease in mass loss for a Ni-20Cr alloy at 700 °C after 1000 hours with a Ni coating. Further, this study was used to propose design routes. For example, the study showed that increasing coating grain size reduced both mass loss and corrosion depth by decreasing the density of fast grain boundary diffusion paths for Cr to reach the salt. Similarly, increasing the underlying alloy grain size was predicted to decrease mass loss (due to less total grain boundary paths for Cr depletion) but could be accompanied by an increase in corrosion depth (as depletion along fewer, larger grain boundaries could penetrate further). Finally, it was found that increasing coating thickness led to a rapid decrease in mass loss and diminished the impact of both alloy and coating grain size, suggesting that controlling coating grain size becomes less critical with thicker coatings.

In a second category of PFM examples, we illustrate another body of work relying on PFM to model salt corrosion [218,219]. As opposed to the previous example, the model we look at next proposes to use a significantly finer description of the diffuse-interface (i.e., 2nm) and departs from a simple ideal mixing model for metal dissolution in the salt. Further, this model leverages a multiphase-field approach allowing for grain boundaries to migrate. While the work of Bieberdorf et al. is not concerned with a specific salt and metal, it aims at proposing a rationale for the diversity of corrosion profiles seen experimentally. As discussed previously, these corroded morphologies can range from planar corrosion profiles to bicontinuous structures. We note that this model was deployed to study both liquid metal dealloying and dealloying corrosion. For this model, the constraint was applied that grain boundaries in contact with the salt maintain an equilibrium configuration. In this approach, grain boundaries play two important roles. They act as rapid diffusion pathways for Cr and Ni and also migrate to preserve equilibrium. In this body of work, the non-ideality of mixing at the solid-liquid interfaces can drive an instability - specifically a spinodal decomposition - leading to complex morphologies of the corrosion front. This is illustrated in the 3D results presented in Figure 22 (a-c) in which dealloying corrosion was simulated as a function of alloy composition. In these examples a binary A-B alloy containing a less noble species, B, is exposed to a salt, C. As shown in Figure 22, these types of formalisms clearly demonstrate the PFM can (i) capture the linkage between composition and parting limit,

(ii) universally rationalize the difference in observed corrosion front including the formation of bicontinuous structures, (iii) predict the role of grain boundary migration on corrosion.

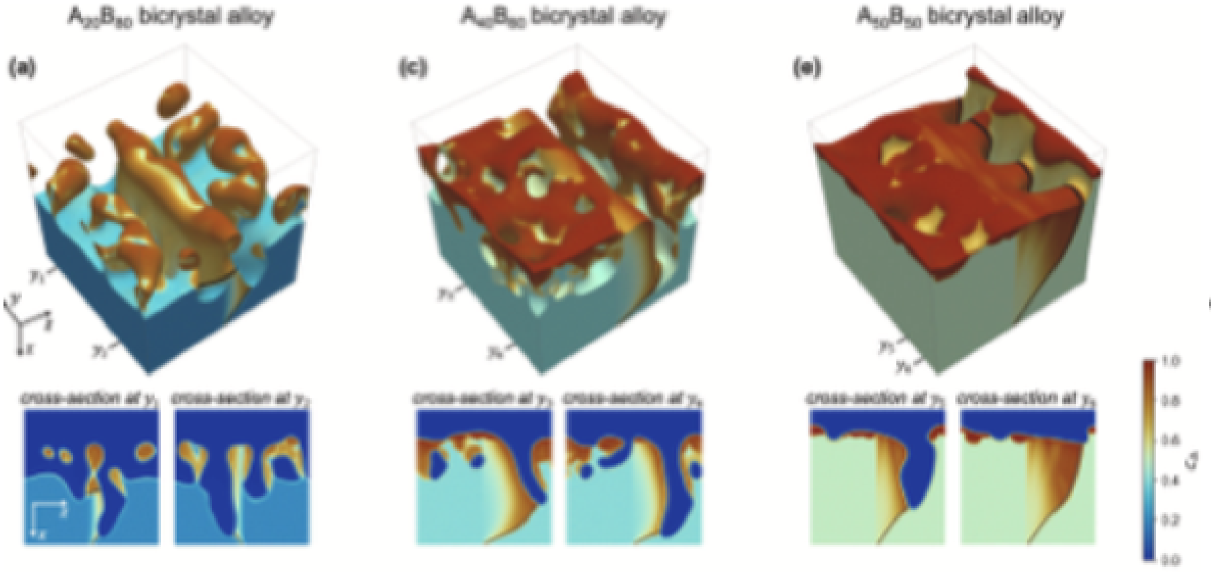

Figure 22: Multi-phase-field dealloying simulations of bicrystal base alloys with varying initial composition. (a) 3D and (b) 2D simulations of $A_{20}B_{80}$ base alloy after 2.3 s and 29 s, respectively. (The - cross-sections in the middle row correspond to the markers from each 3D view in the top row. Each image is colored by the local concentration of species A, and a dark gray band has been added to mark the location of the grain boundary. The liquid phase only illustrated in the middle and bottom rows. [218,219]

4.5.3 Models Using Kinetic Monte Carlo Based Methods (KMC)

Atomic scale Kinetic Monte Carlo (KMC) methods can simulate the effect of a collection of unit processes (atomic jumps, reactions) on corrosion. These types of simulations have typically been used to simulate particularly small volumes (under 100 nm lengthscales) over short periods of time (up to microseconds). These methods can be extended to greater length and timescales, but most KMC studies on corrosion have not been used to simulate corrosion over extended periods of time. The method may help alleviate epistemic gaps associated with interfacial reactions and could be used to formulate inputs (or direct usage) in multi-scale modeling.

Lattice Kinetic Monte Carlo methods are numerous and have historically been proposed to simulate microstructure evolution processes in which an accurate quantification of the local atomic scale energy landscape change associated with reaction or diffusion unit processes are necessary. The basic principle of KMC is to evolve the state of a system by stochastic processes with random number selection to determine the process and/or time evolution [228]. In a typical implementation, random numbers are used to select both the time step and the next event to occur, based on the expected average rates of the different possible events [229]. For chemical reactions, the average rates of the different possible events are dictated, in part, by the activation barriers associated with each process. Those activation energy based rates are typically obtained by prior knowledge, simple predictive models, or density functional theory using minimum energy pathway search methods [230, 231]. KMC methods allow circumventing the problems associated with solving complex coupled systems of equations and advantageously are stochastic in nature; thereby able to capture rare events. While KMC has not yet been used to simulate molten salt corrosion, it has been applied with success to simulate aqueous corrosion and dealloying in several materials. As such it is a particularly relevant technique to consider.

In KMC, each step of the simulation follows a specific protocol, and one implementation will be described here, though other algorithms exist [228]. In the implementation described here, all evolutions of the system and their corresponding transition rates k_i are listed, a time increment Δt is computed based on the sum of these rates, and one event is randomly selected using a weighting based on the relative rates of each possible event, which can thus be expressed as a distribution of probability ($\{P_j\}_{j\in M}$). The next step begins with an update of the event list and the corresponding event rates in response to the change in the system. Only the rates of events which would occur near the previously modified site need to be recalculated. Here, the evolutions are local (i.e., one site at a time) whereby an atom or ion can either move (diffusion) or get involved in a reaction (e.g., dissolution). The time increment and probabilistic distribution for event selection are given by:

$$\Delta t = \frac{1}{\sum_{i=1}^{M} k_i} \tag{64}$$

$$P_j = \frac{k_j}{\sum_{i=1}^{M} k_i} \tag{65}$$

This KMC framework has been used extensively to model the dealloying of metallic $AuAg$ electrodes in KNO_3 under an applied potential. Indeed, by applying an external potential to an AuAg electrode, experimentalists have observed morphology changes in corrosion depending on whether the potential is above or below a composition-dependent critical potential, denoted E_c. The model successfully describes mechanisms responsible for the formation (or absence) of porous morphologies, particularly spinodal decomposition at the interface due to surface diffusion of Au atoms [126]. The simulation used a 256×256 grid with a depth of 500 layers representing a (111)-oriented terrace of a face-centered cubic (fcc) lattice. Only atoms neighboring a vacant site are allowed to evolve, that is, atoms with a coordination number less than or equal to 11. This greatly reduces the system's complexity. The energy barrier for diffusion was calculated as the sum of the bond energies with surrounding atoms. A constant interaction energy E_b was used for $Au-Au$, $Ag-Ag$, and $Au-Ag$ bonds, while interactions with vacant sites were set to zero. Although a more precise calculation would involve the difference in energy between the initial and transition states, the simplified model yielded comparable results. Dissolution used the same energy barrier as diffusion but is modified to account for the potential energy of the electrode.

$$k_n^{\text{diff}} = \nu_D \exp\left(-\frac{nE_b}{k_B T}\right) \tag{66}$$

$$k_n^{\mathrm{diss}} = \nu_E \exp\left(-\frac{nE_b - \phi}{k_B T}\right) \tag{67}$$

with ν_D denoting a frequency close to the Debye frequency, ν_E a frequency for dissolution including vibrational contributions and an exponential of the entropy difference caused by dissolution, n the coordination number of the atom and ϕ the energy shifts proportional to the applied overpotential.

This model led to dealloying morphologies observed depending on overpotential applied and alloy composition. Yet, these simulations neglected the dynamics of the surrounding liquid electrolyte and bulk atoms were assumed immobile. Adding these two missing dynamics components into the KMC algorithm would drastically increase the computational time. Especially due to the high mobility of liquid particles, the simulation would be overwhelmed by highly probable diffusion events in the liquid phase. Indeed, the number of simulation steps is in $\mathcal{O}\left(\frac{\Delta T}{\Delta t}\right)$ e.g. $\mathcal{O}(\Delta T \sum_{i=1}^{M} k_i)$ with ΔT the simulation duration. Only considering interface diffusion events we get $\mathcal{O}\left(\Delta T \sum_{i=1}^{M} k_{n_i}^{diff}\right) \approx \mathcal{O}\left(\Delta T. N_x N_y. k^{diff}\right)$ with N_x and N_y the total number of atoms on the lattice along axis x and y assuming an interface in the (x, y) plane, and k^{diff} an average interface atomistic diffusion rate. Simulation of corrosion for a $1\mu m^2$ interface during $1\mu s$ would therefore take 10^9 steps which is on the order of magnitude of what was computed in [126]. The problem of high frequency events in KMC is also known as KMC stiffness, and algorithms exist for overcoming KMC stiffness [232-234], though such algorithms were not used in the above study.

A modified model introducing electrolyte dynamics into a KMC model was proposed [144]. Liquid molecules (water, cations and anions) were added to the fcc lattice, with their dynamics evolved via a non-stochastic processes at each step, thereby as a modified KMC simulation. At each time step, the simulation performed local displacements of the liquid molecules within their coordination shell, governed by strict rules to preserve electroneutrality and ion aggregation. Vacant lattice sites represented water molecules, which were not explicitly simulated. For each dissolution event of Ag , the reaction product was a cation, Ag^+. This model managed to reproduce dealloyed porous morphology and more importantly gave different results depending on the electrolyte composition.

In addition to KMC, studies have used Metropolis Monte Carlo (MMC) algorithms for corrosion, especially to accelerate the system's approach to equilibrium configurations. One version includes using a random number to 'propose' an event, followed by adding a second random selection step after an event is proposed. With this second random number, the value of a variable, U is drawn from [0,1], and a transition from state C to C' is accepted only if $U > \exp(-\beta[E(C') - E(C)])$. Here, $\beta = \frac{1}{k_B T}$ and $E(C)$ is the total energy of the system in state C. This additional step accelerates convergence toward equilibrium. A variation of MMC has been used to simulate AuAg dealloying in the presence of vacancies and electrolyte molecules on an fcc lattice [145].

KMC and MMC have not been routinely applied to molten salt corrosion, but are already valuable tools in other corrosion domains. The advantage of KMC simulations [126] naturally avoiding the complex coupled equations of mean-field models naturally captures rare events, when KMC stiffness can be overcome and when the computational expense is not prohibitive. KMC simulations are computationally expensive: Models stated previously used on average 500×500×500 lattice grids, equivalent to roughly ten million atoms and physical sizes on the order of 100 nm. In most KMC simulations of corrosion, only interfacial phenomena are modeled. Including bulk diffusion or simulating advanced porosity structures drastically increases the computational power needed to achieve any desired simulation time. Additionally, it is challenging (and sometimes impossible) to achieve computational speedups for KMC simply through use of more powerful computing resources. Moreover, modeling a more realistic interfacial dynamic remains challenging. The limited studies so far rely on strong approximations—such as representing liquid species on the same lattice as solids and simplifying their mobility. A similar difficulty would arise when attempting to model grain boundaries. Additionally, KMC models stated here all used harmonic state transition theory or even simpler approximations to obtain the activation energies used in the atomistic transition rates. However, the accuracy of harmonic transition state theory and simpler approximations may introduce some error, especially at high temperatures. Finally, performing KMC for molten salts corrosion would require a vast database of atomic energy barriers as the number of species in the salt increases as suggested by a 2019-Oak Ridge report [146]. Today, for state-of-the-art chemical accuracy, many DFT simulations would be necessary to populate such a database. The computational expense of populating the database (or using on the-fly calculations) can be reduced using simplified or surrogate models. While atom-scale KMC simulations can provide meaningful chemical mechanistic knowledge and chemical kinetics knowledge for corrosion in molten salts, this methodology has currently not been widely applied to molten salts corrosion.

4.5.4 Lattice Gas Model

In addition to the methods described above, there are also lattice gas models which theoretically could yield an accurate understanding of the charge distribution near salt-metal interface and of their effects on transport of charged species. One significant limitation of lattice gas mean-field approaches is their computational cost: the typical spatial discretization step is on the order of 3 Å, making simulations expensive in both time and memory. Additionally, since the method is lattice-based, it becomes very difficult to accurately model amorphous phases or complex geometries like grain boundaries, where the regular lattice assumption breaks down. While lattice gas mean-field models have been employed to simulate electrochemical cells, they have not been applied to the study of corrosion in molten salts, yet. Mean-field methods have been widely used to model phase transitions in solids and, more recently, to model spinodal decomposition of an alloy from the interface to bulk [147], as well as electrochemical cells and the growth of metallic dendrites by lithium reduction in lithium-ion batteries [148]. These models rely on the idea of averaging the interactions of a particle with its environment: the particle evolves in a mean-field. A detailed presentation of lattice gas models is presented in Appendix D.

4.6 Surrogate models

Surrogate modeling approaches involve using models that do not have any physical meaning, but which can reproduce the physical behavior at reduced computational cost once the surrogate model has been trained on a more meaningful model. Surrogate models have the prospects of potentially addressing the limitations of both empirical models and of phase-field modeling, because they retain the physically realistic behavior of the more meaningful model they were trained on while also achieving the computational cheapness that is normally associated with empirical models. For the past decade, the materials science community has made significant progress in the development of new methods to derive surrogate models. Regardless of the approach pursued, the idea of surrogate models is to derive numerically inexpensive models that emulate predictions from either costly or limited models. Overall, several different types of surrogates modeling approaches have been explored by the community. In the specific case of molten salt corrosion, efforts have been more limited. These include polynomial chaos expansion models, convolution neural networks, graph neural networks, random forest models, genetic symbolic regression models (which rely on machine learning and acyclic graphs to derive analytical models) and similar approaches such as Gaussian processes.

To date, in the specific case of corrosion and dealloying process, we note two important bodies of work. First, in [129], a team first exposed several metals (i.e. Nb, Ta, 316SS, Zr2, Zr4, HT9, Hastelloy N, W and T91) to LiCl-KCl and LiBr-KBr molten salts for 24hours. Then they used Gaussian process regression in combination with an ensemble averaging technique to build a numerical efficient predictor for the kinetics of corrosion for the different metals. The model was found to lead to quite accurate estimates of relevance to engineering length and time scales. These types of surrogate modeling approaches could, in the future, supplant or be used to improve empirical laws. Critically though, they will rely on significant data gathering, since surrogate models must always be trained, and require adequate training data to achieve sufficient accuracy.

Second, we note the work in Ref. [187], largely motivated by the pioneering study in Ref. [188], in which U-Shaped Adaptive Fourier Neural Operators (U-AFNO) were used to develop a surrogate model for high-fidelity and high-resolution phase-field simulations. Remarkably, the U-AFNO surrogate was shown to be able to replicate the evolution of the composition, corrosion front and morphology over time with a speed up factor reaching 11200. This is shown in Figure 23 in which a comparison of the evolution of composition and dealloying corrosion front as predicted by phase-field modeling and by the surrogate model is presented as a function of simulation time. As shown, the surrogate can match with high precision the outputs from the far more numerically costly simulations. This promising body of work could in the future be leveraged to perform simulations over time scales commensurate with service conditions. However, it must be noted that most surrogate models can only serve the purpose of interpolating between point or known states and cannot be used to reliably extrapolate/discover unseen states. For example, in Figure 23 below, the surrogate model would not be able to capture any bifurcation in the evolution of the system (e.g. change of corrosion mode to planar corrosion).

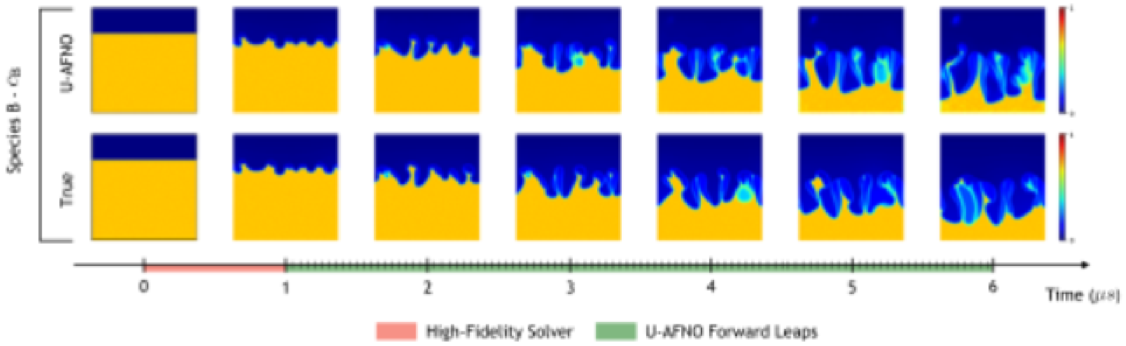

Figure 23: Comparison between predict dealloying corrosion profiles predicted via phase [188].

4.7 Summary and discussion of necessary steps to predicting molten salt corrosion over extended exposures as a function of salt composition and fission products

As per the presentation of the various modeling and simulations approaches discussed previously, over the past decade significant efforts have been made to introduce computational models that can predict mass loss, salt penetration depth, and morphologies of the corrosion front as a function of both the composition of the metals and of the composition of the salt (including impurities). To date, there is not a universal model that can predict all chemical and physical features of corrosion, simultaneously. We also note that, to date, no effort has been placed on predicting the rate of generation and depth of Kirkendall voids for the context of molten salt corrosion of metal alloys. Further, all modeling work pertaining to corrosion remains limited in its ability to predict reaction rates at interfaces. From a fundamental standpoint, a net reaction rate is the product of two factors; a thermodynamic factor which dictates driving force for a reaction to take place, and a kinetic factor which quantifies the frequency at which events are attempted. If the net reaction rate is considered to depend on these two factors, the reactant concentration, the mechanism, and the energy barrier are within the kinetic factor. Both the reactant concentration and the product concentration will be in the thermodynamic factor. Our lack of understanding of the linkage between composition of the metal, and of the salt and the electric double layer structure largely limits our ability to infer reaction rates at interfaces. Pragmatically, this translates into a need to fit models to experimental data to capture the rate of corrosion at the salt-metal interface. Electrochemical methods such as cyclic voltammetry or simple short term corrosion tests can be among the methods used to generate experimental calibration data. Further, as stated previously, it has been shown that thermodynamic and thermo-kinetic databases can be used to inform models (i.e. chemical potentials, intrinsic diffusion), thereby clearly demonstrating the potential for corrosion models to relate salt and composition to corrosion rates, corrosion front morphologies etc. However, gaps in thermodynamic databases, which have not yet addressed the effects of impurities and fission products need first to be filled to realize the potential of corrosion models. In lieu of thermodynamic data, models can leverage experimental tests reporting redox potentials. However, the question of data quality emerges in addition to the need to assess the evolution of species and their chemical potentials in non-dilute conditions. This is key because, as discussed previously, instabilities leading to a complex corrosion front are suspected to emerge from these conditions (e.g., concentrated dissolved Cr in the salt). Further, to date, given the recent emergence of models for molten salt corrosion, limited thoughts have been given to addressing the key question of the types and minimum sets of experiments (i.e., duration, conditions) necessary to develop models that can be used to rapidly extrapolate the evolution of the corrosion front and composition of the metal. Additionally, there will continue to be challenges due to complex corrosion mechanisms, dynamic corrosion morphologies, and even potentially changes in the dominant mechanism of corrosion as a function of time. In what follows, we briefly recall the state-of-the-art, gaps and potential extensions that could be made to develop models that could predict moltens salt corrosion over extended exposures as a function salt composition and fission products. This is summarized in Table 10.

Empirical models (i.e., linear/parabolic) and one-dimensional sharp-interface models [143] have been shown to reproduce experimental data (i.e., mass loss over time) quite well in scenarios in which the corrosion front is relatively planar and largely rate limited by diffusion in the metal. Further, their numerical cost is minimal such that these models are useful. However, while some of the most refined approaches establish linkages between the composition of the metal and corrosion rates, such is the case of the work of Pillai et al. [143], to date, they need to be informed by experiments to assess the reaction rates at the interface. Thus, models would need to be extended to include the salt state to be deployed even on related salt/metal systems. In addition, central to simple sharp-interface diffusion-based models lies the need to introduce effective diffusivities which are key to emulating the role of grain boundaries on corrosion. This has been shown to play an important role in several experiments [186]. Despite their simplicity and limitations, sharp-interface models, particularly one-dimensional ones which are particularly efficient and simple from a numerical standpoint, could be the foundation to develop simple models that predict corrosion over extended periods of time as a function of composition. Necessary extensions will have to consider connecting the driving force for corrosion to thermodynamic databases and devising a means to capture the effect of grain boundaries. We note that, as shown in the work of Bhave [169], existing homogenization models for grain boundary effects are insufficient. Further one-dimensional models would require extensions to consider/homogenize the response of the material when corrosion adopts a complex path (i.e. grain boundary attacks, bicontinuous structures). However, surrogate models could be used to this end, whereby simulations from PFM, which have been shown to be able to address, could be used to provide ground truth data which could be homogenized and simplified using surrogate models. These could operate either as standalone corrosion models or in combination with 1D sharp-interface model thereby providing ‘correction’ accounting from morphological effects. Such a hybrid approach is highly desirable as it would yield interpretable models. Naturally, this hinges upon necessary development in diffusion interface models.

Table 10: Summary of state-of-the-art associated with key models for molten salt corrosion

Model type	Ability to predict corrosion over thousands of hours	Connection with thermodynamic databases	Corrosion modes	Grain boundary effects	Kirkendall voids
1D Sharp-interface model [216]	Y	These models have been connected to databases for the metal but not for the salt. Such extension could be made	Limited to planar corrosion front. 3 D extensions and interaction of the effect of surface energy would be necessary	These models cannot accurately capture grain boundary effects. Those must be inferred by parameter choices	N
Phase-field model with diffusive interface [169]	Y	These models could also leverage both the MSTDB_TC and CALPHAD databases. Examples in the literature have thus far only considered use of CALPHAD	The model form proposed exclusively treated planar corrosion front but could be extended to capture other corrosion models	Rapid transport across grain boundaries can be modeled. The motion of grain boundary has not been modeled. However, the model could be extended to do so	N
Phase-field model [118,119,187,218,219]	N	These models could also leverage both the MSTDB_TV and CALPHAD databases. This has not been done	Can capture any corrosion mode	Both grain boundary transport and grain boundary motion are addressed	N

Indeed, diffusive interface models, relying on the use of PFM models are also fully compatible with thermodynamic databases and can thus already reproduce predictions from sharp-interface models. Further, phase-field models can predict both the role of grain boundaries as a fast diffusion path for dissolution/corrosion [184] and as drivers for microstructure instabilities, whereby the corrosion front advances far more rapidly into the metals [119]. Further, PFM can naturally capture the transition between planar corrosion profiles to parting [118]. However, like sharp-interface models, these models suffer from the fact they typically cannot directly, blindly, predict reaction rates at interfaces or fully describe the structure of the 'bilayer' near the interface. In other words, the reaction rate at the interface must be fit to experiments. Most critically, PFM models are typically costly from a numerical standpoint and thus require high performance computing resources. This typically motivates researchers to either use particularly diffusive interfaces (i.e., with an interface width exceeding 2µm) thus leading to loss of fidelity vis a vis atomic scale processes or to simulating particularly small unit volumes over short durations. However, these models have successfully been deployed to study the potential impact of impurities (e.g., HF) in salts and have proven to be able to predict corrosion over extended periods of time. The difficulty lies in the fact that, currently, predicting the evolution of complex morphological fronts (i.e., bicontinuous structures, salt penetration due to grain boundary motion) requires fine meshes (i.e., sub nm) thus limiting considerably the computational cost. Thus, PFM models overall either use a very diffusive interface and will not, in their current forms, necessarily capture morphological instabilities; or will use a narrow interface to capture those but then not be applicable to address corrosion over extended periods of time without being coupled to other modeling techniques. As discussed previously, surrogate models provide a rich research avenue as they have been proven to be able to accelerate simulations by several orders of magnitude. Further, surrogates can be used to homogenize and simplify 3D simulation outputs into datasets or models compatible with 1D sharp-interface models. It should finally be noted that, to date, none of these types of models have addressed the question of the formation of Kirkendall voids. This is largely due to our lack of formal consideration of vacancy transport and generation during corrosion.

In conclusion, with sustained support, the modeling community is rapidly making progress in addressing the challenge of predicting molten salt corrosion over extended periods of time. With the many important aspects of corrosion (mass loss, composition change in the interior), there may be a role for all approaches being currently developed, and it is likely that surrogate modeling/machine learning will be increasingly used to establish connections between advanced and simplified models; thereby improving the fidelity of numerically light models.

CONCLUSION

This technical letter report set out to: (i) assess the current state-of-knowledge on chloride-salt properties; (ii) review modeling techniques used to study molten-salt properties; and (iii) evaluate the maturity of models that predict corrosion of structural metals as a function of salt state. These three aims guided the structure of the work.

The evidence compiled here points to a clear, actionable picture. Chloride-based molten salt reactors are advancing quickly, yet the experimental and modeling base that underpins safe deployment is currently uneven—especially for actinide-bearing fuels and for conditions that, realistically, will include fission products, impurities, and irradiation. What is known is encouraging: thermodynamic frameworks and Gibbs energy minimizers built on MSTDB-TC/TP can already capture key driving forces for corrosion, and modern atomistic simulations reproduce many thermophysical trends with useful fidelity. The most consequential unknowns still cluster at the salt-metal interface. The electric double layer in molten salts, unlike in aqueous systems, is governed by strong ion correlations and layering: without a quantitative handle on that interfacial structure, rate laws must be fitted rather than predicted, constraining confidence in long-term forecasts.

The path forward that emerges from this report is integrative rather than incremental. First: expand and validate the property databases to cover impurities and fission products so corrosion driving forces and transport can be computed for service-relevant chemistries. Second: pair standardized, in-situ electroanalytical measurements with exposure tests to supply the interfacial kinetics that present models cannot derive from first principles. Third: couple scales use thermodynamic calculations to set boundary conditions, sharp-interface or 1D models for efficient lifetime predictions, and phase-field (and related) methods to resolve morphology, grain-boundary effects, and transitions between planar attack and dealloying. Surrogate and machine-learned interatomic potentials can bridge cost and coverage, turning high-fidelity simulations into practical tools.

Taken together, these steps convert today's partial understanding into a predictive framework: one that links evolving salt composition to redox state, transport, interfacial kinetics, and ultimately to measurable outcomes such as mass loss, penetration depth, and damage morphology. Such a framework—grounded in coordinated experiments and databases and accelerated by modern computation—will enable regulators and designers to make defensible decisions about materials, monitoring, and mitigation for chloride-salt MSRs, as they move from laboratory demonstrations to licensed operation.

Appendix A: The Modified Quasi Chemical Model

This model was developed to capture the short-range ordering (SRO) present in molten salts, a crucial feature that ideal or regular solution models fail to represent. MQM solutions come in different forms from simple to complex. Consider a liquid binary solution consisting of A and B atoms or molecules. The simplest scenario is that A and B are distributed over the sites of one quasi lattice. The following pair-exchange reaction is considered:

$$(A-A)+(B-B)=2(A-B) \tag{68}$$

where (*i* − *j*) represents a FNN pair. The non-configurational Gibbs energy change for the formation of 2 moles of (*A* − *B*) pairs is Δg_{AB}. The Gibbs energy of the solution is given by:

$$G=(n_A g^{\circ}{}_A+n_B g^{\circ}{}_B)-T\Delta \mathrm{S}^{\mathrm{config}}+\frac{n_{AB}}{2}\Delta g_{AB} \tag{69}$$

where n_A and n_B are the number of moles of *A* and *B* and n_{AB} is the number of moles of (*A*−*B*) pairs, $g^{\circ}{}_A$ and $g^{\circ}{}_B$ are the molar Gibbs energies of the pure components, and ΔS^{config} is the configurational entropy arising from the equilibrium distribution of atoms on the quasi lattice sites, which accounts for the non-randomness caused by differing bond energies of FNN pairs. ΔS^{config} is a function of the molar fraction of components and pairs, and coordination numbers. Δg_{AB} can be described using empirical parameters fitted to real systems and might be a function of temperature [99]. In the case of higher-order (many component) systems which often lack experimental data, their behaviors can be predicted without all subsystems being fully or even partially assessed. The un-modeled component(s) may simply be treated as mixing ideally within the solution description of the phase. Such predictions offer a reasonable estimate of the Gibbs energy relations in the absence of sufficient data for performing assessments of higher-order systems. For example, the pairwise interactions in pseudo-binary systems can be mathematically combined and extrapolated to predict the behavior of a pseudo-ternary system [61]. The extrapolation from binary systems uses either a symmetric or asymmetric formula: the symmetric formula applies when all components are treated in the same fashion, whereas the asymmetric formula is useful when one component is chemically different from the other components (e.g., S in S-Fe-Cu). The Gibbs energy of the higher-order solution is

$$G=\sum n_m g^{\circ}{}_m - T\Delta S^{config}+\sum_{m}\sum_{n>m} n_{mn}\frac{\Delta g_{mn}}{2} \tag{70}$$

where Δg_{mn} depends on the symmetric or asymmetric condition and empirical binary coefficients, which are obtained by optimization of binary experimental data. Composition-dependent coordination numbers were also introduced in this model; this provides greater flexibility and permits the composition and maximum SRO to be chosen independently in each binary subsystem [100].

In a molten salt solution, if the cation and anion exhibit a very high degree of SRO, such that the nearest-neighbor of cations are almost exclusively anions and vice versa, it is conceptually and mathematically simpler to treat the liquid solution as if it consisted of two distinct sublattices. A sublattice each for cations (A, B, …) and anions (X, Y, …) allows all combinations to be considered as quadruplets ($\frac{AB}{XY}$) consisting of all permutations of anions and cations [61]. Each quadruplet contains two SNN cations and two SNN anions. Additionally, the cations and anions are mutual FNNs, so both FNN and SNN can be treated simultaneously. Due to its complex form, the Gibbs energy expression for MQMQA is omitted here; the complete derivation and explicit form can be found in Ref. [102].

A small number of cation-cation or anion-anion nearest neighbors are treated within this two-sublattice model as substitutional defects. The ratio of the numbers of sites on the two sublattices vary with composition. Expressing the two-sublattice system as *(A, B, ...)/(X, Y, ...)* where *A, B* are cations and *X, Y* are anions, in the pair approximation, second nearest-neighbor (SNN) pairs are identified as cation pairs such as *A − X − A, A − X − B*, etc, and anion pairs such as *X − A − X, X − B − Y* , etc, aside from the FNN pairs. Simultaneous treatment of SRO of FNNs and SNNs is not possible within a pair approximation; rather, the effect of SNN interactions upon the ordering is considered. The SNN pair-exchange reaction

$$(A - X - A) + (B - X - B) = 2(A - X - B) \tag{71}$$

corresponds to the pair exchange energy $\Delta g_{\frac{AB}{X}}$, which is composition (and possibly temperature) dependent and can be described using coefficients obtained from fitting experimental data for binary AX-BX solutions. The Gibbs energy in the pair approximation is given by

$$G = \left(n_{\frac{A}{X}} g^{\circ}{}_{\frac{A}{X}} + n_{\frac{A}{Y}} g^{\circ}{}_{\frac{A}{Y}} + n_{\frac{B}{X}} g^{\circ}{}_{\frac{B}{X}} +_{\dots}\right) - T\Delta S^{\text{config}} + G^{XS}\left(n_{\frac{i}{p}}, z_i, z_p, \Delta g_{\frac{ij}{p}}, \Delta g_{\frac{i}{pq}}\right) \tag{72}$$

where i, j represent cations and p, q represent anions. G^{XS} depends on the following quantities: $n_{\frac{\mathrm{i}}{\mathrm{p}}}$ is the number of moles of FNN $(i - p)$ pairs, z_i and z_p are the FNN coordination numbers of cation and anion, respectively. $\Delta g_{\frac{\mathrm{ij}}{\mathrm{p}}}$ and $\Delta g_{\frac{\mathrm{i}}{\mathrm{pq}}}$ are the pair exchange energy [101].

Appendix B: Discussion on the use of Thermochimica and MSTDB-TC

MSTDB-TC coupled with Thermochimica is a powerful tool for predicting thermodynamic properties in various systems. However, caution is warranted when interpreting the predicted chemical potentials of elements, as the ability to solve for unique values depends on the equilibrium phases present and the definition of system components, as discussed in Refs. [113, 114] and illustrated in Figure 27. Figure 27a, reproduced from Ref. [113], depicts a hypothetical A-B binary system featuring two stoichiometric phases (A(s), A_2B_3) and one solid solution phase (α(s)). If an equilibrium calculation predicts the stoichiometric phase A_2B_3 to be stable (indicated by the vertical dotted line), and the overall system composition is exactly A_2B_3, the chemical potentials are defined by A_2B_3 itself. However, if this point represents a boundary where A_2B_3 could be in equilibrium with either A(s) (e.g., along a common tangent like the green dotted line to the left) or A(s) (e.g., along a common tangent like the red dotted line to the right), then simply targeting the A_2B_3 composition might not yield uniquely defined chemical potentials representative of a specific two-phase-field. Applying the Gibbs Phase Rule (GPR) at constant temperature and pressure ($DOF = C - P$), for a binary system ($C = 2$) with a single-phase stable ($P = 1$), $DOF = 2 - 1 = 1$. This single degree of freedom corresponds to the ambiguity of A_2B_3 being part of different two-phase equilibria. Figure 27b schematically illustrates molar Gibbs energy considerations for the Cr-Na-Cl ternary molten salt system (not to scale), with system components defined as Na, Cr, and Cl. If one considers Gibbs energy data points corresponding to pure liquid NaCl, pure liquid $CrCl_2$, and an intermediate liquid NaCl–$CrCl_2$ mixture, these compositions are collinear (dotted line) within the ternary composition space. Such collinear data points are insufficient to uniquely define a Gibbs tangent plane to the liquid solution's Gibbs energy surface. In other words, characterizing the molar Gibbs energy of a molten salt solution phase along only one compositional direction (a pseudo-binary join) does not provide sufficient information to determine unique values for the chemical potentials of constituent elements throughout the entire phase region via a simple tangent construction. Applying the GPR to this scenario: with three fundamental components (Na, Cr, Cl; $C = 3$) and one liquid phase ($P = 1$), if an additional constraint is imposed by restricting compositions to the pseudo-binary NaCl–$CrCl_2$ join (effectively fixing one compositional relationship, $R = 1$), the degrees of freedom become one ($DOF = C - P - R = 3 - 1 - 1 = 1$). Therefore, one compositional degree of freedom remains, meaning the chemical potentials of Na, Cr, and Cl are functions of this single variable (e.g., the mole fraction of NaCl along the join) and are not yet uniquely fixed. Even if one specifies that variable, the computational method using elemental components struggles to find those non-unique potential values robustly due to the collinearity. If the system components are defined as NaCl and $CrCl_2$, instead, the degrees of freedom are still one as $DOF = C - P = 2 - 1 = 1$. There is still one way one can vary the composition (the ratio/mole fraction of NaCl to $CrCl_2$). However, $\mu NaCl$ and $\mu CrCl_2$ are well defined once the mixture ratio is specified, because this setup is more computationally unique for compositions along the NaCl–$CrCl_2$ join by avoiding the 'rank-deficient Hessian' issue (detailed in Refs. [113, 114]) that arises when trying to get elemental potentials directly from the elemental component definition in the collinear case. Once $\mu NaCl$ and $\mu CrCl_2$ are uniquely determined, these values in conjunction with the overall elemental stoichiometry defined (i.e., the fixed ratio of Na:Cr:Cl for that specific mixture), allow for the determination of unique chemical potential values for the elements (μNa, μCr, μCl) consistent with that thermodynamic state. Assuming the system components remain Na, Cr, and Cl, unique chemical potential values for these elements can be determined if a second phase coexists with the molten salt at equilibrium, as illustrated in Figure 27c. The presence of this second phase shifts the system off the line and provides additional thermodynamic constraints. This scenario can be achieved if there is a slight surplus or deficit of one of the chemical elements relative to the stoichiometry of the primary salt components, potentially leading to the precipitation of a phase like solid Cr if its solubility in the salt is exceeded. In this situation, with C = 3 (e.g., Na, Cr, Cl) and P = 2 (e.g., liquid salt + solid Cr), the GPR yields DOF = C − P = 3 − 2 = 1. If an additional constraint (R = 1) is imposed, such as fixing the ratio of certain solvent components (effectively constraining the molten salt's composition to vary along a specific line in ternary space as solute is added), then DOF = C − P − R = 3 − 2 − 1 = 0. This invariant state means the compositions of both equilibrium phases and all chemical potential values are uniquely fixed. Graphically, a unique common tangent plane is defined, connecting the Gibbs energy of the molten salt (at its now fixed equilibrium composition on that 'line') and the Gibbs energy of the solid Cr phase.

The relationship between the system component defined, equilibrium phases, and the predicted chemical potentials is summarized in Table 11 for a Na-Cr-Cl ternary molten salt system. It is important to note that for the calculations presented in Figure 15 (e.g., varying X_{CrF_2} in a FLiNaK–CrF_2 system), a trace amount of solid Cr was predicted to be stable even at the lowest CrF_2 concentrations considered (potentially due to solver tolerances). The amount of this solid Cr phase increases as adding more CrF_2 approaches the solubility limit. Consequently, under the conditions and overall compositions explored in Figure 15, the molten salt was never the sole equilibrium phase; it was always in equilibrium with solid Cr.

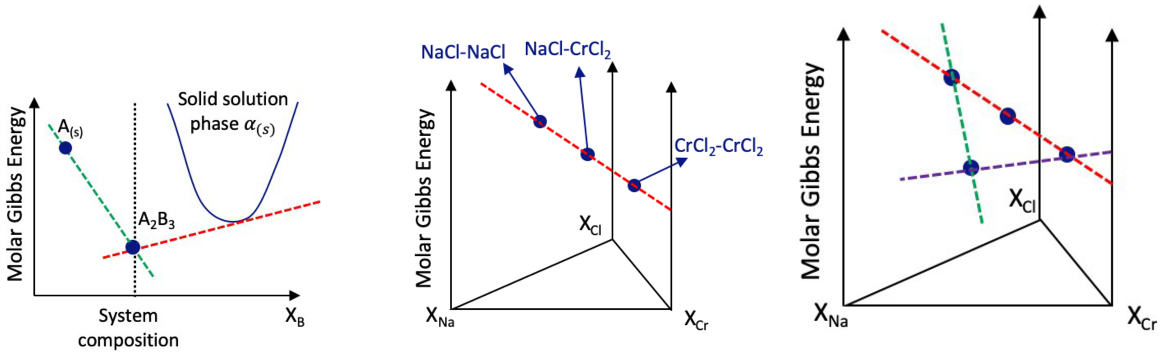

(a) (b) (c)

Figure 27: Molar Gibbs energy versus system composition diagrams (at constant temperature and pressure) for visualizing the determination of chemical potentials. (a) Molar Gibbs energy plot for a hypothetical A-B binary system featuring stoichiometric phases (A(s), A_2B_3) and a solid solution ($\alpha(s)$), reproduced based on Ref. [113]. If the overall system composition is that of the line compound A2B3, a unique common tangent line cannot be determined as A2B3 can be in equilibrium with either $\alpha(s)$ or A(s) phase. (b) Molar Gibbs energy representation for compositions within the pseudo- binary NaCl– CrCl2 join of the Cr-Na-Cl ternary molten salt system. The linear molar Gibbs energy (indicated by the dotted line) is insufficient to define a unique Gibbs tangent plane in the ternary space, illustrating how having only the molten salt phase does not uniquely determine chemical potential. (c) Illustration for the Cr-Na-Cl ternary molten salt system when the molten salt phase (whose compositions may vary, e.g., along a specific solvent ratio line) is in equilibrium with a distinct second phase (e.g., solid Cr). In this scenario, a unique Gibbs tangent plane (indicated by the triangle formed by dotted lines) is established.

Table 11: Summary of the uniqueness of chemical potentials calculated from MSTDB-TC using Thermochimica based on the defined system components, phases at equilibrium, chemical potentials of interest.

System Component	Equilibrium Phases (at Fixed T, P)	DOF	Potential of Interest	Uniquely Defined?	Notes
Elements (Na, Cr, Cl)	Molten salt (only general composition)	2	Na, Cr, Cl	No	Two compositional variables (e.g., X_{Na}, X_{Cr}) are needed to fix the state.
Elements (Na, Cr, Cl)	Molten salt constrained to $NaCl-CrCl_2$ join	1	Na, Cr, C	No	One compositional variable (position on the join) is needed. According to Piro et al. [113], it is computationally problematic for elemental potentials due to collinearity.
Compounds ($NaCl, CrCl_2$)	Molten salt (mixture of NaCl and $CrCl_2$)	1	$NaCl, CrCl_2$	No	One compositional variable (e.g., X_{NaCL}) is needed.
Compounds ($NaCl, CrCl_2$)	Molten salt at specified X_{NaCl}	0	$NaCl, CrCl_2$	Yes	According to Piro et al. [113], these component potentials are computationally unique.
Compounds ($NaCl, CrCl_2$)	Molten salt at specified X_{NaCl}	0	Na, Cr, Cl	Yes	Elemental potentials are derivable from unique component potentials for this fully specified mixture.
Elements (Na, Cr, Cl)	Molten salt and one other phase (e.g., solid Cr)	1	Na, Cr, Cl	No	Potentials are fixed by the 2-phase equilibrium (tangent plane). $DOF = 1$ refers to varying bulk composition along the common tangent plane, not potential values.
Elements (Na, Cr, Cl)	Molten salt (on $NaCl-CrCl_2$ join, specified X_{NaCl}) and one other phase (e.g., solid Cr)	0	Na, Cr, Cl	Yes	System is invariant; adding a second phase to the constrained join resolves ambiguity and fixes potentials.

Appendix C: Phase-field Modeling

Electrochemical PFM - assumptions and the treatment of electrostatic potential

The literature presents numerous electrochemical phase-field models, differing in the species tracked, the formulation of interfacial kinetics, and the treatment of the electrostatic potential ϕ [132, 133, 165–171]. The simplest assumption regarding ϕ is a constant potential in the bulk phases and a sharp interfacial potential difference between the solid and liquid phase, $\Delta\phi^{l-s}$, while taking the solid electrostatic potential ϕ^s as the reference, as depicted in Figure 24. The profile of ϕ is represented by the dotted line. It is sharp, discontinuous, and has the profile of a step function. Within this category, Liang et al. [132] first proposed a model (shown in the left panel of Figure 24, labeled as Model #1) where they consider a simple general electrode reaction

$$M^{z+} + ze^- \leftrightarrow M \tag{73}$$

where the ions M^{z+} in the electrolyte solution react with electrons e^- in the electrode to produce the electrode M atoms. This model focuses on the electrode kinetics and assumes that a_{Mz+} is constant and does not evolve with time. In this case, there will be no overpotential drop for the charge transport nor the EDL; i.e., the entire overpotential drop is associated with the electrode reaction. Inspired by Model #1, a slightly more complicated model is shown in the right panel of Figure 24, labeled as Model #2, where the diffusion of species is governed by Equation (62). The simulation domain comprises a solid phase and a liquid electrolyte. The solid can be either a pure reactive metal, M, or an A–M alloy, where component A is nobler than M. This setup is relevant, for instance, to Ni(A)-Cr(M) structural alloys in MSRs or to the electrodeposition of M onto an inert substrate like Pt in electroanalysis. The liquid phase contains the reactive cation M^{z+} and a second species B. Component A is treated as a neutral species within the metallic solid phase. As a significant model simplification to isolate the electrostatic effects of the reactive species, in this formulation, B is also treated as charge neutral ($z_B = 0$). Although B might represent a component of the bulk molten salt (like KCl, which physically consists of K^+ and Cl^- ions), this model approximates its role electrostatically as neutral. Consequently, while B affects the activity coefficient of M^{z+} and its concentration is tracked via diffusion, it does not contribute to the local charge density ρ or the electrostatic energy term f_{elec}. The primary electrochemical focus remains on the behavior of M^{z+}. The model tracks the molar fractions of A, B, and M^{z+}, assuming constant valences throughout the domain (i.e., $z_{i,s} = z_{i,l} = z_i$). Key assumptions are that the solid acts as an ideal electron source/sink (non-limiting electron availability) and that sufficient immobile background anions are present in the electrolyte to ensure overall charge neutrality in the bulk phase (primarily balancing the M^{z+} cations). The local electrostatic energy density in Models #1 and #2 is approximated by

$$f_{elec}\left(\{x_i\},\{\xi_\alpha\},\Delta\phi^{l-s}\right) = \sum_i x_i\left[z_i F\Delta\phi^{l-s} h_l(\{\xi_\alpha\}) + z_i F\phi^s\right], \tag{74}$$

where $\phi^s = 0$, and $\rho = \sum_i x_i z_i F = x_{M^{z+}} z_{M^{z+}} F$ is calculated solely from the tracked charge species (i.e., M^{z+}). Although the bulk liquid is neutral overall (due to background anions balancing mobile cations), the phase-field model resolves molar fraction gradient of mobile species M^{z+} across the diffuse-interface. This leads to a non-zero local ρ within the interface, which interacts with the imposed potential difference $\Delta\phi^{l-s}$, thus contributing a non-zero f_{elec} specifically in the interfacial region. This term effectively captures the primary electrostatic energy contribution associated with charge separation across the interface without the computational expense of solving Poisson's equation. Therefore, Models #1 and #2 benefit from simple formulations and computational efficiency. However, they neglect electromigration by assuming a flat ϕ profile in the bulk phases (which is appropriate if the molten salt is well-stirred), and they also omit the EDL effects.

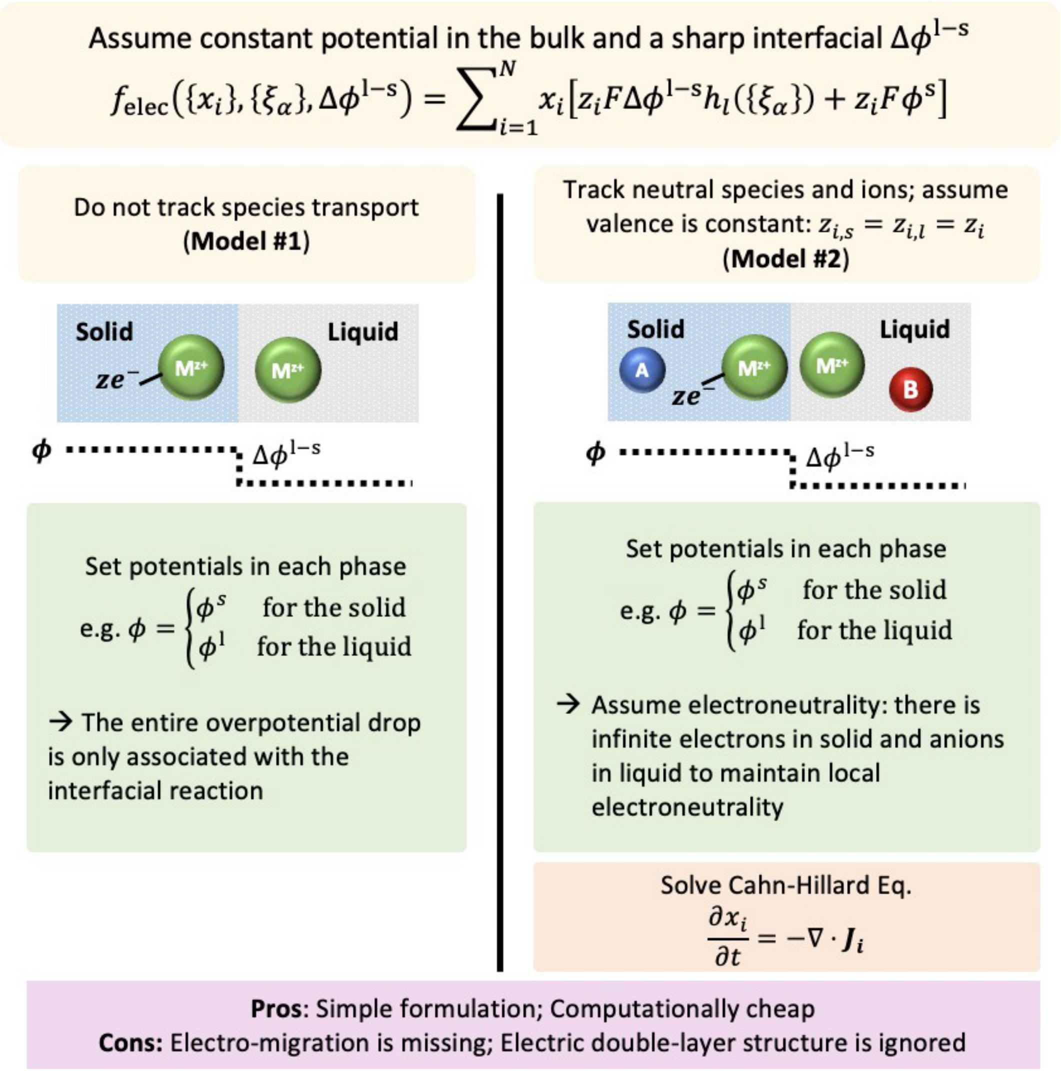

Assume constant potential in the bulk and a sharp interfacial $\Delta\phi^{\mathrm{l-s}}$

$$f_{\mathrm{elec}}(\{x_i\},\{\xi_\alpha\},\Delta\phi^{\mathrm{l-s}}) = \sum_{i=1}^{N} x_i\left[z_iF\Delta\phi^{\mathrm{l-s}}h_l(\{\xi_\alpha\}) + z_iF\phi^{\mathrm{s}}\right]$$

Do not track species transport **(Model #1)**

Set potentials in each phase

$$\text{e.g. } \phi = \begin{cases} \phi^s & \text{for the solid} \\ \phi^{\mathrm{l}} & \text{for the liquid} \end{cases}$$

→ The entire overpotential drop is only associated with the interfacial reaction

Track neutral species and ions; assume valence is constant: $z_{i,s} = z_{i,l} = z_i$ **(Model #2)**

Set potentials in each phase

$$\text{e.g. } \phi = \begin{cases} \phi^s & \text{for the solid} \\ \phi^{\mathrm{l}} & \text{for the liquid} \end{cases}$$

→ Assume electroneutrality: there is infinite electrons in solid and anions in liquid to maintain local electroneutrality

Solve Cahn-Hillard Eq.

$$\frac{\partial x_i}{\partial t} = -\nabla\cdot\boldsymbol{J}_i$$

Pros: Simple formulation; Computationally cheap
Cons: Electro-migration is missing; Electric double-layer structure is ignored

Figure 24: Electrochemical phase-field models using a constant electrostatic potential in the bulk and a sharp interfacial electrostatic potential difference $\Delta\phi^{l-s}$ with the solid potential ϕ^s as the reference.

Incorporating electromigration enhances the realism of electrochemical phase-field models, especially if there is significant electrostatic potential gradient in the liquid phase. Accurately capturing ϕ typically involves solving Poisson's equation. However, this significantly adds to the computational costs due to the need to resolve the EDL structure at the scale of the Debye length (often around 1nm) [168]. To circumvent this challenge, some simplified models assume local electroneutrality and neglect EDL effects entirely, including the models depicted in Figure 24. A widely adopted alternative strategy, which accounts for electromigration driven by potential gradients without explicitly resolving the EDL via Poisson's equation, is to employ the conserved current condition (CCC). This approach contrasts with simpler models that assume a flat potential profile. The CCC starts from the fundamental charge conservation law (continuity equation for charge)

$$\frac{\partial \rho}{\partial t} + \nabla \cdot \mathbf{i} = 0 \tag{75}$$

where i is the current density. The time needed for charge accumulation across the interface due to the diffusion of ionic species is much longer than that required to achieve steady-state charge accumulation across the interface, so the conservation of charge can be considered at a steady state [172]. The relation given in Equation (75) is reduced to [168,170]:

$$\frac{\partial \rho}{\partial t} = \nabla \cdot \mathbf{i} = 0 \tag{76}$$

Figure 25 shows the different phase-field electrochemical models using the CCC. For all the models using CCC presented here, electroneutrality is either assumed or explicitly enforced, and the CCC solves for the potential profile. They all assume that there is infinite number of electrons in the solid to compensate the net charge. The models differ mainly in the interpolation scheme, how CCC is imposed, and the diffusion equation. Model #3 tracks neutral and charged species and assumes that the valence is constant within the domain, e.g., $z_{i,s} = z_{i,l} = z_i$. Its local electrostatic energy density is:

$$f_{elec} = \sum_i x_i \, z_i \phi(x) \tag{77}$$

There are also two ways to impose the CCC in literature: only within the diffuse interface, or everywhere in the simulation domain. The former has been utilized in Model #3 in Refs. [133,165] as

$$-\nabla \cdot \left[\sigma^{eff} \nabla \mathrm{\phi}(\mathrm{x}) + \mathrm{i_{rxn}}\right] = 0 \tag{78}$$

where $\sigma^{eff} = \sigma^s h_s(\{\xi_\alpha\}) + \sigma^l h_l(\{\xi_\alpha\})$, σ^s and σ^l are the electrode and electrolyte conductivities, respectively. $\mathrm{I_{rxn}}$ describes the reaction current generated by the interfacial electrochemical reaction. The electromigration current density is $\mathrm{i_{mig}} = \sigma^{eff}\nabla\phi(\mathrm{x})$. Therefore, Equation (79) indicates that $\mathrm{i} = \mathrm{i_{mig}} + \mathrm{i_{rxn}}$. The current due to diffusion of charged species is not directly incorporated into Equation (78) because the dominant term governing the potential field $\phi(x)$ is often $\mathrm{i_{mig}}$. While concentration gradients that drive diffusion exist, the model often treats their primary effect as influencing species transport and reaction rates, rather than directly contributing a separate flux term to the equation being solved for $\phi(x)$. The model structure is simplified, and the coupling between diffusion and CCC is still maintained through σ^{eff} and $\mathrm{i_{rxn}}$. In Ref. [133], the divergence of $\mathrm{i_{rxn}}$ is represented by a source term

$$-\nabla \cdot \mathrm{i_{rxn}} = I_R \tag{79}$$

where I_R is related to the reaction rate by $I_R = nFc_s\frac{\partial \xi_s}{\partial t}$ and c_s is the site density of M-metal. The relationship between reaction rate and phase-field evolution rate is discussed in Section 4.4.2.3. Equation (79) is physically reasonable because $-\nabla \cdot \mathrm{i_{rxn}}$ is the rate at which reaction charge leaves a volume (net outflow), and I_R is the rate at which charge is generated within the volume; charge generated must equal the negative of the net outflow due to reactions. Substituting Equation (79) into Equation (78) gives the CCC that appears in Ref. [133]

$$\nabla \cdot \left[-\sigma^{eff}\nabla\phi(\mathrm{x})\right] = I_R \tag{80}$$

Since both neutral M and cation M^{z+} are tracked in Model #3 (for a pure metal $x_M = \xi_s$), their molar fraction evolution must have an interfacial source/sink term R_i related to the reaction rate, added to Equation (62), and written in general as

$$\frac{\partial x_i}{\partial t} = -\nabla \cdot \mathrm{J_i} + R_i \tag{81}$$

In Ref. [133], $R_i = -\frac{c_s}{c_0}\frac{\partial \xi_s}{\partial t}$, where c_0 is the standard bulk concentration of electrolyte solution. The study models the dendritic patterns during electrodeposition, applied to lithium-ion battery. Reference [173] contains a similar formulation of CCC, and models intergranular corrosion kinetics in sensitized metallic materials.

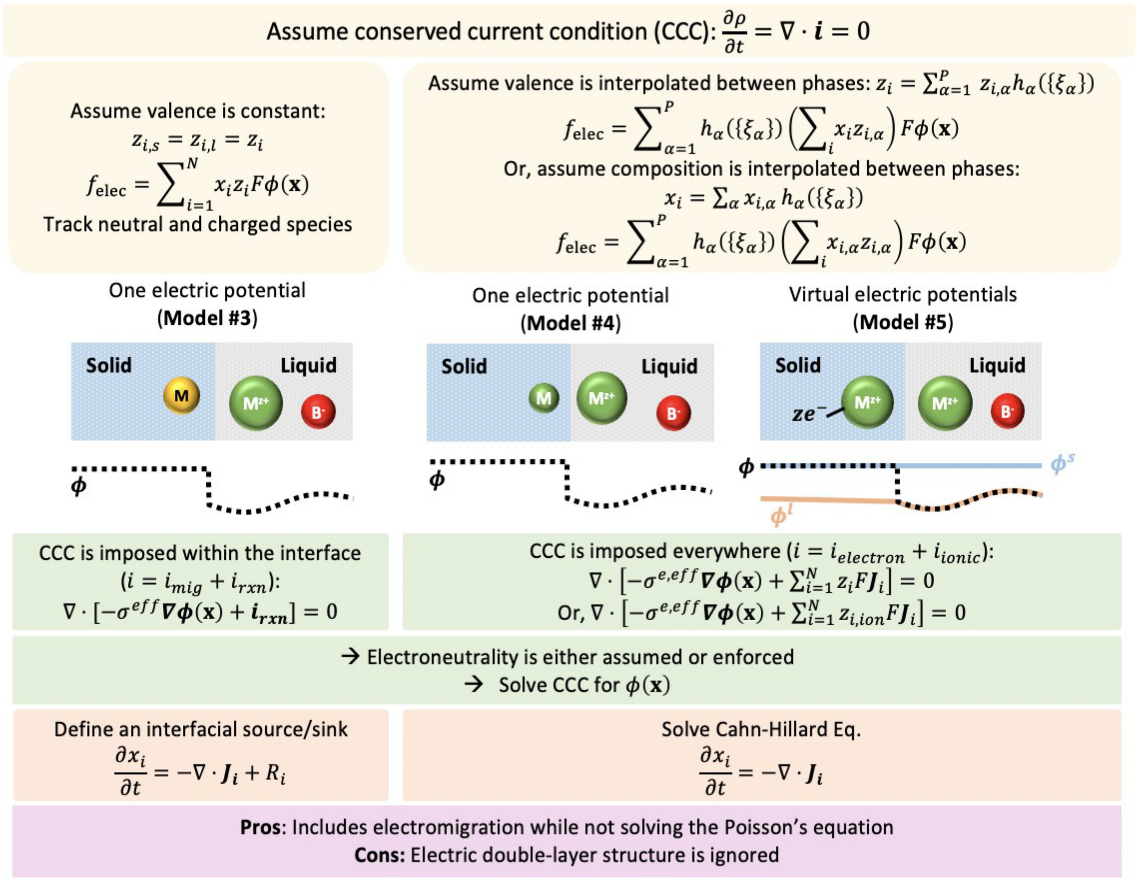

Figure 25: Electrochemical phase-field models assuming the conserved current condition.

An alternative modeling strategy employs valence interpolation, defining an effective, spatially varying valence $z_i = \sum_\alpha z_{i,\alpha} h_\alpha(\{\xi_\alpha\})$, where $z_{i,\alpha}$ is the constant valence of species i in phase α. Consequently, the local electrostatic energy density is

$$f_{elec} = \sum_\alpha h_\alpha(\{\xi_\alpha\}) \left(\sum_i x_i z_{i,\alpha}\right) F\phi(x) \tag{82}$$

This approach allows the reacting species (e.g., M^{z+} and M) to be represented by a single molar fraction field (x_M). Key advantages include reducing the number of independent variables and simplifying the diffusion equation (Equation (62)) by eliminating explicit reaction source/sink terms. Because the reaction is implicitly handled via the flux divergence $\nabla \cdot \mathrm{J_M}$, the CCC governing the electrostatic potential ϕ can be applied throughout the entire domain, including the diffuse interface, as

$$\nabla \cdot \left[-\sigma^{e,eff} \nabla\phi(\mathrm{x}) + \sum_i z_i F \mathrm{J_i}\right] = 0 \tag{83}$$

where $\sigma^{e,eff} = \sum_\alpha \sigma^{e,\alpha} \, h_\alpha(\{\xi_\alpha\})$ is the interpolated electronic conductivity. This equation represents $\nabla \cdot \mathrm{i} = 0$, equivalent to Equation(78), with total current $\mathrm{i} = \mathrm{i}_{\mathrm{electronic}} + \mathrm{i}_{\mathrm{ionic}}$, where $\mathrm{i}_{\mathrm{electronic}} = -\sigma^{e,eff} \nabla \phi(\mathrm{x})$ and $\mathrm{i}_{\mathrm{ionic}} = \sum_i z_i \, F \mathrm{J}_\mathrm{i}$. Reference [169], depicted as Model #4 in Figure 25, utilized such a valence interpolation scheme, combining it with a grand potential formulation to model the corrosion of structural alloys by molten salt.

Another approach is composition partitioning, characteristic of KKS models. Here, the overall composition x_i results from partitioning among phase-specific compositions, $x_{i,\alpha}$, determined by local thermodynamic equilibrium: $x_i = \sum_\alpha x_{i,\alpha} \, h_\alpha(\{\xi_\alpha\})$. Valence ($z_{i,\alpha}$) is treated as an intrinsic, constant property of species i within phase α (e.g., $z_{i,s} = 0, z_{i,l} \neq 0$). Conceptually, the electrostatic energy density consistent with this framework can be represented as

$$f_{elec} = \sum_\alpha h_\alpha \left(\{\xi_\alpha\}\right) \left(\sum_i x_{i,\alpha} \, z_{i,\alpha} \right) F \phi(x) \tag{84}$$

Charge conservation is governed by the CCC equation:

$$\nabla \cdot \left[-\sigma^{e,eff} \nabla \phi(\mathrm{x}) + \sum_i z_{i,ion} \, F \mathrm{J}_\mathrm{i} \right] = 0 \tag{85}$$

where $z_{i,ion}$ is the constant valence of the species when ionic ($z_{i,ion} = 0$ if the species only moves when neutral). Diffusion is governed by the flux laws inherent to the KKS formulation (Equation (62)). This composition partitioning approach, having the same domain illustration as Model #4, was utilized by Wu et al. [72] within a KKS framework to model stainless steel oxidation, capturing multiple oxide layer growth.

A distinct approach, proposed recently by Zhang et al. [171], introduces separate electrostatic potential fields for the electrode (ϕ^s) and the electrolyte (ϕ^l) as independent variables (illustrated as Model #5 in Figure 25). Although defined everywhere, these "virtual" potentials ϕ^s and ϕ^l are physically meaningful only within their respective bulk phases. This method still utilizes "virtual" phase-specific molar fractions ($x_{i,\alpha}$) akin to the KKS formulation (composition partitioning) to describe the local state. To enhance computational efficiency and avoid explicitly solving local quasi-equilibrium equations, Zhang et al. adopted the grand potential formulation, where local equilibrium is inherently satisfied. Compared to models employing a single electrostatic potential field, this dual-potential formulation offers greater flexibility in capturing the potential jump across the diffuse electrode-electrolyte interface, including spatial variations in this jump along the interface, without the need for computationally expensive resolution of the EDL structure. The main benefit of models using the CCC equation is that they include electromigration while not having to solve the Poisson's equation. However, the detailed EDL structure is still not captured.

The final category of electrochemical phase-field models reviewed here explicitly resolves the EDL structure by directly solving Poisson's equation and simulating electron transport [166,167]. Figure 26 illustrates the model's principles. A representative system might include charged components like electrons e^-, cations M^{z+}, cations A^{a+}, and anions B^-, treated with constant valences (z_i). Such models can simulate alloy electrodeposition and dissolution. Transport is often described using a generalized Cahn-Hilliard framework. The evolution of substitutional species (M^{z+}, A^{a+}, and B^-) considers cross-diffusion effects:

$$\frac{\partial x_i}{\partial t} = -\nabla \cdot \mathrm{J_i} = \nabla \cdot \sum_{j=1, j\neq e^-}^{N-1} M_{ij} \nabla \left(\frac{\delta \mathcal{F}}{\delta \mathrm{x_j}}\right) \tag{86}$$

while the evolution of interstitial electrons is treated separately:

$$\frac{\partial x_{e^-}}{\partial t} = -\nabla \cdot \mathrm{J_{e^-}} = \nabla \cdot M_{e^-} \nabla \left(\frac{\delta \mathcal{F}}{\delta \mathrm{x_{e^-}}}\right) \tag{87}$$

This formulation reflects that substitutional species are coupled (movement requires displacement of others), while electron flux is independent of substitutional site occupancy. Crucially, the electrostatic potential ϕ is obtained by directly solving Poisson's equation:

$$\nabla \cdot [\epsilon(\{\xi_\alpha\}) \nabla \phi(\mathrm{x})] + \rho = 0 \tag{88}$$

where $\epsilon(\{\xi_\alpha\}) = \sum_\alpha \epsilon_\alpha h_\alpha(\{\xi_\alpha\})$ is the interpolated effective permittivity, and the local charge density is $\rho = \frac{F}{V_m} \sum_{i=1}^{N} z_i x_i$. Although direct flux coupling between substitutional species and electrons is neglected in Eqs. (86) and (97), all species fluxes are indirectly coupled via the electrostatic potential, which depends on the total charge distribution ρ through Equation (88). This high-fidelity approach requires resolving charge distributions near interface (often on the nanometer scale), limiting practical domain sizes and simulation times, making it the most computationally demanding method discussed. Adaptive mesh techniques and implicit solution methods are promising for enabling simulations over large domains and long timescales [166]. Adaptive Mesh Refinement (AMR), in particular, has proven effective. For instance, an AMR method was specifically developed to simulate EDL formation, allowing for modeling of arbitrarily complex geometries with resolutions spanning from nanometers in the EDL to micron/millimeter scales in the bulk particle/electrode regions [174]. Building upon this, Qu et al. [175] used AMR within the Smoothed Boundary Method (SBM) framework to simulate electrochemical impedance spectroscopy coupled with complex electrode microstructures and interfacial morphology. They employed high mesh refinement near the electrode particle-electrolyte interfaces to model EDL formation and calculate double layer capacitance. Since the authors did not directly resolve the double layers in the complex microstructure simulations, a low level of AMR was used only to ensure the numerical accuracy. The AMR method has also been applied by Malik et al. [176] to simulate the performance of lithium-ion batteries (e.g., cell voltage curves, cyclic voltammograms) as affected by electrode microstructure. It is noteworthy, however, that these specific SBM-based AMR applications [174-176] assumed a stationary, albeit geometrically complex, electrode-electrolyte interface.

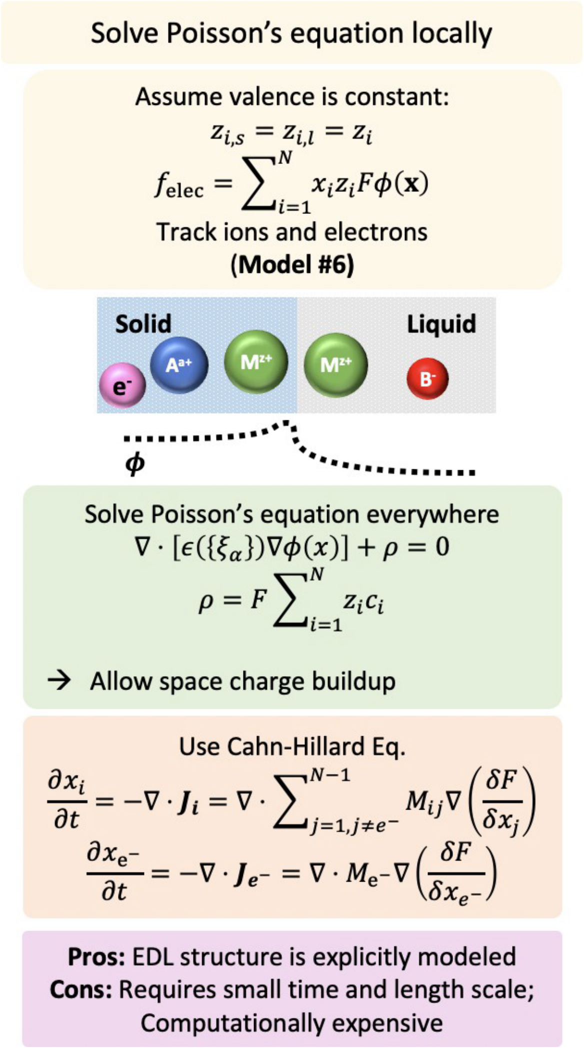

Solve Poisson's equation locally

Assume valence is constant:

$$z_{i,s} = z_{i,l} = z_i$$

$$f_{\mathrm{elec}} = \sum_{i=1}^{N} x_i z_i F \phi(\mathbf{x})$$

Track ions and electrons

(Model #6)

Solve Poisson's equation everywhere

$$\nabla \cdot [\epsilon(\{\xi_\alpha\}) \nabla \phi(x)] + \rho = 0$$

$$\rho = F \sum_{i=1}^{N} z_i c_i$$

→ Allow space charge buildup

Use Cahn-Hillard Eq.

$$\frac{\partial x_i}{\partial t} = -\nabla \cdot \boldsymbol{J}_i = \nabla \cdot \sum_{j=1, j \neq e^-}^{N-1} M_{ij} \nabla \left(\frac{\delta F}{\delta x_j} \right)$$

$$\frac{\partial x_{\mathrm{e}^-}}{\partial t} = -\nabla \cdot \boldsymbol{J}_{e^-} = \nabla \cdot M_{\mathrm{e}^-} \nabla \left(\frac{\delta F}{\delta x_{e^-}} \right)$$

Pros: EDL structure is explicitly modeled

Cons: Requires small time and length scale; Computationally expensive

Figure 26: Electrochemical phase-field models modeling explicitly the electric double layer structure.

Electrochemical PFM - interface kinetics

The modeling of interfacial evolution kinetics often utilizes classical rate theory, akin to chemical reaction kinetics, as an alternative to the linear kinetics assumed by the Allen-Cahn equation. The justification stems from fundamental electrochemical principles. Specifically, Faraday's law (Equation (43)) provides a relationship between the current density i and the normal interfacial velocity v: $i = \frac{Fn}{V_m} v$. Recognizing that the rate of phase-field change $\frac{\partial \xi}{\partial t}$ depends on this velocity according to $\frac{\partial \xi}{\partial t} = \frac{\partial \xi}{\partial x} \frac{\partial x}{\partial t} = \nabla_x \xi v$, it directly follows that $\frac{\partial \xi}{\partial t}$ is proportional to i.

The functional relationship between $\frac{\partial \xi}{\partial t}$ and the overpotential η may be nonlinear, semi-linear, or linear. Which regime applies is determined by the relative magnitude of the overpotential and the specific simplifying assumptions adopted in the model. Zhang et al. [171], for example, have explored the case of nonlinear phase evolution kinetics. They utilized the variational overpotential [130,168]

$$\eta = \frac{V_m}{nF}\frac{\delta \Omega}{\delta \xi}$$

(89)

where Ω is the grand potential of the electrochemical system. To fulfill the second law of thermodynamics, the following constitutive relations from nonequilibrium thermodynamics is used

$$\frac{\partial \xi}{\partial t} = -\frac{V_m}{6F\delta_{intf}} i(\eta)$$

(90)

where δ_{intf} is the width of the diffuse-interface, and the constant before $i(\eta)$ merely makes i the interfacial current density. Here $i(\eta)$ describes the general reaction and can be determined theoretically or experimentally. The Butler-Volmer (BV) kinetics provides a description of $i(\eta)$ as shown in Equation (46). This study also incorporates the Marcus model, characterized by the solvent reorganization energy λ. A key simplification, discussed in Section 4.2, occurs when $E_{eq} = E^{0'}$. In this scenario, the Marcus kinetics can be expressed in the same form as the BV equation. This equivalence is achieved by defining the effective transfer coefficient α via Equation (54), noting that $\eta = E - E_{eq} = E - E^{0'}$. Applying this simplification, the Marcus kinetic equation, based on Ref. [171], becomes

$$i(\eta) = i_0 \left\{ \exp\left[\left(\frac{1}{2} - \frac{nF\eta}{4\lambda}\right)\frac{nF\eta}{RT}\right] - \exp\left[\left(-\frac{1}{2} + \frac{nF\eta}{4\lambda}\right)\frac{nF\eta}{RT}\right] \right\}$$

(91)

The Marcus-Hush-Chidsey (MHC) theory [177,178] extends the Marcus framework by integrating the electrode's electronic structure (Fermi level, density of states). This provides a more physically realistic description of heterogeneous electron transfer rates, treating them as a continuous function of electrode potential. The MHC model is

$$i(\eta) = \frac{i_0}{A}\left\{ \int_{-\infty}^{+\infty} \exp\left[-\frac{(x - \frac{\lambda}{RT} + \frac{nF\eta}{RT})^2}{\frac{4\lambda}{RT}}\right]\frac{dx}{1 + \mathrm{e}^x} - \int_{-\infty}^{+\infty} \exp\left[-\frac{(x - \frac{\lambda}{RT} - \frac{nF\eta}{RT})^2}{\frac{4\lambda}{RT}}\right]\frac{dx}{1 + \mathrm{e}^x} \right\}$$

(92)

where $A = \int_{-\infty}^{+\infty} \exp\left[-\frac{(x-\lambda/RT)^2}{\frac{4\lambda}{RT}}\right]\frac{1}{1+\mathrm{e}^x} dx$. To make the MHC model computationally tractable within their phase-field simulations, Zhang et al. [171] employed a polynomial fit of the numerical integration results. This approach avoids the significant computational expense of performing the full MHC integration at every grid point and timestep. They subsequently verified that their phase-field model, using this approximation, accurately captures the analytical reaction kinetics, even at high overpotentials. In related work, Cogswell [168] incorporated Marcus reaction kinetics into a phase-field framework, because Marcus kinetics approximates the MHC kinetics at small overpotential.

Simplifications are often made to the nonlinear reaction kinetics in phase-field models. In Ref. [132], Liang et al. were the first to use nonlinear model to describe the temporal and spatial evolution of the phase-field variable as

$$\frac{\partial \xi}{\partial t} = -RTk_n \left[\exp\left(\frac{\frac{\alpha \delta F}{\delta \xi}}{RT} \right) - \left(-\frac{\frac{(1-\alpha)\delta F}{\delta \xi}}{RT} \right) \right] \tag{93}$$

where k_n is the reaction rate constant. However, the authors [132] found, through asymptotic analysis and numerical simulations of its sharp-interface limit, that the kinetics described by Equation (93) are sensitive to the choice of interpolating function. Furthermore, mapping parameters to conventional electrode kinetic models proves difficult because this limit lacks a simple analytical form. To overcome these limitations, they proposed a simplified "semi-linear" kinetic model. In this formulation, the interface migration velocity depends linearly on the interfacial free energy reduction (typically the smaller driving force component) but nonlinearly on the overpotential (typically the larger component). This approach ensures the overall nonlinear dependence of the reaction rate on the driving force remains consistent with standard chemical kinetic rate theories. The semi-linear kinetics equation is

$$\frac{\partial \xi}{\partial t} = -L_\sigma \frac{\delta f_{intf}(\{\xi_\alpha\})}{\delta \xi} - L_\eta RT h'_\alpha(\{\xi_\alpha\}) \left[\exp\left(\frac{\alpha \Delta G}{RT}\right) - \exp\left(-\frac{\beta \Delta G}{RT}\right) \right] \tag{94}$$

where L_σ is the interface mobility, and L_η is a reaction rate constant. $L_\sigma = RTL_\eta = M_\xi$, where M_ξ is the interfacial mobility in Equation (63). The thermodynamic driving force $\Delta G = zF\eta$ for an electrode reaction (73). The analytical solution of the interfacial velocity, v, under the sharp-interface limit of Equation (94), is obtained from asymptotic analysis in Ref. [179] and written as [133]

$$v = -\frac{\kappa_\xi L_\eta RT}{\sigma} \left[\exp\left(\frac{\alpha z F \eta}{RT}\right) - \exp\left(-\frac{\beta z F \eta}{RT}\right) \right] \tag{95}$$

where σ is the interfacial energy per unit area between electrode and electrolyte. By using Equation (95), one can calibrate the interface mobility M_ξ from the experimental measured exchange current density i_0 based on the Faraday's law (Equation (43)). To develop a *thermodynamically consistent* phase-field model, Chen et al. [133] incorporated Bazant's nonequilibrium thermodynamics framework [130], specifically utilizing the excess electrochemical energy analysis detailed in Section 4.2. They considered an electrodeposition system governed by reaction (73), defining c, c_+, c_- as the concentrations for M-atom, M^{n+} cations, and A^{n-} anions in the liquid solution, respectively. A key assumption is that the solid phase consists of pure M-metal (with site density c_s) allowing the solid phase fraction ξ_s to be defined relative to the local M-atom concentration c as $\xi_s = \frac{c}{c_s}$. Under the further assumptions of BV kinetics, a dilute electrolyte solution, and unity electron activity, Chen et al. derived the following expression for the electrochemical reaction rate and phase evolution rate

$$R_e = \frac{\delta \xi_s}{\delta t} = -k_0 \tilde{c}_+^{1-\alpha} a_M^{\alpha} \left\{ \exp\left[\frac{(1-\alpha)nF\eta}{RT}\right] - \exp\left[\frac{-\alpha nF\eta}{RT}\right] \right\}$$

(96)

where η is the variational overpotential, and k_0 is the reaction rate constant. By again assuming that the interfacial energy related to the thermal energy ($kT = 0.0257$ eV) is smaller relative to the electrode reaction affinity when a certain large electrostatic potential (e.g., higher than 0.5V) is applied to the electrodeposition systems, the temporal evolution of phase-field is considered linearly proportional to the interfacial free energy and exponentially to the thermodynamic driving force related electrode reactions, that is

$$\frac{\delta \xi_s}{\delta t} = -L_\sigma \frac{\delta f_{intf}(\{\xi_\alpha\})}{\delta \xi} - L_\eta h'_\alpha(\{\xi_\alpha\}) \left\{ \exp\left[\frac{(1-\alpha)nF\eta_a}{RT}\right] - \tilde{c}_+ \left[\frac{-\alpha nF\eta_a}{RT}\right] \right\}$$

(97)

where $\eta_a = \Delta\phi^{l-s} - E^0$ is the activation overpotential. Alternatively, to deriving it from a variational principle, the total overpotential can be defined as the sum of activation, concentration (η_c), and capillary (η_s) components. The concentration overpotential, η_c, arises from deviations of interfacial concentrations from Nernst equilibrium; for instance, Chen et al. [133] use the form $\eta_c = -\frac{RT}{nF}(\ln\tilde{c}_+ - \ln a_M)$. The capillary overpotential, η_s, accounts for the effect of interfacial curvature on the equilibrium state and is therefore non-zero only in 2D and 3D simulations. It is noteworthy that the semi-linear kinetics formulation (Eqs. (94) and (107)), which relates interfacial evolution rate to such overpotentials, has been employed in numerous studies [132, 133, 165, 173, 180–182] modeling electrochemical problems.

At low overpotential, linearization of Equation (94) recovers the well-known Allen-Cahn equation (63). The analytical interfacial velocity at the sharp-interface limit for the linear phase evolution rate is [133]

$$v = -\frac{\kappa_\xi L_\eta zF}{\sigma} \eta$$

(98)

Under a high positive overpotential, the forward electrode reaction, the reduction reaction, dominates over the reverse reaction, and the sharp-interface limit of the nonlinear phase-field equation reduces to the Tafel Equation (47):

$$v = -\frac{\kappa_\xi L_\eta RT}{\sigma} \exp\left(\frac{\alpha zF\eta}{RT}\right)$$

(99)

The linear phase evolution kinetics has been widely adopted in Refs. [167, 169, 170, 172, 183].

Appendix D: Lattice Gas Model

In the case of lattice gas models, the system is supposed to be a cubic lattice in dimension d with lattice spacing a, uniform for both solid and liquid phases. This leads to the approximation of the occupancy for each site i:

$$p_k^\alpha(t) = \langle n_k^\alpha \rangle(t) = \sum_n n_k^\alpha \, P(n,t) \tag{100}$$

where α denotes the type of particle present at the site (e.g., metal, cation, anion, solvent or vacancy), n_k^α is 1 α is present on site k and 0 otherwise, and n is one configuration for the entire system.

For a system composed of metal 0, cations $+$, anions $-$, and solvent s, the following evolution equations are obtained for each of them:

$$\frac{\partial p_k^0}{\partial t} = -\sum_a \tilde{J}_{k,k+a}^0 + \sum_a \sigma_{k,k+a} \tag{101}$$

$$\frac{\partial p_k^+}{\partial t} = -\sum_a \tilde{J}_{k,k+a}^+ - \sum_a \sigma_{k,k+a} \tag{102}$$

$$\frac{\partial p_k^-}{\partial t} = -\sum_a \tilde{J}_{k,k+a}^- \tag{103}$$

$$\frac{\partial p_k^s}{\partial t} = -\sum_a \tilde{J}_{k,k+a}^s \tag{104}$$

with vacancies simulated as $p_k^v = 1 - (p_k^0 + p_k^+ + p_k^- + p_k^s)$. Displacements are modeled as jumps into vacancies. The flux thus follows an Arrhenius law that governs the jump of the particle into the vacancy. The energy barrier of such an elementary step is computed as the sum of the energy to break all the initial bonds of the particle and the difference of local electric field which shifts the energy barrier.

$$J^{\alpha}_{k,k+a} = w^{\alpha}[p^{\alpha}_{k} p^{v}_{k+a} \exp\left(-\frac{1}{kT}\left(\sum_{\beta}\sum_{a'} \varepsilon_{\alpha\beta}\, p^{\beta}_{k+a'} + \frac{q^{\alpha}}{2}(V_k - V_{k+a})\right)\right)$$
$$-p^{\alpha}_{k+a} p^{v}_{k} \exp\left(-\frac{1}{kT}\left(\sum_{\beta}\sum_{a'} \varepsilon_{\alpha\beta}\, p^{\beta}_{k+a'} + \frac{q^{\alpha}}{2}(V_{k+a} - V_k)\right)\right)]$$

(105)

where w^{α} is the attempt frequency for particle α, $\varepsilon_{\alpha\beta}$ is the interaction energy between species α and β, q^{α} is the charge of species α, V_k is the electric potential at site k. It can then be shown that rate can be expressed as $J^{\alpha}_{k,k+a}$:

$$J^{\alpha}_{k,k+a} = -\widetilde{M}^{\alpha}_{k,k+a} D_a \tilde{\mu}^{\alpha}_{k}$$

(106)

with the mobility defined as follows:

$$\widetilde{M}^{\alpha}_{k,k+1} = \frac{w^{\alpha}}{kT} p^{v}_{k} p^{v}_{k+1} \exp\left(\frac{\tilde{\mu}^{\alpha}_{k} + \tilde{\mu}^{\alpha}_{k+1}}{2kT}\right) \frac{\operatorname{shc} D_a \tilde{\mu}^{\alpha}_{k}}{2kT}$$

(107)

and the chemical potential given by:

$$\tilde{\mu}^{\alpha}_{k} = \mu^{\alpha}_{k} + q_{\alpha} V_k = -\sum_{\beta}\sum_{a'} \varepsilon_{\alpha\beta}\, p^{\beta}_{k+a'} + kT \ln\left(\frac{p^{\alpha}_{k}}{p^{v}_{k}}\right) + q_{\alpha} V_k$$

(108)

In addition to mass transport via vacancy-mediated diffusion, lattice gas models can also account for electrochemical reactions, i.e. $\mathrm{M}^{+}_{k} + e^{-}_{k+a} \rightleftharpoons \mathrm{M}^{0}_{k}$ through the term $\sigma_{k,k+a}$. To describe this process, electrons must be included in the system, whose dynamics follow the equations:

$$\frac{\partial p^{e}_{k}}{\partial t} = -\sum_{a} \tilde{J}^{e}_{k,k+a} - \sum_{a} \sigma_{k,k+a}$$

(109)

$$\tilde{J}^{e}_{k,k+a} = -\widetilde{M}^{e}_{k,k+a}\, \Delta\tilde{\mu}^{e}_{k}$$

$$\widetilde{M}^{e}_{k,k+a} = \frac{w^{e}}{kT}\, f(p^{0}_{k}) f(p^{0}_{k+a})$$

(110)

$$\tilde{\mu}^{e}_{k} = E_F + q^{e} V_k + \frac{p^{e}_{k}}{D(E_F)}$$

where E_F is the Fermi level, q^e is the electron charge, V_k is the electrostatic potential at site k, $D(E_F)$ is the density of states at the Fermi level and $f(p_k^0)$ plays a similar role as p_k^0 in determining the occupation probability, but with a more pronounced transition to prevent electrons from escaping the metal. Consequently, the electrochemical reaction term $\sigma_{k,k+a}$ is derived from an Arrhenius law for an elementary step, like the diffusion process discussed earlier.

$$\sigma_{k,k+a} = w^*[1 - f(p_k^0)]f(p_{k+a}^0)\left[\exp\left(\frac{\tilde{\mu}_k^+ + \tilde{\mu}_{k+a}^e}{kT}\right) - \exp\left(\frac{\tilde{\mu}_k^0}{kT}\right)\right] \tag{111}$$

where w^* is a pre-exponential factor that accounts for the attempt frequency of the reaction. Finally, the electrostatic potential is resolved via a discrete Poisson equation:

$$\sum_{\alpha} V_{k+1} - 4V_k = \frac{2^{2-d}}{\epsilon} \sum_{\alpha=+,-,e} q^\alpha \, p_k^\alpha \tag{112}$$

References

[1] M. Crapo, S. Whitehouse, C. Booker, J. E. Risch, O. G. Hatch, L. Murkowski, R. Durbin, L. Strange, Nuclear energy innovation capabilities act of 2017, Public Law No. 115–248, 2018. 115th Congress, 132 Stat. 3154–3161.

[2] G. I. I. Forum, Molten salt reactors (msr), Generation IV Criteria and Technologies, 2024.

[3] J. Krepel, K. J. Kramer, in: T. J. Dolan, I. P´azsit, A. Rykhlevskii, R. Yoshioka (Eds.), Molten Salt Reactors and Thorium Energy, Elsevier, 953–972, 2024.

[4] E. Blandford, Kyle Brumback, Lambert Fick, Craig Gerardi, Brandon Haugh, Elizabeth Hillstrom, Kevin Johnson, Per F. Peterson, Floren Rubio, Fatih S. Sarikurt, Sonat Sen, Haihua Zhao, Nicolas Zweibaum, Nuclear Engineering and Design, V 364, 110636, ISSN 0029-5493, 2020.

[5] N. Resources, Advanced nuclear development, https://www.naturaresources.com/, 2025.

[6] D. E. Holcomb, L. Cheng, B. Cipiti, V. V. Ignatiev, G. Edwards, M. Allibert, E. Merle, S. Delpech, L. Giot, D. Heuer, 2023 PRPP GIF MSR Proliferation Resistance and Physical Protection White Paper, Technical Report, Generation IV International Forum (GIF), 2023.

[7] P. N. Haubenreich, J. R. Engel, Nuclear Applications and Technology 8, 118–136, 197, 2017.

[8] S. S. Raiman, D. Sulejmanovic, J. M. Kurley, J. Lee, C. G. Parker, B. A. Pint, Technical Assessment of Materials Compatibility in Molten Salt Reactors, Technical Report ML21084A039, U.S. Nuclear Regulatory Commission, 2021.

[9] B. A. Pint, D. Sulejmanovic, R. Pillai, Evaluating Static Isothermal Molten Salt Compatibility with Structural Alloys, Technical Report ML23129A786, U.S. Nuclear Regulatory Commission, 2023.

[10] R. Pillai, A. Savara, Preliminary Assessment of Models for Generating Predictions of Long-Term Corrosion in Molten Salts, Technical Report ML24095A304, U.S. Nuclear Regulatory Commission, 2024.

[11] E. Kiosidou, D. Sulejmanovic, B. A. Pint, Effect of Fission Products on Degradation of Structural Materials in Molten Salt Reactors, Technical Report ML24178A348, Oak Ridge National Laboratory, 2024.

[12] G. Cao, G. Fredrickson, K. Marsden, Electrochemical Monitoring for Molten Salt Reactors: Status Review, Technical Report ML25080A225, U.S. Nuclear Regulatory Commission, 2025.

[13] G. Zheng, Ph.D. Thesis, University of Madison Wisconsin 2015.

[14] G. Zheng, B. Kelleher, G. Cao, M. Anderson, T. Allen, K. Sridharan, Journal of Nuclear Materials 461, 143–150, 2015.

[15] X. Liu, A. Ronne, L. C. Yu, Y. Liu, M. Ge, C. H. Lin, B. Layne, P. Halstenberg, D. S. Maltsev, A. S. Ivanov, S. Antonelli, S. Dai, W. K. Lee, S. M. Mahurin, A. I. Frenkel, J. F. Wishart, X. Xiao, Y. chen Karen Chen-Wiegart, Nature Communications,1–12., 2021.

[16] R. D. Kane, Corrosion: Fundamentals, Testing, and Protection, 216–219, 2003.

[17] W. B. Cottrell, H. E. Hungerford, J. K. Leslie, J. L. Meem, Operation of the Aircraft Reactor Experiment, Technical Report, Oak Ridge National Laboratory, Oak Ridge, TN, United States, 1955.

[18] R. Roper, M. Harkema, P. Sabharwall, C. Riddle, B. Chisholm, B. Day, P. Marotta, Annals of Nuclear Energy 169, 108924, 2022.

[19] N. S. Patel, V. Pavlık, M. Boca, Critical Reviews in Solid State and Materials Sciences 42, 83–97, 2016.

[20] J. R. Keiser, X. He, D. Sulejmanovic, J. Qu, K. R. Robb, K. Oldinski, Journal of Solar Energy Engineering, Transactions of the ASME 145, 2023.

[21] K. Sridharan, T. R. Allen, in: Molten Salts Chemistry, 241–267, 2013.

[22] S. S. Raiman, S. Lee, Journal of Nuclear Materials 511, 523–535, 2018.

[23] B. C. Kelleher, Ph.D. Thesis, University of Wisconsin-Madison, 2015.

[24] S. Zhao, Q. Li, L. Wang, Y. Zhang, Materials Letters 60, 425–430, 2006.

[25] G. Mohan, M. Venkataraman, J. Gomez-Vidal, J. Coventry, Energy Conversion and Management, 2018.

[26] H. Sun, P. Zhang, J. Wang, Corrosion Science, 143, 187–199, 2018.

[27] E. S. Sooby, A. T. Nelson, J. T. White, P. M. McIntyre, Journal of Nuclear Materials, 466, 280–285, 2015.

[28] O. Benes, R. J. M. Konings, Journal of Nuclear Materials, 375 (2008) ,202–208, 2008.

[29] C. W. Bjorklund, J. G. Reavis, J. A. Leary, K. A. Walsh, Journal of Physical Chemistry, 63, 1774–1777, 1959.

[30] S. Delpech, C. Carriere, A. Chmakoff, L. Martinelli, D. Rodrigues, C. Cannes, Materials 17, 581, 2024.

[31] A. L. Frischknecht, D. O. Halligan, M. L. Parks, Journal of Chemical Physics, 14,54708, 2014.

[32] T. Hartmann, P. Paviet, Journal of Nuclear Fuel Cycle and Waste Technology (JNFCWT) 20, 43–63, 2022.

[33] D. A. Andersson, B. W. Beeler, Journal of Nuclear Materials, 568, 153836, 2022.

[34] B. Li, Z. R. Jones, C. Eiroa-Lledo, K. E. Knope, V. Mocko, B. W. Stein, J. N. Wacker, S. A. Kozimor, E. R. Batista, P. Yang, Inorganic Chemistry 62, 10528–10538, 2023.

[35] C. R. Lhermitte, H. K. Patenaude, J. M. Jackson, M. J. Monreal, Electrochimica Acta, 487, 144123, 2024.

[36] M. M. MacInnes, Z. R. Jones, B. Li, N. H. Anderson, E. R. Batista, I. M. DiMucci, C. Eiroa-Lledo, K. E. Knope, M. Y. Livshits, S. A. Kozimor, V. Mocko, K. A. Pace, F. R. Rocha, B. W. Stein, J. N. Wacker, P. Yang, Dalton Transactions, 50, 15696–15710, 2021.

[37] I. K. Delimarskii, B. F. Markov, in: Electrochemistry of Fused Salts, The Sigma Press, Washington, D.C., 159–200, 1961.

[38] C. Edeleanu, R. Littlewood, Electrochimica Acta, 3, 195–207, 1960.

[39] C. F. Baes, Journal of Nuclear Materials, 51, 149–162, 1974.

[40] J. A. Plambeck, Journal of Chemical Engineering Data, 12,77–82, 1967.

[41] S. Guo, J. Zhang, W. Wu, W. Zhou, Progress in Materials Science, 97, 448–487, 2018.

[42] V. Ignatiev, A. Surenkov, in: Comprehensive Nuclear Materials, V1-5, Elsevier, 221–250, 2012.

[43] J. A. Yingling, J. Schorne-Pinto, M. Aziziha, J. C. Ard, A. M. Mofrad, M. S. Christian, C. M. Dixon, T. M. Besmann, Journal of Chemical Thermodynamics, 179,106974, 2023.

[44] J. A. Yingling, M. Aziziha, J. Schorne-Pinto, J. P. S. Palma, J. C. Ard, R. E. Booth, C. M. Dixon, T. M. Besmann, ACS Applied Energy Materials, 6, 5868–5882, 2023.

[45] S. S. Parker, A. Long, C. Lhermitte, S. Vogel, M. Monreal, J. M. Jackson, Journal of Molecular Liquids , 346, 118147, 2022.

[46] C. J. Rao, S. Ningshen, C. Mallika, U. K. Mudali, Journal of Nuclear Materials, 501, 189–199, 2018.

[47] M. A. Rose, L. D. Gardner, T. T. Lichtenstein, S. A. Thomas, E. Wu, Property Measurements of NaCl UCl_3 and NaCl-KCl-UCl_3 Molten Salts (Rev.1), Technical Report, Argonne National Laboratory, Argonne, IL, United States, 2023.

[48] J. C. Shiloff, Journal of Physical Chemistry 64, 1566–1567, 1960.

[49] K. A. Romberger, J. Braunstein, R. E. Thoma, Journal of Physical Chemistry, 76, 1154–1159, 1972.

[50] J. Schorne-Pinto, M. Aziziha, H. B. Tisdale, A. M. Mofrad, A. Birri, M. S. Christian, J. C. Ard, R. E. Booth, J. A. Yingling, J. P. S. Palma, C. Dixon, H. C. zur Loye, T. M. Besmann, ACS Applied Energy Materials, 7, 4016–4029, 2024.

[51] T. Y. Karlsson, M. E. Woods, N. H. Erfurth, M. W. Lounsbury, R. V. Roper, D. D. Tolman, S. A. Warmann, Analysis and Thermal Property Investigations into Ternary Actinide Chloride Salt Systems Containing UCl3 and PuCl3, Technical Report, Idaho National Laboratory, INL/RPT-23-74483 Idaho Falls, 2023.

[52] M. Pourbaix, Corrosion, 25, 267–284, 1969.

[53] R. Littlewood, E. J. Argent, Electrochimica Acta, 4, 114–128, 1961.

[54] A. D. Graves, D. Inman, Journal of Electroanalytical Chemistry and Interfacial Electrochemistry, 25, 357–372, 1970.

[55] A. D. Graves, Journal of Electroanalytical Chemistry and Interfacial Electrochemistry, 25, 349–356, 1970.

[56] R. Parsons, Chemical Reviews, 90, 813–826, 1980.

[57] A. D. Graves, D. Inman, Nature, 208, 481–482, 1965.

[58] A. Kisza, Electrochimica Acta, 51, 2315–2321, 2006.

[59] J. Klos, S. Lamperski, Journal of Chemical Physics 150, 2019.

[60] N. Termini, A. Birri, S. Henderson, N. D. B. Ezell, An Overview of the Molten Salt Thermal Properties Database – Thermophysical, Version 2.1.1 (MSTDB-TP v.2.1.1), Technical Report, Oak Ridge National Laboratory, 2023. Accessed 2024-11-17.

[61] J. C. Ard, J. A. Yingling, T. J. Johnson, J. Schorne-Pinto, M. Aziziha, C. M. Dixon, M. S. Christian, J. W. McMurray, T. M. Besmann, Journal of Nuclear Materials, 563, 153631, 2022.

[62] B. Spencer, T. Besmann, Integration Plan for NEAMS Structural Materials and Chemistry MSR Modeling, Technical Report, Idaho National Laboratory, Idaho Falls, ID, United States, 2022.

[63] P. J. Spencer, Calphad, 32, 1–8, 2008.

[64] T. M. Besmann, J. Schorne-Pinto, Thermo Vol. 1, 168-178, 2021.

[65] J. H. DeVa, R. B. Evans, Corrosion Behavior of Reactor Materials in Fluoride Salt Mixtures, Technical Report ORNL-TM-328, Oak Ridge National Laboratory, Oak Ridge, TN, United States, 1962.

[66] I. R. B. Evans, J. H. DeVan, G. M. Watson, Self-Diffusion of Chromium in Nickel-Base Alloys, Technical Report, Oak Ridge National Laboratory, Oak Ridge, TN, United States, 1961.

[67] R. S. Nicholson, Analytical Chemistry, 37,1351–1355, 1965.

[68] A. J. Bard, L. R. Faulkner, Electrochemical Methods: Fundamentals and Applications, John Wiley & Sons, Inc., New York, 2001.

[69] S. A. Kuznetsov, M. Gaune-Escard, Journal of Nuclear Materials, 389, 108–114, 2009.

[70] S. A. Kuznetsov, M. Gaune-Escard, Journal of Electroanalytical Chemistry, 595,11–22, 2006.

[71] S. A. Kuznetsov, M. Gaune-Escard, Electrochimica Acta 46, 1101–1111, 2001.

[72] H. K. Patenaude, Ph.D. thesis, University of Nevada, Las Vegas, Las Vegas, 2024.

[73] M. G. Trachioti, A. C. Lazanas, M. I. Prodromidis, Microchimica Acta, 190, 1–14, 2023.

[74] C. J. Rao, K. A. Venkatesan, K. Nagarajan, T. G. Srinivasan, P. R. V. Rao, Electrochimica Acta, 54, 4718–4725, 2009.

[75] R. Nagaishi, M. Arisaka, T. Kimura, Y. Kitatsuji, Journal of Alloys and Compounds, 431, 221–225, 2007.

[76] R. J. Klingler, J. K. Kochi, The Journal of Physical Chemistry, 85, 1731–1741, 1981.

[77] A. J. Bard, L. R. Faulkner, J. Wiley, Electrochemical methods: fundamentals and applications, 20220

[78] P. Delahay, in: P. Delahay, C. N. Reilley (Eds.), New Instrumental Methods in Electrochemistry: Theory, Instrumentation, and Applications to Analytical and Physical Chemistry, Interscience Publishers, Inc., New York, 115–145, 1954.

[79] N. Hege, J. Jackson, J. Shafer, Journal of The Electrochemical Society, 170, 016503, 2023.

[80] I. B. Polovov, A. V. Abramov, K. V. Dedov, V. V. Karpov, A. Y. Zhilyakov, A. F. Gibadullina,S. V. Belikov, V. A. Volkovich, O. I. Rebrin, ECS Transactions, 77, 847–855, 2017

[81] C. Jiang, D. Andersson, G. Wang, B. Li, P. Yang, Lower-Length-Scale Modeling of Chemical Additions, Corrosion and Fission Products in Select MSR Base Salts, Technical Report, Idaho National Laboratory, Idaho Falls, ID (United States), 2023.

[82] T. Karlsson, S. Warmann, D. Tolman, T. Rigoulot, C. Wren, C. Howard, T. Trowbridge, J. Burns, N. Erfurth, C. Falconer, I. Mitchell, Experimental Investigations into the Corrosion of Alloy 625 Us- ing NaCl-$PuCl_3$ Molten Salt in a Natural Circulation Microloop, Technical Report, Idaho National Laboratory, Idaho Falls, ID (United States), 2024.

[83] A. S. Dedova, A. O. Shibitko, O. L. Sukhorukova, A. V. Abramov, N. L. Vasilyeva, A. V. Saprygin,O. I. Rebrin, in: American Institute of Physics Conference Proceedings, volume 2015, American Institute of Physics Inc., 2018.

[84] J. W. Park, S. Yoon, H. J. Eom, S. Kim, C. Jang, J.-I. Yun, Corrosion Science, 252, 112979, 2025.

[85] M. L. Newton, D. E. Hamilton, M. F. Simpson, ECS Transactions, 98, 19–25, 2020.

[86] K. Hanson, K. M. Sankar, P. F. Weck, J. K. Startt, R. Dingreville, C. S. Deo, J. D. Sugar, P. M. Singh, Corrosion Science, 194, 109914, 2022.

[87] J. Zhang, C. W. Forsberg, M. F. Simpson, S. Guo, S. T. Lam, R. O. Scarlat, F. Carotti, K. J. Chan, P. M. Singh, W. Doniger, K. Sridharan, J. R. Keiser, Corrosion Science, 144, 44–53, 2018.

[88] W. Ding, H. Shi, A. Jianu, Y. Xiu, A. Bonk, A. Weisenburger, T. Bauer, Solar Energy Materials and Solar Cells, 193, 298–313, 2019.

[89] A. Ibrahim, H. Peng, A. Riaz, M. Abdul Basit, U. Rashid, A. Basit, Solar Energy Materials and Solar Cells, 219, 110768, 2021.

[90] J. W. Koger, Evaluation of Hastelloy N Alloys after Nine Years Exposure to Both a Molten Fluoride Salt and Air at Temperatures from 700 to 560oC, Technical Report, Oak Ridge National Laboratory, Oak Ridge, TN (United States), 1972.

[91] J. W. Koger, Alloy Compatibility with LiF–BeF_2 Salts Containing ThF_4 and UF_4, Technical Report, Oak Ridge National Laboratory, Oak Ridge, TN (United States), 1972.

[92] J. R. Keiser, D. L. Manning, R. E. Clausing, in: ECS Proceedings Volumes, volume 1976-6, The Electrochemical Society, 1976, pp. 315–328.

[93] J. R. Keiser, Compatibility Studies of Potential Molten-Salt Breeder Reactor Materials in Molten Fluoride alts. [Inconel 601, Cr and Nb Modifications of Hastelloy N], Technical Report, Oak Ridge National Laboratory, Oak Ridge, TN (United States), 1977.

[94] S. Guo, N. Shay, Y. Wang, W. Zhou, J. Zhang, Journal of Nuclear Materials 496, 197–206, 2017.

[95] S. Simunovic, B. G. Gaston, T. M. Besmann, Thermochimica, https://github.com/ORNL-CEES/thermochimica, , 2017.

[96] A. Pelton, Phase diagrams and thermodynamic modeling of solutions, 2018.

[97] N. Saunders, A. Miodownik, CALPHAD (calculation of phase diagrams): a comprehensive guide, 1998.

[98] G. N. Haidemenopoulos, Physical Metallurgy, https://doi.org/10.1201/9781315211220, 2018.

[99] A. D. Pelton, S. A. Degterov, G. Eriksson, C. Robelin, Y. Dessureault, Metallurgical and Materials Transactions B: Process Metallurgy and Materials Processing Science, 31, 651–659, 2000.

[100] A. D. Pelton, P. Chartrand, Metallurgical and Materials Transactions A: Physical Metallurgy and Materials Science, 32, 1355–1360, 2001.

[101] P. Chartrand, A. D. Pelton, Metallurgical and Materials Transactions A: Physical Metallurgy and Materials Science, 32,1397–1407, 2001.

[102] A. D. Pelton, P. Chartrand, G. Eriksson, Metallurgical and Materials Transactions A: Physical Metallurgy and Materials Science, 32,1409–1416, 2001.

[103] R. H. Fowler, Statistical thermodynamics, CUP Archive, 1939.

[104] C. W. Bale, E. B´elisle, P. Chartrand, S. A. Decterov, G. Eriksson, A. E. Gheribi, K. Hack, I. H. Jung, Y. B. Kang, J. Melan¸con, A. D. Pelton, S. Petersen, C. Robelin, J. Sangster, P. Spencer,

[105] M. A. V. Ende, Calphad, 54, 35–53, 2016.

[106] S. Bigdeli, L. F. Zhu, A. Glensk, B. Grabowski, B. Lindahl, T. Hickel, M. Selleby, Calphad, 65, 79–85, 2019.

[107] P. S¨oderlind, A. Perron, E. E. Moore, A. Landa, T. W. Heo, Applied Sciences, 10, 3914, 2020.

[108] J. A. Oc´adiz-Flores, A. E. Gheribi, J. Vlieland, K. Dardenne, J. Rothe, R. J. Konings, A. L. Smith, Journal of Molecular Liquids, 331, 115820, 2021.

[109] X. Li, J. Song, S. Shi, L. Yan, Z. Zhang, T. Jiang, S. Peng, Journal of Physical Chemistry A, 121, 571–578, 2017.

[110] A. Dinsdale, Calphad, 15, 317–425, 1991.

[111] H. L. Chan, E. Romanovskaia, J. Qiu, P. Hosemann, J. R. Scully, npj Materials Degradation, 6, 1–10, 2022.

[112] B. A. Frandsen, S. D. Nickerson, A. D. Clark, A. Solano, R. Baral, J. Williams, J. Neuefeind, M. Memmott, Journal of Nuclear Materials, 537, 152219, 2020.

[113] R. L. Fitzhugh, A. D. Clark, S. D. Nickerson, M. J. Memmott, J. N. Harb, Journal of The Electrochemical Society, 168, 026502, 2021.

[114] M. H. Piro, M. J. Welland, M. Stan, Journal of Nuclear Materials, 464, 48–52, 2015.

[115] M. H. Piro, M. Poschmann, P. Bajpai, Journal of Nuclear Materials, 526, 151756, 2019.

[116] Y. chen Karen Chen-Wiegart, S. Wang, W.-K. Lee, I. McNulty, P. W. Voorhees, D. C. Dunand, Acta Materialia, 61, 1118–1125, 2013.

[117] Y. Hu, Y. Han, Y. Qin, H. Zhou, IOP Conference Series: Materials Science and Engineering, 394 , 032117, 2018.

[118] A. U. Seybolt, Oxidation of Metals, 2, 137–153, 1970.

[119] J. Kerr, N. Bieberdorf, L. Capolungo, M. Asta, Phys. Rev. Mater., 8, 103802, 2024.

[120] N. Bieberdorf, M. Asta, L. Capolungo, npj Computational Materials, 9, 127, 2023.

[121] I. McCue, B. Gaskey, P.-A. Geslin, A. Karma, J. Erlebacher, Acta Materialia, 115, 10–23, 2016.

[122] N. Epstein, Chemical Engineering Science, 44, 777–779, 1989.

[123] Y. chen Karen Chen-Wiegart, R. DeMike, C. Erdonmez, K. Thornton, S. A. Barnett, J. Wang, Journal of Power Sources, 249, 349–356, 2014.

[124] Q. Chen, K. Sieradzki, Journal of The Electrochemical Society, 160, 226–231, 2013.

[125] T. Tzvetkoff, J. Kolchakov, Materials Chemistry and Physics, 87, 201–211, 2004.

[126] A. S. Khanna, in: M. Kutz (Ed.), Handbook of Environmental Degradation of Materials, William Andrew, 2 edition127–148, 2012.

[127] J. Erlebacher, Journal of The Electrochemical Society, 151, 614–626, 2004.

[128] K. Wagner, H. H¨acker, H. J. Engell, Journal of The Electrochemical Society, 144, 3545–3552, 1997.

[129] M. Itoh, Scientific Reports, 12, 6944, 2022.

[130] E. Sooby, M. Alamaniotis, A. Heifetz, in: Proceedings of the 12th Nuclear Plant Instrumentation, Control and Human-Machine Interface Technologies, American Nuclear Society, 239-250, 2021.

[131] M. Z. Bazant, Accounts of Chemical Research, 46, 1144–1160, 2013.

[132] R. Seeber, C. Zanardi, G. Inzelt, ChemTexts, 1, 1–16, 2015.

[133] L. Liang, Y. Qi, F. Xue, S. Bhattacharya, S. J. Harris, L.-Q. Chen, Physical Revie E, 86, 51609, 2012.

[134] L. Chen, H. W. Zhang, L. Y. Liang, Z. Liu, Y. Qi, P. Lu, J. Chen, L. Q. Chen, Journal of Power Sources, 300, 376–385, 2015.

[135] D. C. Grahame, Chemical Reviews, 41, 441–501, 1947.

[136] J. Wu, Chemical Reviews, 122, 10821–10859, 2022.

[137] D. Henderson, D. Boda, Physical Chemistry Chemical Physics, 11, 3822–3830, 2009.

[138] D. N. Petsev, F. van Swol, L. J. D. Frink, Molecular Theory of Electric Double Layers, 2021.

[139] A. A. Kornyshev, Journal of Physical Chemistry B, 111, 5545–5557, 2007.

[140] M. S. Kilic, M. Z. Bazant, A. Ajdari, Physical Review E - Statistical, Nonlinear, and Soft Matter Physics, 75, 2007.

[141] M. Z. Bazant, B. D. Storey, A. A. Kornyshev, Physical Review Letters, 106, 046102, 2011.

[142] L. Langford, N. Winner, A. Hwang, H. Williams, L. Vergari, R. O. Scarlat, M. Asta, Journal of Chemical Physics, 157, 94705, 2022.

[143] H. Wang, L. Pilon, Electrochimica Acta, 64,130–139, 2012.

[144] R. Pillai, S. S. Raiman, B. A. Pint, Journal of Nuclear Materials, 546 ,152755, 2021.

[145] S. A. Policastro, J. C. Carnahan, G. Zangari, H. Bart-Smith, E. Seker, M. R. Begley, M. L. Reed, P. F. Reynolds, R. G. Kelly, Journal of The Electrochemical Society 157,328–337, 2010.

[146] O. Zinchenko, H. A. D. Raedt, E. Detsi, P. R. Onck, J. T. M. D. Hosson, Computer Physics Communications 184, 1562–1569, 2013.

[147] J. K. Startt, C. S. Deo, S. S. Raiman, Modeling Salt-Material Interactions in Molten Salt Reactors: Opportunities and Path Forward, Technical Report ORNL/TM-2019/1194, Oak Ridge National Laboratory, 2019.

[148] M. Plapp, J.-F. Gouyet, The European Physical Journal B, 9, 267–282, 1999.

[149] M.-O. Bernard, M. Plapp, J.-F. Gouyet, *Physical Review E,* 68, 011604, 2003.

[150] W. J. Boettinger, J. A. Warren, C. Beckermann, A. Karma, *Annual Review of Materials Science,* 32, 163–194, 2002.

[151] L.Q. Chen, *Annual Review of Materials Research* 32, 113–153, 2002

[152] L. Q. Chen, W. Yang, *Physical Review B* 50, 15752–15756, 1994.

[153] Y. Wang, Y. Jin, A.M. Cuitino, A.G. Khachaturyan, *Appl. Phys. Lett.* 78, 2324–2326, 2001.

[154] D. Rodney, Y. L. Bouar, A. Finel, *Acta Materialia* 51, 17–30, 2003.

[155] H. Henry, H. Levine, *Physical Review Letters,* 93, 2004.

[156] A. Kazaryan, Y. Wang, B. R. Patton, *Scripta Materialia,* 41, 487–492, 1999.

[157] N. Moelans, B. Blanpain, P. Wollants, *Calphad,* 32, 268–294, 2008.

[158] S. G. Kim, W. T. Kim, T. Suzuki, *Physical Review E* 60, 7186–7197, 1999.

[159] M. Plapp, *Physical Review E,* 84, 031601, 2011.

[160] A. A. Wheeler, W. J. Boettinger, G. B. McFadden, *Physical Review A,* 45, 7424–7439, 1992.

[161] I. Steinbach, *Modelling Simul. Mater. Sci. Eng,* 17, 31, 2009.

[162] G. Caginalp, *Archive for Rational Mechanics and Analysis* 92, 205–245, 1986.

[163] J. W. Cahn, J. E. Hilliard, *The Journal of Chemical Physics* 28, 258–267, 1958.

[164] N. Moelans, *Acta Materialia,* 59,1077–1086, 2011.

[165] S. M. Allen, J. W. Cahn, *Acta Metallurgica,* 20, 423–433, 1972.

[166] L. Liang, L. Q. Chen, *Applied Physics Letters,* 105, 263903, 2014.

[167] J. E. Guyer, W. J. Boettinger, J. A. Warren, G. B. McFadden, *Physical Review E,* 69, 021603, 2004.

[168] J. E. Guyer, W. J. Boettinger, J. A. Warren, G. B. McFadden, *Physical Review E* 69, 021604, 2004.

[169] D. A. Cogswell, *Physical Review E,* 92, 011301, 2015.

[170] C. V. Bhave, G. Zheng, K. Sridharan, D. Schwen, M. R. Tonks, *Journal of Nuclear Materials* 574, 154147, 2023.

[171] X. Wu, I. Abdallah, W. Jiang, R. S. Ullberg, S. R. Phillpot, A. Couet, J. H. Perepezko, M. R. Tonks, *Computational Materials Science,* 218, 111996, 2023.

[172] J. Zhang, A. F. Chadwick, P. W. Voorhees, *Journal of The Electrochemical Society,* 170, 120503, 2023.

[173] T. Q. Ansari, Z. Xiao, S. Hu, Y. Li, J. L. Luo, S. Q. Shi, *npj Computational Materials,* 4, 1–9, 2018.

[174] T. Ansari, J.-L. Luo, S.-Q. Shi, *Journal of The Electrochemical Society,* 167, 061508, 2020.

[175] D. Qu, R. Termuhlen, H.-C. Yu, *Journal of The Electrochemical Society* 167, 140515, 2020.

[176] D. Qu, A. Malik, H. C. Yu, *Electrochimica Acta* 432, 141141, 2022.

[177] A. Malik, H.-C. Yu, *Journal of The Electrochemical Society,* 169, 070527, 2022.

[178] C. E. D. Chidsey, *Science,* 251,919–922, 1991.

[179] Y. Zeng, R. B. Smith, P. Bai, M. Z. Bazant, *Journal of Electroanalytical Chemistry,* 735, 77–83, 2014.

[180] K. R. Elder, M. Grant, N. Provatas, J. M. Kosterlitz, *Physical Review E*, 64, 021604, 2001.

[181] Z. Hong, V. Viswanathan, *ACS Energy Letters* 3 (2018) 1737–1743, 2018.

[182] J. Jeon, G. H. Yoon, T. Vegge, J. H. Chang, *ACS Applied Materials & Interfaces,* 14, 15275–15286, 2022.

[183] H. Wen, M. Zhang, S. Wang, Z. Zhao, Y. Wang, Y. Yan, D. Zhang, X. Sun, *ACS Applied Materials & Interfaces,* 17, 7881–7893, 2025.

[184] D. R. Ely, A. Jana, R. E. García, *Journal of Power Sources,* 272, 581–594, 2014.

[185] C. Bhave, M. R. Tonks, *Journal of Nuclear Materials,* 606,155616, 2025.

[186] T. Ghaznavi, S. Persaud, R. Newman, *Journal of The Electrochemical Society,* 169, 111506, 2022.

[187] G. Zheng, K. Sridharan, *Journa of Materials,* 70, 1535–1541, 2018.

[188] C. Bonneville, N. Bieberdorf, A. Hegde, M. Asta, H. N. Najm, L. Capolungo, C. Safta, *npj Computational Materials,* 11, 14, 2025.

[189] D. Montes de Oca Zapiain, J. A. Stewart, R. Dingreville, *npj Computational Materials,* 7, 3, 2021.

[190] S. A. Walker, M. E. Tano, A. Abou-Jaoude, O. Calvin, Frontiers in Nuclear Engineering, 2, 2023.

[191] A. Leong, J. Zhang, S. D. Rountree, High Temperature Corrosion of Materials, 99, 375–397, 2023.

[192] S. Guo, W. Zhuo, Y. Wang, J. Zhang, Corrosion Science, 163, 108279, 2020.

[193] L. Langford, N. Winner, A. Hwang, H. Williams, L. Vergari, R. O. Scarlat, M. Asta, The Journal of Chemical Physics, 157, 9, 2022.

[194] T. M. Besmann, J. Ard, J. Schorne-Pinto, J. A. Yingling, M. Aziziha, C. M. Dixon, et al., Journal of Nuclear Materials, 563, 153631, 2022.

[195] T. M. Besmann, J. Schorne-Pinto, J. Paz Soldan Palma, C. Dixon, R. Booth, J. Wilson, A. Padinhare Manissery, Z. Gardiner, Generation of Molten Salt Thermochemical Properties and Database Development, presen accessible at GAIN-INL, 2025.

[196] B. R. Betzler, et al., Molten Salt Reactor Thermodynamic Database (MSTDB) Development, Oak Ridge National Laboratory, 2021.

[197] T. M. Besmann, Update on MSTDB-TC Database, GAIN-INL Molten Salt Reactor Campaign, 2024.

[198] D. Boda, D. Henderson, K. Y. Chan, J. Chem. Phys, 110, 5346, 1999.

[199] H. Arkoub, S. Dwivedi, A. C. van Duin, M. Jin, Applied Surface Science, 655, 159627, 2024.

[200] L. Frischknecht, K. J. Halligan, M. L. Parks, Journal of Chemical Physics, 141, 054708, 2014.

[201] J. S. Klos, S. Lamperski, Journal of Chemical Physics, 150, 064704, 2019.

[202] J. Vatamanu, O. Borodin, G. D. Smith, Physical Chemistry Chemical Physics, 12, 1707, 2010.

[203] M.Ling, W. Sun,, Y. Xue, L. Yan, B. y=Yue, Journal of Molecular liquids 413, 125915, 2024.

[204] L. Lankford, N. Winner, A. Hwang, H. Williams, L. Vergari, R. O. Scarlat, M. Asta, Journal of Chemical Physics, 157, 094705, 2022.

[205] C.-F. Chen, Y.-C. Cheng, C.-W. Hong, CCMES 109-110, 263–283, 2015.

[206] A. L. Smith, E. Capelli, R. J. M. Konings, A. E. Gheribi, Journal of Molecular Liquids, 299,112165, 2020.

[207] S. Attarian, C. Shen, D. Morgan, I. Szlufarska, Machine learning interatomic potentials for molten salts: best practices, Computational Materials Science, 246,113409, 2025.

[208] M. Lambrecht, M. T. de Miguel, M. I. Lasanta, G. García-Martín, F. J. Pérez, International Journal of Heat and Mass Transfer, 196,123273, 2022.

[209] D. Andersson, B. W. Beeler, Journal of Nuclear Materials 568153836, 2022.

[210] M. S. Emerson, S. Sharma, S. Roy, V. S. Bryantsev, A. S. Ivanov, R. Gakhar, M. E. Woods, L. C. Gallington, S. Dai, D. S. Maltsev, C. J. Margulis, Journal of the American Chemical Society 144 (47), 21751–21762, 2022.

[211] C. Zhu, J. Song, Y. Wang, H. Luo, Y. Ding, W. Zhou, Y. Wang, Journal of Nuclear Materials, 609, 155749, 2025.

[212] B. C. Kelleher, S. F. Gagnon, I. G. Mitchell, Materials Today Communications, 33,104358, 2022.

[213] R. Guidelli, R. G. Compton, J. M. Feliu, E. Gileadi, J. Lipkowski, W. Schmickler, S. Trasatti, Pure and Applied Chemistry 86 (2), 245–258, 2014.

[214] B.A.T. Mehrabadi, J.W. Weidner, B. Garcia-Diaz, M. Martinez-Rodriguez, L. Olson, S. Shimpalee, Journal of The Electrochemical Society, 163, 830–838, 2016.

[215] H.-S. Cho, J. W. Van Zee, S. Shimpalee, B. A. Tavakoli, J. W. Weidner, B. L. Garcia-Diaz, M. J. Martinez-Rodriguez, L. Olson, J. Gray, Corrosion, 72 (6), 742–760, 2016.

[216] S. Pillai, S.S. Raiman, B.A. Pint, Journal of Nuclear Materials, 542, 152465, 2020.

[217] H. Larsson, A. Engström, A homogenization approach to diffusion simulations applied to α + γ Fe–Cr–Ni diffusion couples, Acta Materialia, 54, 2431–2439, 2006.

[218] N. Bieberdorf, L. Capolungo, M. Asta, Morphologies of dealloying corrosion attack at grain boundaries, Acta Materialia, 236, 121308, 2025.

[219] N. Bieberdorf, M. Asta, L. Capolungo, Grain boundary effects in high-temperature liquid-metal dealloying: a multi-phase field study, npj Computational Materials 9 (1), 12, 2023.

[220] V. Prithivirajan, Examining Graphite Degradation in Molten Salt Environments: A Chemical, Physical, and Material Analysis, 2024.

[221] A. Savara, E. Walker, ChemCatChem, 12, 5385 – 5400, 2020.

[222] B. Ruscic, R. E. Pinzon, M. L. Morton, G. von Laszevski, S. J. Bittner, S. G. Nijsure, K. A. Amin, M. Minkoff, and A. F. Wagner, *The Journal of Physical Chemistry A*, *108* (45), 9979-9997, 2004.

[223] B. Ruscic, International journal of quantum chemistry, International Journal of Quantum Chemistry, 114, 1097–110, 2014.

[224] B.Ruscic, B., Feller, D., Peterson. Active Thermochemical Tables: dissociation energies of several homonuclear first-row diatomics and related thermochemical values. In: Wilson, A., Peterson, K., Woon, D. (eds) Thom H. Dunning, Jr.. Highlights in Theoretical Chemistry, vol 10. Springer, Berlin, Heidelberg, 2015.

[225] B. Ruscic, R. E Pinzon, G. von Laszewski, D. Kodeboyina, A. Burcat, D. Leahy, D.Montoy and A. F Wagner *J. Phys.: Conf. Ser.* 16 561, 2005.

[226] P.N. Haubenreich & J.R. Engel, *Nuclear Applications and Technology*. 8 (2): 118–136, 1970.

[227] H.E. McCoy, B.McNabb, intergranular cracking of inor-8 in the MSRE, ORNL-4829, 1965.

[228] Jansen, A.P.J.. Kinetic Monte Carlo Algorithms. In: An Introduction to Kinetic Monte Carlo Simulations of Surface Reactions. Lecture Notes in Physics, vol 856. Springer, Berlin, Heidelberg. https://doi.org/10.1007/978-3-642-29488-4_3, 2012.

[229] A. Mie , P. Chiara , R. Karsten, Frontiers in Chemistry, 7, 2019.

[230] S. Matera, W. F. Schneider, A. Heyden, and A. Savara, *ACS Catalysis*, *9* (8), 2019.

[231] D. G. Vlachos, Advances in Chemical Engineering. V 30 1-61, 2005.

[232] T. Danielson, J. E. Sutton, C. Hin, A. Savara, Computer Physics Communications, 219, 149-163, 2017.

[233] A. Savara, J.E. Sutton, Journal of Physics: Condensed Matter,30 , 2018.

[234] Giannis D. Savva and Michail Stamatakis, *The Journal of Physical Chemistry A* 2025 *129* (6), 1726-1740, 2025.